# Probing the band structure and local electronic properties of low-dimensional semiconductor structures

by

Jenna Cherie Walrath

A dissertation submitted in partial fulfillment
of the requirements for the degree of
Doctor of Philosophy
(Physics)
in The University of Michigan
2016

**Doctoral Committee:**

Professor Rachel S. Goldman, Chair
Professor Roy Clarke
Associate Professor Kevin Patrick Pipe
Assistant Professor Liang Qi
Professor Ctirad Uher

© Jenna Cherie Walrath
2016

## Dedication

This dissertation is dedicated to my wonderful husband, Matt, and to my loving family, including my parents, Trudy and Craig, my siblings, Chris and Sheila, and the best in-laws anyone could ask for, Kim and Charlie. I love you all.

## Acknowledgements

First, I would like to thank my Ph.D. advisor, Professor Rachel Goldman, for her guidance and encouragement. I could not have asked for a more supportive mentor. I am also grateful to my committee members, Professors Roy Clarke, Ctirad Uher, Kevin Pipe, and Liang Qi, as well as Professor Cagliyan Kurdak, for their collaboration, support, and helpful discussions. Thank you to all of my STM lab mates, especially Yen-Hsiang Lin for his support and mentorship during the critical years at the beginning of my PhD research, Alex Chang, Chris Greenhill, and Eric Zech, as well as Mike Warren, Simon Huang, Davide Del Gaudio, and the rest of my Goldman group-mates. Thank you to all of my collaborators over the past few years, including Vladimir Stoica, Yuwei Li, Wei Liu, Lynn Endicott, and Si Hui, among others.

I'd also like to acknowledge the mentors I had as an undergraduate student: Professors Daniela Bortoletto, Jens Gundlach, Stephan Schlamminger, Rana Adhikari, and Dr. Alastair Heptonstall. The positive experiences I had in undergraduate research are 100% responsible for my decision to go to graduate school, and I am very grateful.

Thank you to the staff of the Physics Student Services, especially Christina Zigulis, for being so exceptional, and to the Physics Demonstration Lab, especially Warren and Monika, for providing the support and excellent demos that made so many SWIP events and my Saturday Morning Physics talk possible. I also need express my deep appreciation for everyone who created a wonderfully supportive environment in the Society of Women

in Physics: Kaitlin, Kate, Julia, Veronica, Jessie, Natasha, Anna, Prof. Christine Aidala and many many more on a list too long to name, thank you.

I would like to thank my husband, Matthew, and my family- my parents, siblings, and in-laws, for their endless support. Finally, I'd like to thank Julia and Stephanie for their friendship, which I value deeply, and their unwavering support.

## Table of Contents

Dedication ........ ii

Acknowledgements ........ iii

List of Tables ........ ix

List of Figures ........ x

List of Appendices ........ xviii

Abstract ........ xix

Chapter 1 Introduction ........ 1

1.1 Overview ........ 1

1.2 Low-dimensional structures for enhanced thermoelectric efficiency ........ 3

1.3 Self-assembled semiconductor quantum dots ........ 5

1.4 Topological insulators ........ 5

1.5 Methods for examining the structural and electronic properties of materials ........ 7

1.6 Dissertation Organization ........ 8

1.7 References ........ 12

Chapter 2 Experimental Procedures ........ 15

2.1 Overview ........ 15

2.2 Molecular Beam Epitaxy (MBE) ........ 15

2.3 Scanning Tunneling Microscopy (STM) ........ 16

2.3.1 Cross-sectional and plan-view STM ........ 17

2.3.2 Park Autoprobe VP2 and Omicron VT-STM ................................................ 18
2.4 Scanning Tunneling Spectroscopy (STS) ............................................................ 20
2.5 Scanning Thermoelectric Microscopy (SThEM) ................................................. 21
2.5.1 Overview ........................................................................................................ 22
2.5.2 SThEM Instrumentation ................................................................................ 23
2.5.3 Experimental procedure ................................................................................ 25
2.6 References ........................................................................................................... 34
Chapter 3 Quantifying the local Seebeck coefficient with SThEM ................................ 35
3.1 Overview .............................................................................................................. 35
3.2 Background .......................................................................................................... 36
3.3 MBE growth and sample preparation ................................................................... 37
3.4 XSTM of GaAs p-n junction ................................................................................. 38
3.5 SThEM of GaAs p-n junction ................................................................................ 39
3.6 Quasi-3D deconvolution ........................................................................................ 40
3.7 Measured $V_{SThEM}$ and converted S profiles ........................................................ 41
3.8 Summary and Conclusions ..................................................................................... 44
3.9 References ............................................................................................................. 49
Chapter 4 Profiling the local carrier concentration across a semiconductor quantum dot 51
4.1 Overview ................................................................................................................ 51
4.2 Background ............................................................................................................ 52
4.3 MBE growth of InAs quantum dots ........................................................................ 53
4.4 Plan-view STM of InAs QDs ................................................................................. 55
4.5 SThEM across a single InAs QD ............................................................................ 56

4.6 Conversion of $V_{SThEM}$ to free carrier concentration .............................................. 57
4.7 Poisson-Schrodinger band structure calculations of InAs QD .............................. 59
4.8 Atom probe tomography investigations of dopant distribution ............................. 60
4.9 Discussion ........................................................................................................ 62
4.10 Summary and Conclusions ............................................................................ 63
4.11 References ...................................................................................................... 70
Chapter 5 Ordered horizontal $Sb_2Te_3$ nanowires induced by femtosecond lasers ...........73
5.1 Overview .......................................................................................................... 73
5.2 Background ...................................................................................................... 74
5.3 MBE growth and nanowire formation ............................................................... 75
5.4 STM and SThEM studies .................................................................................. 76
5.5 Cross-sectional transmission electron microscopy of $Sb_2Te_3$ nanowires .............. 77
5.6 STS investigations ............................................................................................ 78
5.7 Summary and Conclusions ............................................................................... 78
5.8 References ........................................................................................................ 85
Chapter 6 Identification of topological surface states in $(Bi_{1-x}Sb_x)_2Te_3$ alloy films.........87
6.1 Overview .......................................................................................................... 87
6.2 Background ...................................................................................................... 88
6.3 Experimental Details ......................................................................................... 89
6.4 STM of BiSbTe films ........................................................................................ 90
6.5 STS of bulk and surface states .......................................................................... 91
6.6 Thickness-dependent electrical resistance of BiSbTe films .................................. 92
6.7 Summary and Conclusions ............................................................................... 93

6.8 References ... 99

Chapter 7 Summary and Suggestions for Future Work ... 100

7.1 Summary ... 100

7.1.1 Quantifying the local Seebeck coefficient with nanometer resolution ... 100

7.1.2 Profiling the local carrier concentration across a semiconductor quantum dot ... 101

7.1.3 Ordered Horizontal $Sb_2Te_3$ Nanowires Induced by Femtosecond Laser ... 102

7.1.4 Identification of topological surface states in $(Bi_{1-x}Sb_x)_2Te_3$ alloy films ... 102

7.2 Suggestions for Future Work ... 103

7.2.1 Investigating the composition of bulk thermoelectrics using SThEM ... 103

7.2.2 Strain-induced band gap opening in nanostructured graphene ... 105

7.2.3 Investigating the local electronic properties of quantum dots using SThEM 106

7.3 References ... 111

Appendices ... 112

## List of Tables


Table 6.1: $(Bi_{1-x}Sb_x)_2Te_3$ sample composition, thickness, carrier type, and effective band gap measured using STS. .......................................................................... 89

Table C.1: κ of the tip and samples used to calculate the f-factor and the bulk band gap values at 300 K used for comparison with the effective bandgaps measured by STS. ................................................................................................ 143

Table C.2: Material parameters of GaAs and used for the 1D Poisson-Schrodinger calculation.................................................................................................. 144

Table C.3: Material parameters of ternary $In_xGa_{1-x}As$ and used for the 1D Poisson-Schrodinger calculation. The ternary parameters follow the form $parameter\ value = constant + (linear)x + (quadratic)x^2$ ............... 144

## List of Figures

Figure 1.1: Energy dependence of the density of states for (a) an ideal free electron gas, (b) an electron free in 2 directions but constrained in 1 direction, (c) an electron free in 1 direction and constrained in 2 directions, and (d) an electron constrained in 3 directions. For an unconstrained electron, the density of states has a parabolic dependence on energy, dD/dE $\propto E^{1/2}$. For an electron constrained in one direction, the density of states has a step function-like dependence on energy, dD/dE $\propto$ const. For an electron confined in two dimensions, such as in a nanowire, dD/dE $\propto E^{-1/2}$. For an electron confined in three directions, such as in a quantum dot, the density of states function has a delta function-like dependence on energy, dD/dE $\propto \delta$E.For an electron confined in three directions, such as in a quantum dot, the density of states function has a delta function-like dependence on energy, dD/dE $\propto \delta$E. Adapted and printed with permission from Ref. 11 (Copyright 2010, Vaishno Dasika)........................................................................ 11

Figure 2.1: Schematic of plan-view and cross-sectional STM applied to a III-V heterostructure. The STM tip is brought within a few angstroms of the growth [001] (plan-view) or cleaved [110] (cross-sectional) face. ................................ 27

Figure 2.2: Tip and sample configurations in the (a) Omicron VT-STM and (b) Park Autoprobe VP2. The Omicron has a vertical configuration where the tip is facing up towards the sample, and the Park has a horizontal configuration, with the tip and sample oriented parallel to the floor. .......................................................... 28

Figure 2.3: (a) Park STM tip holder, designed to enable both STM and AFM. The STM tip is secured using a single screw, while specialized Si piezo-cantilevers for AFM are held in place by a metal clip, both marked by red arrows. (b) The Omicron tip holder and tip transfer plate. The STM tip is placed in the gold metal cylinder and secured by crimping. The tip holder is then magnetically secured to a tip transfer plate for transfer into the UHV chamber and for loading and unloading the tip from the scan head. The tip position and magnetic connector are marked by red arrows. .................................................................................................... 29

Figure 2.4: Simple demonstration of the Seebeck effect for electron-dominated conduction. The electrons respond to the applied temperature gradient and develop a steady-state voltage proportional to the applied temperature difference and the Seebeck coefficient of the material.......................................................................... 30

Figure 2.5: Schematic of SThEM setup: A room-temperature STM tip is brought into contact with a heated sample, generating a local thermoelectric voltage. Relays allow switching between measuring the thermoelectric voltage and the STM tunneling current. .......................................................................................... 31

Figure 2.6: (a) Back side of the SThEM sample plate and (b) side-view of the sample plate holder. In (a), the positions of the heater (red) and Si diode (grey) are shown. The electrical connections for the heater and Si diode are made using Pogo pins, mounted on the back of the sample. (b) The sample plate holder, where the Pogo pins make electrical contact with the receptor pins. The sample plate is held in place with clips, and a notch at the top of the sample plate holder assures firm contact between the Pogo pins and receptors. .................................................. 32

Figure 2.7: (a) The tip-sample resistance and (b) thermoelectric voltage measured between the tip and sample as a function of tip extension for a GaAs sample with Seebeck coefficient, S = 392 μV/K. Using the fine tip motion of the z-piezo extension, the tip is pressed further and further into the sample until solid electrical and thermal contact are established. In (a), after the tip is extended less than 100 nm, the electrical resistance has fallen into the kΩ range, indicating good electrical contact. (b) To determine the tip extension needed for good thermal contact, the tip is extended further until $V_{SThEM}$ reaches the value expected based on the known S, for a total tip extension of ~ 400 nm. ........................................................... 33

Figure 3.1: (a) Schematic of SThEM setup with room temperature ($T_{Tip}$) probe tip in contact with heated ($T_{Sample}$) sample, consisting of the cleaved (110) surface of a GaAs p-n junction. (b) Cross-sectional STM image of a p-n junction, with junction location defined by the black dashed line and SThEM tip trajectory defined by the white dotted line. (c) Dashed lines represent the targeted dopant profiles, assuming full activation of $Zn_{Ga}$ and $Si_{Ga}$; solid lines represent the redistributed dopant profiles following diffusion during GaAs growth at 580°C. Reprinted with permission from Ref. 1 (Copyright 2013, AIP Publishing LLC). ........................................................................................................................ 45

Figure 3.2: (a) Position-dependence of free electron (black) and hole (blue) concentrations calculated using the 1D Poisson equation for the diffused dopant profile in Fig 3.1(c). (b) Position-dependence of the measured thermoelectric voltage, $V_{SThEM}$, with the junction at x = 0. For comparison, the Seebeck coefficient computed using the free carrier concentration profile was used to determine the voltage profiles using the δT(r), 3D network, and quasi-3D conversion methods, labeled $V_{\delta T(r)}$, $V_{3D}$, and $V_{quasi\text{-}3D}$ in the plot. The most significant variations in $V_{SThEM}$ occur within 100 nm of the p-n junction interface, consistent with the estimated depletion width of 200 nm. The general agreement between the position-dependences of $V_{quasi\text{-}3D}$ and $V_{3D}$ suggests that the quasi-3D matrix approximation can be used in lieu of the 3D network simulation. Reprinted with permission from Ref. 1 (Copyright 2013, AIP Publishing LLC). ................................................ 46

Figure 3.3: Effective circuit diagram of the tip-sample contact point with position-independent conductances, G, and voltage sources connected in three directions perpendicular and two directions parallel to the p-n junction interface. For isotropic G, the voltage, $V_i$, is reduced to the average of V in the five directions. Reprinted with permission from Ref. 1 (Copyright 2013, AIP Publishing LLC). ........................................................................................................ 47

Figure 3.4: Position-dependence of $S_{quasi\text{-}3D}$, $S_{\delta T(r)}$, and $S_{Comp}$. $S_{quasi\text{-}3D}$ is in general agreement with $S_{Comp}$, while the magnitude of $S_{\delta T(r)}$ is generally smaller than $S_{Comp}$, especially in the vicinity of the interface. Reprinted with permission from Ref. 1 (Copyright 2013, AIP Publishing LLC). ................................................ 48

Figure 4.1: (a) Tapping mode AFM image of an uncapped InAs SK QD ensemble. (b) Plan-view STM image of an isolated QD used for the SThEM measurement. Due to the requirement of tip-sample contact during SThEM measurements, the tip often does not retain its atomic resolution. Thus, subsequent STM images typically do not exhibit atomic resolution. (c) Schematic of SThEM setup, which consists of a room temperature probe tip (i.e. $T_{Tip}$ = room temperature) in contact with a heated sample (i.e. $T_{Sample} > T_{Tip}$). The thermoelectric voltage at each tip-sample contact point is measured along the yellow dashed line shown in (b) and (c). Reprinted with permission from Ref. 1 (Copyright 2015, AIP Publishing LLC). .............. 64

Figure 4.2: Position-dependence of the local (a) indium fraction, $x_{In}$, (b) thermal conductivity, $\kappa_{sample}$, and (c) f-factor, f(x). To determine the In fraction profile across the SK QD in (a), we perform a 2D (x-z) moving average over 5 x 5 $nm^2$ regions of the In composition map in Ref. 28, followed by extraction of a 1D $x_{In}$ profile from a line cut through the QD center, defined as the position of highest $x_{In}$. The resulting averaged 1D $x_{In}$ profile and position-dependence of $\kappa_{sample}(x)$ are shown in (a) and (b), respectively. For (c), $\kappa_{sample}(x)$ was used as input into Eq. 4.2 to determine f(x). Reprinted with permission from Ref. 1 (Copyright 2015, AIP Publishing LLC). ........................................................................... 65

Figure 4.3: (a) $V_{SThEM}(x)$, the measured thermoelectric voltage, as a function of position across the QD, as shown in Fig. 4.1(b). $V_{SThEM}(x)$ is negative due to electron-dominated transport in the n-type semiconductor; $V_{SThEM}(x)$ reaches a maximum at $x \approx \pm 10$ nm, which corresponds to the edge of the QD. (b) S(x), the position dependence of the Seebeck coefficient, converted from the measured $V_{SThEM}(x)$ using Eq. 4.1. S(x) also exhibits maxima at the edges of the QD. (c) $E_C$-$E_F(x)$, the position dependence of the conduction band edge relative to the Fermi level, converted from S(x) using Eq. 4.3, where the Fermi level is defined at E = 0. $E_{C_1D}(x)$, plotted in blue, is calculated using a 1D Poisson-Schrodinger calculation of the band structure. The maxima in $E_C(x)$ at $x \approx \pm 10$ nm indicate the presence of band-bending at the QD/WL interfaces. Reprinted with permission from Ref. 1 (Copyright 2015, AIP Publishing LLC). ....................................................... 66

Figure 4.4: Position-dependence of the local (a) effective mass, m*(x), and (b) carrier concentration, n(x). m*(x) is determined using linear interpolations of the binary compound effective masses, $m^*_{InAs}= 0.023m_e$ and $m^*_{GaAs}= 0.067m_e$, and the profile of $x_{In}$ shown in Fig. 2(a). n(x) is converted from $E_C(x)$ using the m*(x) profile shown in (a) and Eq. 4.4. The values of n(x) inside the QD are 75% of those outside the QD, despite the intended uniform doping across all layers. Reprinted with permission from Ref. 1 (Copyright 2015, AIP Publishing LLC). ........ 67

Figure 4.5: (a) Reconstruction of laser-pulsed APT data of InAs/GaAs QDs superimposed on an SEM image of the tip. Indium atoms are shown in blue, where isosurfaces with indium concentration $x_{In} > 0.05$ appear yellow, revealing well-defined QD wetting layers. A cross-section of the reconstructed data of the InAs QD layers, (b) layer 3 (top), (c) layer 2 (middle), and (d) layer 3 (bottom). Yellow denotes an isosurface of $x_{In} > 0.25$, revealing QDs with diameters ~5-10 nm. Adapted and printed with permission from Ref. 35. (Copyright 2016, A.S. Chang). ............. 68

Figure 4.6: For each layer, the Si dopant concentration is analyzed in several areas: the GaAs spacer, a section of the WL not including QDs (WL defined by $x_{In} = 0.05$ isosurfaces), a section of the WL including QDs, and the QD only, defined by the x = 0.25 isosurfaces. Here the Si concentration is plotted as a function of growth layer. The Si concentration in the GaAs spacer (black) and WL not including QDs (red) is less than $5 \times 10^{18}$ cm$^{-3}$ and does not vary by layer. The Si concentration in the QDs (blue) is significantly larger than that in the GaAs spacer or WL, with values ranging from 1.2-2.2 x $10^{19}$ cm$^{-3}$, while the SThEM results suggest a reduced carrier concentration at the QD center. Therefore, it is possible that a fraction of Si atoms within the InAs QDs are electronically inactive or that carrier trapping within in the QDs is responsible for the decreased carrier concentration In the section of the WL including QDs (green), the Si concentration is in between that of the GaAs spacer and the QDs, but a clear correlation with layer is observed, where the Si concentration increases from the bottom layer to the top layer, which could indicate a saturation effect of the dopant concentration within single QDs. ........ 69

Figure 5.1: Schematic of $Sb_2Te_3$ film composition and laser irradiation method. (a) Cross-sectional view of the sample structure where the 100 nm $Sb_2Te_3$ film was grown on a *c*-plane sapphire substrate with a 10 nm $Bi_2Te_3$ buffer layer. (b) The sample is mounted on a translation stage and irradiated with a femtosecond laser (1560 nm, 150 fs) at a scan rate of 5 μm/s and fluence of 14 mJ/cm$^2$ at room temperature in ambient conditions. ........ 80

Figure 5.2: (a) STM image of the nanowires, revealing nanowires with diameters ~100 nm and separated by valleys of 50-100 nm. The color scale of this image represents a height difference Δz = 40 nm. (b) dI/dV as a function of bias voltage for the unmodified $Sb_2Te_3$ film (black) and the irradiated surface of the nanowires (red). dI/dV collected on the pristine $Sb_2Te_3$ reveals an effective band gap ~0.2 eV,

while dI/dV collected in the laser-irradiated region revealed an insulating phase, with a band gap in excess of 1.5 eV. ................................................................ 81

Figure 5.3: (a) Illustration of the different regions probed by SThEM and STS. STS probes the first few atomic layers of the surface, while SThEM is able to probe buried structures. (b) SThEM measurements taken in the unmodified region (left) reveal $V_{SThEM} = 2.15 \pm 0.1$ mV, and the measurements taken on the irradiated nanowires (right) $V_{SThEM} = 2.24 \pm 0.07$ mV. The errors represent the standard deviation of the data. Thus, $V_{SThEM}$ does not differ significantly between the irradiated and non-irradiated region. ......................................................................... 82

Figure 5.4: HAADF image of the $Sb_2Te_3$ nanowires. The top of the figure shows well-ordered bright spots, the nanowires, surrounded by a darker material. The bottom figure is zoomed in on this region, revealing a clear distinction between the nanowires and the surrounding insulating phase. Adapted and printed with permission from Ref. 1 (Copyright 2014, AIP Publishing LLC). ...................... 83

Figure 5.5: (a) Illustration of the locations probed by STS, including the valley between the nanowires and the regions on the surface of the nanowires not fully covered by the insulating phase. (b) dI/dV versus bias voltage of the valley (red) reveals an effective band gap in excess of 1.5 eV, consistent with the previous STS results. However, dI/dV of the nanowire surface (black) reveals an effective band gap ~ 0.2 eV, consistent with that of the unmodified $Sb_2Te_3$ film. Adapted and printed with permission from Ref. 1 (Copyright 2014, AIP Publishing LLC). ............. 84

Figure 6.1: Large-scale STM images of the surface topography for (a) 18 nm ($\Delta z = 9.5$ nm) (b) 30 nm ($\Delta z = 15.8$ nm), (c) 30 nm ($\Delta z = 9.8$ nm), and (d) 6 nm ($\Delta z = 15.5$ nm) films. For all samples, large terraces with 1 quintuple layer steps are observed, indicating high-quality layer-by-layer growth of the Van der Waals bonded layers. (d) has been adapted and reprinted with permission from Ref. 13 (Copyright 2016, AIP Publishing LLC). ......................................................................... 94

Figure 6.2: dI/dV as a function of bias voltage, corresponding to the energy relative to the Fermi level. The value of the bulk band gap is between 0.19-0.21 ± 0.10 eV, consistent with previous studies. The Fermi level is tuned across the gap, with an n-p transition occurring from composition B (x = 0.58) to composition C (x = 0.64). ......................................................................................................... 95

Figure 6.3: dI/dV of samples (a) B and (b) C as a function of bias voltage, corresponding to the energy relative to the Fermi level, $E_F$, revealing two distinct states of surface and bulk conduction. The bulk conduction (black) reveals an effective band gap of 0.20 (0.21) ± 0.10 eV for sample B (C). The surface state curves (red) were taken with a lower tunneling impedance, with the Dirac point, $E_D$, located between $E_F$ and the valence band edge for sample B (x = 0.58) and near the conduction band edge for sample C (x = 0.64). ............................................... 96

Figure 6.4: Resistivity vs. temperature for sample A (18 nm, blue), a sample similar to B (30 nm, red), and an 8 nm film (black). For thin films (8 nm), the resistance increases monotonically as a function of temperature, indicating conductive behavior. For thicker films (>18 nm), the resistivity decreases with temperature, indicating resistive behavior. 97

Figure 6.5: (a) RHEED intensity oscillations as a function of time and (b) an analysis of the streak spacing as a function of time. There is an increase in streak spacing around 275 s, corresponding to a decrease in the lattice constant which could indicate the presence of Bi intercalation resulting in a tsuomoite structure, giving way to the standard tetradymide structure later in the growth. (c) Cross-sectional view of the sample with the structure suggested by the electrical resistance and RHEED results. At the substrate/growth layer interface is a conductive layer, followed by an insulating layer of BiSbTe. The red lines indicate the topological surface states. 98

Figure 7.1: (a) STM topography image of a polished bulk skutterudite sample. The sample was reasonably flat over a range of µm¸ with Δz for this image ≈ 13 nm. (b) $V_{SThEM}$ as a function of position, measured across the dotted white line in (a). The SThEM measurement reveals a large variation of the $V_{SThEM}$, varying up to 33% from the mean, with a maximum variation of a factor of 6 across the sample, indicating significant inhomogeneity. 108

Figure 7.2: An ingot produced using SPS (top) will be sliced into disks. Each disk will be probed with SThEM (bottom), providing a map of the uniformity of SPS thermoelectric materials from a nanometer to millimeter scale. 109

Figure 7.3: (a) Schematic of the graphene nano-trench sample (b) Representative dI/dV measurements on the unpatterned graphene, at the edge of a trench, and in the area between trenches. The unpatterned graphene has no distinguishable bandgap, while the edge of the trench has a significantly larger bandgap than the area between trenches, presumably due to differing levels of strain. (c) STM image of a nano-trench and (d) the corresponding effective bandgaps as a function of position. The highest bandgaps are observed at the trench edges, presumably due to their high strain which maximizes the bandgap opening. 110

Figure A.1: Graphical user interface for the STS band gap calculation code. The user defines the linear regions of the valence and conductance band edges. 136

Figure B.1: Thermal model of SThEM. Assuming Q is constant, we model the sample as a series of thermal resistances and temperatures. There is a thermal resistance and temperature drop in the sample, the tip, and the tip-sample contact. 140

Figure B.2: f as a function of θ for a tungsten tip, $\kappa_W$=173 W/mK, and samples of thermal conductivities ranging from $\kappa_{GaAs}$= 55 W/mK to $\kappa_{BiTe}$=1.7W/mK. f increases with the ratio of $\kappa_{Tip}/\kappa_{Sample}$ and with the tip angle $\theta_{Tip}$. The values of the f factor

calculated using Eq. B.9 and measured for GaAs and $Sb_2Te_3$ samples of known S are marked with blue and red x's, respectively. The calculated and measured values of $f_{GaAs}$ agree well, but there is nearly a factor of 2 discrepancy between the calculated and measured values of $f_{SbTe}$. .................................................. 141

Figure D.1: Overview of STM and SThEM electronics in the modified Park Autoprobe VP2. ......................................................................................................... 146

Figure D.2: SThEM breakout box schematic diagram. Two relays disconnect the sample bias and tunneling current to instead measure the thermoelectric voltage, $V_{SThEM}$. The breakout box is connected between the STM and the pre-amplifier externally to the UHV chamber by 10 pin military connectors........................................ 147

Figure F.1: VI front panel for the SThEM acquisition program. The user sets the delay times before beginning acquisition of the voltage or resistance readings and the number of readings to take. The program calculates the average and standard deviation of these readings and plots them in the graph on the right of the VI.151

Figure G.1: Plots of normalized $V_{SThEM}$ as a function of position for (a) a GaAs p-n junction, (b) an InAs/GaAs quantum dot, (c) an In island on GaAs, and (d) $Sb_2Te_3$ nanotracks, with the height profile across the SThEM trajectory for each STM image. For all measurements, the corresponding STM image is included with the trajectory noted with a yellow dashed line. .................................................... 154

Figure J.1: (a) 2D image of the local gradient of the AFM surface topography (b) Frequency as a function of QD diameter fit with a Gaussian distribution ($R^2$=0.99), revealing a mean diameter of 28 ± 11 nm. ...................................................................... 174

Figure J.2: STS measurement of dI/dV as a function of bias voltage on the oxidized surface of the InAs/GaAs QD sample. The voltages correspond to the energy relative to the Fermi level. The spectra display well-defined band edges, with effective band-gap values > 2 eV. We note the absence of electronic states in the vicinity of the Fermi level. The valence and conduction band edges are marked with vertical dashed lines on the left and right, respectively................................................ 175

Figure J.3: SThEM data for p-type GaAs as a function of the temperature difference between the tip and sample, $\Delta T = T_{Sample} - T_{Tip}$. A linear least-squares fit to $V_{SThEM}$ vs. $\Delta T$ reveals a slope of 0.089, corresponding to an S-value of 270 μV/K. The correlation coefficient value of 0.99 confirms the linear dependence of $V_{SThEM}$ on $\Delta T$, and the resulting temperature-independence of S. ................................... 176

Figure J.4: To determine the position-dependent indium composition, we consider a 2D composition map consisting of the in-plane, x, and out-of-plane, z, directions, where z is the growth direction, where $x_{In}$ ranges from 0.15 in the WL to 0.65 at the center of the QD. We perform a 2D (x-z) moving average over 5 x 5 $nm^2$

regions, as marked by the black square, followed by extraction of a 1D $x_{In}$ profile from a line cut through the QD center, marked by the black dashed line. ....... 177

Figure J.5: (a) Varying $x_{In}$ profiles, including with values equal to those used in Section 4.5 (black squares), with values 10% higher (green triangle) or 10% lower (red circle), as well as a more gradual spatial profile (blue inverted triangle). The resulting S and n profiles are shown in (b) and (c), respectively. .................... 178

Figure J.6: (a) Varying $x_{In}$ profiles, including with values equal to those used in Section 4.5 (black squares), with constant $x_{In}$ values, $x_{In}$ = 0.2 (green triangle), $x_{In}$ = 0.5 (cyan diamond), and $x_{In}$ = 0.8 (blue inverted triangle), and with values for a pure InAs/GaAs quantum well (red circle). The resulting S and n profiles are shown in (b) and (c), respectively. ....................................................................... 179

Figure K.1: Mass spectra collected in (a) voltage and (b) laser modes, with various peaks of Ga and As labeled in both. The peaks collected in laser mode are better defined, and high mass peaks are successfully detected. (c) Zoomed-in section of the mass spectrum at the location of the Si peak where horizontal red line is the background noise level calculated by the IVAS software. Thus, the Si dopant peak is significantly above the background. ................................................................ 183

Figure K.2: Reconstruction explorer interface where the image compression factor and detector efficiency are then varied until the QD layers have minimum curvature, and the spacing between layers matches the value expected from the MBE growth. The parameters on the left side are modified and the results examined in real time in the reconstruction explorer on the right. ..................................................... 184

Figure K.3: Si dopant analysis procedure. (a) First, a cube with a volume of 1710 $nm^3$ is created in the region of interest. (b) Next, a new POS file is created from the cube and the composition is analyzed using the "background corrected" option. For the QD only analysis, a slightly modified procedure is used. Instead of a cube, the $x_{In}$=0.25 isosurface of the QD is used to create the new POS file, analyzing only the atoms inside the QD. ...................................................................... 185

## List of Appendices


Appendix A Scanning tunneling spectroscopy data analysis ........................................112

Appendix B 1D Fourier model and f-factor..................................................................137

Appendix C Materials parameters ..................................................................................142

Appendix D SThEM modifications ..................................................................................145

Appendix E Modifications to the RHK SPM controller ................................................148

Appendix F SThEM data acquisition................................................................................150

Appendix G Influence of sample geometry on SThEM measurements ..........................152

Appendix H Poisson-Schrodinger calculations .............................................................155

Appendix I Quasi-3D deconvolution ...............................................................................158

Appendix J InAs quantum dot supplementary information ...........................................170

Appendix K Atom probe tomography reconstruction and analysis................................180

## Abstract

**Probing the band structure and local electronic properties of low-dimensional semiconductor structures**
**by**

**Jenna Cherie Walrath**

**Chair: Rachel S. Goldman**

Low-dimensional semiconductor structures are important for a wide variety of applications, including thermoelectric generators, laser diodes, photovoltaics, and topological spintronic devices. Recent advances in nanoscale fabrication are paving the way for increasingly precise nano-engineering of a wide range of materials. It is therefore essential that the physics of materials at the nanoscale are thoroughly understood to unleash the full potential of nanotechnology, requiring the development and utilization of increasingly sophisticated instrumentation and modeling.

Of particular interest is understanding the relationship between the local density of states (LDOS) of low-dimensional structures and the band structure and local electronic properties. The dependence of the LDOS on energy changes significantly with reduced dimensionality; for an unconstrained electron, the density of states has a parabolic dependence on energy, $dD/dE \propto E^{1/2}$, while an electron confined in three directions, such as in a quantum dot, has a delta function-like dependence on energy, $dD/dE \propto \delta E$. This dissertation presents the investigation of the band structure, local density of states, and

local electronic properties of nanostructures ranging from zero-dimensional (0D) quantum dots to two-dimensional (2D) thin films, synthesizing computational and experimental approaches including Poisson-Schrodinger band structure calculations, scanning tunneling microscopy (STM), scanning tunneling spectroscopy (STS), and scanning thermoelectric microscopy (SThEM).

A method is presented for quantifying the local Seebeck coefficient with scanning thermoelectric microscopy, using a direct approach to convert temperature gradient-induced voltages to Seebeck coefficients (S). We use a quasi-3D conversion matrix that considers both the sample geometry and the temperature profile. For a GaAs p-n junction, the resulting S-profile is consistent with that computed using the free carrier concentration profile. This combined computational-experimental approach is expected to enable nanoscale measurements of S across a wide variety of heterostructure interfaces. Although deconvolutions based on tip geometries are often used to enhance lateral resolution of scanning probe measurements, this is the first deconvolution which allows direct conversion of a measured proxy quantity to the quantity of interest. Therefore, this approach could be extended to other techniques such as scanning voltage microscopy and scanning spreading resistance microscopy.

The local carrier concentration, n, is profiled across epitaxial InAs/GaAs quantum dots (QDs) consisting of 3D islands on top of a 2D alloy layer. SThEM is used to profile the temperature gradient-induced voltage, which is converted to a profile of the local Seebeck coefficient, S. The S profile is then converted to a conduction band-edge profile and compared with Poisson-Schrodinger band-edge simulations. The combined computational-experimental approach suggests a reduced carrier concentration in the QD

center in comparison to that of the 2D alloy layer. The relative roles of free carrier trapping and/or dopant expulsion are discussed. We further use 3D atom probe tomography to profile the distribution of Si dopants. Preliminary data indicates a higher Si dopant concentration within the QDs than in the surrounding WL, with an increase in the number of dopants in the vicinity of the QD with increasing growth layer. This work is the first measurement of a carrier concentration across a single quantum dot, and this approach can be applied to a wide range of semiconductor heterostructures, providing key insight necessary for achieving nanostructured semiconductor device design goals.

The surface composition and band structure of ordered horizontal $Sb_2Te_3$ nanowires induced by femtosecond laser irradiation of a thin film are investigated. Initial STM and STS studies revealed a widened band gap in the nanowire region, but SThEM indicates the thermopower of the nanowires remained unchanged from pristine $Sb_2Te_3$, suggesting the presence of an insulating material surrounding buried nanowires. Subsequent cross-sectional transmission electron microscopy studies confirmed the presence of single-crystal $Sb_2Te_3$ nanowires surrounded by a polycrystalline material, but revealed gaps in this material in some areas of the nanowire surface that could be probed directly using STS. Thus, a more targeted STS study directly measured the band gap modulation between the nanowires and insulating material. These horizontal $Sb_2Te_3$ nanowires are promising for a variety of applications, including thermoelectrics and optoelectronics, and the novel fabrication method using fs laser-irradiation in ambient conditions provides a pathway for scalable manufacturing.

Finally, scanning tunneling microscopy and spectroscopy (STM/STS) are used to investigate the band structure of $(Bi_{1-x}Sb_x)_2Te_3$ alloys at room temperature, revealing both

the Fermi level and Dirac point located inside the bulk bandgap, indicating bulk-like insulating behavior with accessible surface states. Prior to this work, direct detection of topological surface states in BiSbTe systems has been achieved for only $T < 10$ K. However, for device applications, room-temperature identification of topological surface states is needed. This work demonstrates the first direct measurement of topological surface states using STS at room temperature for any material. Additionally, we discuss the alloy composition and film thickness dependence of the band structure and transport properties, showing evidence for a conductive interface layer beneath the insulating bulk. Thus, while alloying can be used to achieve tunable surface states, the film/substrate interface needs to be carefully considered to achieve an insulating bulk.

# Chapter 1

# Introduction

## 1.1 Overview

Low-dimensional semiconductor structures are important for a wide variety of applications, including thermoelectric generators, laser diodes, photovoltaics, and topological spintronic devices. Recent advances in nanoscale fabrication are paving the way for increasingly precise nano-engineering of a wide range of materials. It is therefore essential that the physics of materials at the nanoscale are thoroughly understood to unleash the full potential of nanotechnology, requiring the development and utilization of increasingly sophisticated instrumentation and modeling.

Of particular interest is understanding the relationship between the local density of states (LDOS) of low-dimensional structures and the resulting band structure and local electronic properties. The dependence of the LDOS on energy changes significantly with reduced dimensionality; for an unconstrained electron, the density of states has a parabolic dependence on energy, $dD/dE \propto E^{1/2}$, while an electron confined in three directions, such as in a quantum dot, has a delta function-like dependence on energy, $dD/dE \propto \delta E$. This dissertation presents the investigation of the band structure, local density of states, and

local electronic properties of nanostructures ranging from zero-dimensional (0D) quantum dots to two-dimensional (2D) thin films, synthesizing computational and experimental approaches including Poisson-Schrodinger band structure calculations, scanning tunneling microscopy (STM), scanning tunneling spectroscopy (STS), and scanning thermoelectric microscopy (SThEM).

Specifically, the following projects will be described in this dissertation: (1) development of a quasi-3D matrix method to directly convert the measured thermoelectric voltage to a local measurement of the Seebeck coefficient and demonstration of this technique on a SThEM measurement across a GaAs p-n junction. (2) 0D: Use of SThEM to probe the thermoelectric voltage cross a single InAs quantum dot and converted this to a profile of the local carrier concentration across the quantum dot and wetting layer. (3) 1D: STM/S and SThEM investigation of the surface composition and band structure of ordered horizontal $Sb_2Te_3$ nanowires (4) 2D: Investigation of the band structure of topologically insulating BiSbTe thin film alloys using STM/S to directly detect topological surface states at room temperature.

This chapter explores the current opportunities, challenges, and applications presented by low-dimensional semiconductor structures and presents an overview of the methods available for studying nanostructured materials, followed by a description of the dissertation organization.

## 1.2 Low-dimensional structures for enhanced thermoelectric efficiency

As global energy demands are rapidly increasing, the need for sustainable clean energy sources driven by scientific research is greater than ever. However, in any energy-producing or utilizing system, heat loss is a barrier to efficiency. Thermoelectric (TE) devices offer a method of recovering waste heat through solid state conversion of heat to electricity. However, typical efficiencies of TE devices are 5-10% which constitutes a barrier to widespread use.

Low-dimensional thermoelectric materials may provide the key to increased efficiencies. The efficiency of a TE device is given by the dimensionless figure of merit

$$ZT = \frac{S^2\sigma}{\kappa}T \tag{1.1}$$

where S is the Seebeck coefficient (also known as the thermopower), T is the temperature, and σ (κ) is the electrical (thermal) conductivity. As ZT approaches infinity, the thermoelectric device efficiency approaches the Carnot efficiency. For a thermoelectric device to be considered competitive, it must have ZT > 1 in the operable temperature range.[1] Most processes that increase S also decrease σ, and increasing σ tends to increase κ, negating the benefits in either case. However, it has been proposed that nanostructuring materials in the form of thin films, superlattices, nanowires, or quantum dots has the potential to increase ZT. Much of this work has focused on reducing κ while preserving σ as a result of the Phonon-Glass-Electron-Crystal concept;[2] however, in bulk materials, the phonon mean free path cannot become shorter than the interatomic distance, thereby limiting the potential improvements in ZT through reduction of κ.[3]

Alternatively, an increase in the Seebeck coefficient has been predicted for low dimensional structures, due to a modification in the LDOS, by means of reduced dimensionality[4,5] or introduction of resonant states,[6] and/or through energy-dependent scattering processes that render an energy-dependent carrier mobility, μ[7]. The Van Hove singularities in the LDOS of these low-dimensional structures are responsible for the predicted enhancement of the Seebeck coefficient, as evidenced by the Mott relation[8,9] which reveals that

$$S \propto \left. \frac{d[\ln D(E)\tau(E)]}{dE} \right|_{E_F} \tag{1.2}$$

where D is the density of states, τ is the scattering parameter, and $E_F$ is the Fermi energy. Figure 1.1 illustrates the Van Hove singularities, showing the energy dependence of the ideal electronic density of states for (a) a free electron gas, (b) an electron confined in one dimension, as in a quantum well, (c) an electron confined in two dimensions, as in a quantum wire, and (d) an electron confined in three dimensions, as in a quantum dot.[10,11]

Thus, all of the nanostructures investigated in this dissertation are potentially promising for thermoelectric devices. For example, quantum dots have been predicted to have significantly enhanced thermoelectric efficiency.[12] In the work presented in Chapter 4 on InAs quantum dots, the goal was to directly measure a correlation between quantum confinement and an enhanced power factor. While the Fermi level was too far from the quantum confined states to observe such an enhancement, the author was able to instead use SThEM as a method to conduct the first ever profile of carrier concentration across a single quantum dot, with implications far beyond thermoelectric applications, as described in the following section.[13]

### 1.3 Self-assembled semiconductor quantum dots

Self-assembled semiconductor quantum dots (QDs) are promising materials for a variety of solid-state applications, including solar cells,[14,15] lasers,[16] photodetectors,[17,18] light-emitting diodes,[19,20] and thermoelectric generators.[21] However, a variety of issues plague quantum dot optoelectronic devices such as non-radiative carrier recombination, carrier trapping, and dark current.[22,23] Furthermore, QD non-uniformities such as inhomogeneous dot size, density, composition, and doping lead to inhomogeneous broadening of the density of states, lowering the device efficiency. Further advances will require an improved understanding and control of dot morphology and the influence on the density of states and resulting electronic properties on a nanometer scale. Due to the practical and fundamental limitations of existing local probe techniques, [24] understanding and manipulating the local electronic properties of QDs, such as the carrier concentration (n), remains challenging. A novel scanning probe technique called scanning thermoelectric microscopy (SThEM) enables nanoscale measurements of the Seebeck coefficient (S), which then can be converted a profile of the local carrier concentration. This technique allows carrier concentration profiling across single nanostructures, such as QDs, with nm resolution, which no other current technique can currently accomplish.

### 1.4 Topological insulators

Topological insulators (TIs) have emerged as an exciting class of quantum materials, which possess an insulating bulk and metallic, spin-polarized surface states that

arise from time-reversal symmetry breaking. Spin-polarization in topological surface states has two primary consequences: (1) The orientation of the spin can be controlled by reversing the direction of the applied current, opening up a wide range of potential applications including quantum computing and spintronic devices, and (2) spin-momentum locking suppresses backscattering, resulting in ultra-high carrier mobility.[25-28] Many recently discovered topological insulators are also well-known thermoelectric materials, such as $Bi_2Te_3$, $Sb_2Te_3$, and related compounds. It has been proposed that these highly mobile surface states may be capitalized upon to enhance thermoelectric efficiency by carefully tuning the interactions between the surface and bulk states.[29-31]

The $Sb_2Te_3$ nanowires presented in Chapter 5 and the alloys of $Bi_2Te_3$ and $Sb_2Te_3$ presented in Chapter 6 are of particular interest for topological insulator applications for several reasons. First, the presence of topological surface states in $Bi_2Te_3$, $Sb_2Te_3$, and BiSbTe alloys has been well established through angle resolved photoemission spectroscopy (ARPES),[32] STS,[33] and transport measurements.[34] Second, since the band gaps of both $Sb_2Te_3$ and BiSbTe are sufficiently larger than $k_BT$ ($E_g$ >>26 meV), room-temperature applications may be within reach.[32,35] Furthermore, in the case of BiSbTe, the growth of high-quality ultra-thin and flat $Bi_2Te_3$-based films has already been demonstrated,[36-38] Finally, alloying $Bi_2Te_3$ and $Sb_2Te_3$ has been reported to induce a mid-gap Dirac point and Fermi level, allowing a decoupling of bulk and surface transport.[32,39]

### 1.5 Methods for examining the structural and electronic properties of materials

Various techniques are available for the investigation of structural and electronic properties in low dimensional semiconductor structures, including high-resolution transmission electron microscopy (TEM), plan-view and cross-sectional scanning tunneling microscopy [(X)STM], photoluminescence (PL) spectroscopy, scanning tunneling spectroscopy (STS), capacitance-voltage (C-V) spectroscopy, and angle-resolved photoemission spectroscopy (ARPES). While high resolution TEM often has a lateral resolution on the order of angstroms, the data is averaged across ~10-100 nm and is not directly sensitive to the electronic structure.[40] In contrast, plan-view and cross sectional scanning tunneling microscopy allow direct observations of the spatial distribution of individual atoms on the surface and is inherently sensitive to the electronic states of the material.[41-46] One of the main advantages of STM is that the collected images are associated primarily with the top layer of the surface of interest, instead of an average over many layers as is typical for TEM.

For investigating the electronic structure of nanostructures, C-V and PL are commonly used techniques. However, C-V spectroscopy typically requires applying bias voltage to a heterostructure, thereby modifying the depletion width in the heterostructure. Furthermore, the data typically corresponds to a spatial average over 10's-100's of microns, so the spatial resolution for this measurement technique is limited.[47-50] PL is commonly employed to measure the band gap of materials. However, PL measurements are typically limited by the fast decay times of the excited carriers and provide information only on the energy difference between the ground states of the carriers.[51] Furthermore, PL

data corresponds to a spatial average relying on several assumptions, such as interface abruptness, alloy composition, and film quality.[51,52] Additionally, APRES is a technique in which the surface density of states (DOS) is imaged in momentum space; however, it is not possible to probe states above the Fermi level with ARPES.

STS, which allows spatially-resolved electronic measurements within single layers of semiconductors, is a promising alternative to methods such as C-V and PL. While STS can only probe the band structure at a single point in momentum space, both filled and empty states can be probed with STS, in contrast to ARPES. Additionally, a novel scanning probe technique called scanning thermoelectric microscopy (SThEM) enables nanoscale measurements of the S. Since S is fundamentally related to the DOS in the vicinity of the Fermi level, information about the band structure and the LDOS can be extracted from SThEM data. SThEM measurements are not limited to the topmost atomic layer which STS is most sensitive to, and thus SThEM data can provide information about structures within a few nanometers of the surface, such as nanostructures buried beneath an oxide layer. Thus, (X)STM, STS, and SThEM provide a powerful suite of tools for investigating the relationships between the band structure, local density of states, and local electronic properties of nanostructures.

### 1.6 Dissertation Organization

This dissertation is organized as follows. In Chapter 2, the experimental procedures used for the growth and characterization of the GaAs p-n junction, InAs QD, $Sb_2Te_3$ nanowires, and BiSbTe thin films are described. Film growth by molecular beam epitaxy

(MBE) and the characterization tools used, including SThEM, STM, and STS, are described in detail.

Chapter 3 presents a method for quantifying the local Seebeck coefficient with SThEM, using a direct approach to convert temperature gradient-induced voltages to Seebeck coefficients (S). We use a quasi-3D conversion matrix that considers both the sample geometry and the temperature profile. For a GaAs p-n junction, the resulting S-profile is consistent with that computed using the free carrier concentration profile. This combined computational-experimental approach is expected to enable nanoscale measurements of S across a wide variety of heterostructure interfaces.

In Chapter 4, the local carrier concentration, n, is profiled across epitaxial InAs/GaAs quantum dots (QDs) consisting of 3D islands on top of a 2D alloy layer. We use SThEM to measure a profile of the temperature gradient-induced voltage, which is converted a profile of the local S. The S profile is then converted to a conduction band-edge profile and compared with Poisson-Schrodinger band-edge simulations. The combined computational-experimental approach suggests a reduced carrier concentration in the QD center in comparison to that of the 2D alloy layer. We further use 3D atom probe tomography to profile the distribution of Si dopants. The correlation between the Si dopant distribution and the observed carrier concentration profile is discussed.

Chapter 5 presents STM/S and SThEM investigations of the surface composition and band structure of ordered horizontal $Sb_2Te_3$ nanowires induced by femtosecond laser irradiation of a thin film. Initial STM and STS studies revealed a widened band gap in the nanowire region compared to pristine $Sb_2Te_3$, but SThEM indicated the thermoelectric voltage of the nanowires remained unchanged from pristine $Sb_2Te_3$, suggesting the

presence of an insulating material surrounding buried nanowires. Subsequent cross-sectional transmission electron microscopy (X-TEM) studies confirmed the presence of single-crystal $Sb_2Te_3$ nanowires surrounded by a polycrystalline material, but revealed gaps in this material in some areas of the nanowires. Subsequently, a more targeted STS study directly measured the band gap modulation between the nanowires and insulating material.

In Chapter 6, STM and STS are used to investigate the band structure of $(Bi_{1-x}Sb_x)_2Te_3$ alloys at room temperature, revealing both the Fermi level and Dirac point located inside the bulk bandgap, indicating bulk-like insulating behavior with accessible surface states. Additionally, we discuss the alloy composition and film thickness dependence of the band structure and transport properties, showing evidence for a conductive interface layer beneath the insulating bulk. Thus, while alloying can be used to achieve tunable surface states, the film/substrate interface needs to be carefully considered to achieve an insulating bulk.

Finally a summary and suggestions for future work are presented in Chapter 7.

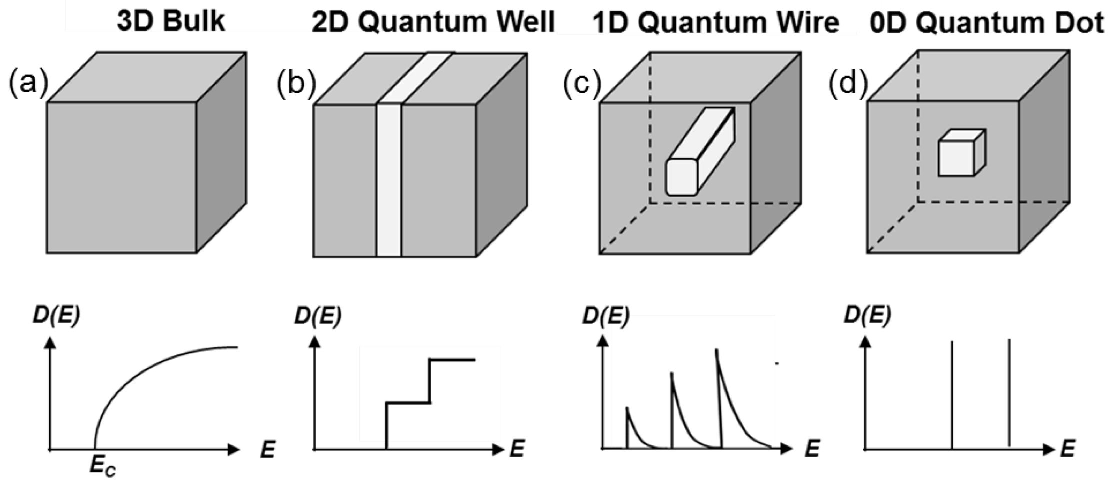


Figure 1.1: Energy dependence of the density of states for (a) an ideal free electron gas, (b) an electron free in 2 directions but constrained in 1 direction, (c) an electron free in 1 direction and constrained in 2 directions, and (d) an electron constrained in 3 directions. For an unconstrained electron, the density of states has a parabolic dependence on energy, $dD/dE \propto E^{1/2}$. For an electron constrained in one direction, the density of states has a step function-like dependence on energy, $dD/dE \propto$ const. For an electron confined in two dimensions, such as in a nanowire, $dD/dE \propto E^{-1/2}$. For an electron confined in three directions, such as in a quantum dot, the density of states function has a delta function-like dependence on energy, $dD/dE \propto \delta(E)$. Adapted and printed with permission from Ref. 11 (Copyright 2010, Vaishno Dasika).

## 1.7 References


[1] H. J. Goldsmid, *Thermoelectric Refrigeration*, Plenum Press, New York (1964).

[2] G. A. Slack, *Handbook of Thermoelectrics*, CRC Press, Boca Raton, FL (1995), Chap. 34.

[3] G. A. Slack, *Solid State Physics*, Vol. 34, H. Ehrenreich, F. Seitz, D. Turnbull, Eds. Academic Press, New York (1979), pp. 1–71.

[4] L.D. Hicks and M.S. Dresselhaus, *Phys. Rev. B* **47**, 19, 12727 (1993).

[5] L.D. Hicks and M.S. Dresselhaus, *Phys. Rev. B* **47**, 24, 16631 (1993).

[6] J. P. Heremans, V. Jovovic, E. S. Toberer, A. Saramat, K. Kurosaki, A. Charoenphakdee, S. Yamanaka, G. J. Snyder, *Science*, **321** 554 (2008).

[7] J. P. Heremans, C. M. Thrush, and D. T. Morelli, *J. Appl. Phys.* **98**, 063703 (2005).

[8] A. Shakouri, *Annu. Rev. Mater. Res.* **41**, 399 (2011).

[9] The full Mott relation is $S \propto \frac{\pi^2 k_B}{3q} k_B T \left.\frac{d(\ln \sigma(E))}{dE}\right|_{E_F}$

[10] D. Bimberg, M. Grundmann, and N. N. Ledenstov, *Quantum Dot Heterostructures*. (John Wiley & Sons Ltd, West Sussex, 2001).

[11] V. Dasika, Ph.D. Thesis, University of Michigan, 2010.

[12] G. D. Mahan and J. O. Sofo, *Proc. Natl. Acad. Sci.* **93** 7436 (1996).

[13] J. C. Walrath, Y. H. Lin, S. Huang, and R. S. Goldman, *Appl. Phys. Lett.* **106**, 192101 (2015).

[14] A. Marti, E. Antolin, C. R. Stanley, C. D. Farmer, N. Lopez, P. Diaz, E. Canovas, P. G. Linares, and A. Luque, *Phys. Rev. Lett.* **97**, 247701 (2006).

[15] S. Huang, A. V. Semichaevsky, L. Webster, H. T. Johnson, and R. S.Goldman, *J. Appl. Phys.* **110**, 073105 (2011).

[16] L. Huffaker, G. Park, Z. Zou, O. B. Shchekin, and D. G. Deppe, *Appl. Phys. Lett.* **73**, 2564 (1998).

[17] J. Phillips, K. Kamath, and P. Bhattacharya, *Appl. Phys. Lett.* **72**, 2020 (1998).

[18] Z.Y. Zhao, C. Yi, K.R. Lantz, and A.D. Stiff-Roberts, *Appl. Phys. Lett.* **90**, 233511 (2007).

[19] N. M. Park, T. S. Kim, and S. J. Park, *Appl. Phys. Lett.* **78**, 2575 (2001).

[20] J. X. Chen, A. Markus, A. Fiore, U. Oesterle, R. P. Stanley, J. F. Carlin, R. Houdre, M. Ilegems, L. Lazzarini, L. Nasi, M.T. Todaro, E. Piscopiello, R. Cingolani, M. Catalano, J. Katcki, and J. Ratajczak, *J. Appl. Phys.* **91**, 6710 (2002).

[21] G.D. Mahan and J.O. Sofo, *Proc. Natl. Acad. Sci.* **93** 7436 (1996).

[22] W. K. Bae, S. Brovelli and V. I. Klimov, *MRS Bulletin*, 38, pp 721-730 (2013).

[23] A.D. Stiff-Roberts, *IEE-NANO*, 444 (2009).

[24] P. De Wolf, R. Stephenson, T. Trenkler, T. Clarysse, T. Hantschel, and W. Vandervorst, *J. Vac. Sci. Technol., B* **18**, 361 (2000).

[25] Y.L. Chen, J.G. Analytis, J.H. Chu, Z.K. Liu, S.K. Mo, X.L. Qi, H.J. Zhang, D.H. Lu, X. Dai, Z. Fang, S.C. Zhang, I.R. Fisher, Z. Hussain, and Z.X. Shen, *Science* **325**, 178 (2009).

[26] D.X. Qu, Y.S. Hor, J. Xiong, R.J. Cava, and N.P. Ong, *Science* **329**, 5993 (2010).

[27] K. Hoefer, C. Becker, D. Rata, J. Swanson, P. Thalmeier, and L.H. Tjeng, *PNAS* **111**, 14979 (2015).

[28] W. Liu, H. Chi, J. C. Walrath, A.S. Chang, V. A. Stoica, L. Endicott, X. Tang, R. S. Goldman, and C. Uher, *Appl. Phys. Lett.* **108**, 043902 (2016).

[29] Y. Xu, Z.X. Gan, and S.C. Zhang, *Phys. Rev. Lett.* **112**, 226801 (2014).

[30] D.J. Singh, *Phys. Rev. B* **81**, 195217 (2010).

[31] J.S. Zhang, X. Feng, Y. Xu, M.H. Guo, Z.C. Zhang, Y.B. Ou, Y. Feng, K. Li, H.J. Zhang, L.L. Wang, X. Chen, Z.X. Gan, S.C. Zhang, K. He, X.C. Ma, Q.K. Xue, and Y.Y. Wang, *Phys. Rev. B* **91**, 075431 (2015).

[32] J.S. Zhang, C.Z Zhu, Z.C. Zhang, J. Wen, X. Feng, K. Li, M.H. Liu, K. He, L.L. Wang, X. Chen, Q.K. Xue, X.C. Ma, and Y.Y. Wang, *Nature Commun.* **2**, 574 (2011).

[33] Y. Jiang, Y.Y. Sun, M. Chen, Y. Wang, Z. Li, C. Song, K. He, L. Wang, X. Chen, Q.K. Xue, X. Ma, and S.B. Zhang, *Phys. Rev. Lett*. **108**, 066809 (2012).

[34] D.X. Qu, Y.S. Hor, J. Xiong, R.J. Cava, and N.P. Ong, *Science* **329**, 5993 (2010).

[35] L. Liu, A. Richardella, I. Garate, Y. Zhu, N. Samarth, and C.T. Chen, *Phys. Rev. B* **91**, 235437 (2015).

[36] K. Hoefer, C. Becker, D. Rata, J. Swanson, P. Thalmeier, and L.H. Tjeng, *PNAS* **111**, 14979 (2015).

[37] S.E. Harrison, S. Li, Y. Huo, B. Zhou, Y.L. Chen, and J.S. Harris, *Appl. Phys. Lett.* **102**, 171906 (2013).

[38] N. Bansal, Y.S. Kim, M. Brahlek, E. Edrey, and S. Oh, *Phys. Rev. Lett.* **109**, 116804 (2012).

[39] X. He, H. Li, L. Chen, and K. Wu, *Sci. Rep.* **5**, 8830 (2015).

[40] A. Neubauer, F. Kuchar, H. Heinrich, *Low-Dimensional Electronic Systems: New Concepts* 111, Springer-Verlag Berlin Heidelberg (1992).

[41] T. Tsuruoka and S. Ushioda, *J. Electron Microsc.* **53**, 169 (2004).

[42] R. J. Hamers, *Annu. Rev. Phys. Chem.* **40**, 531 (1989).

[43] B. Lita, Ph.D. Thesis, University of Michigan, 2001.

[44] O. Albrektsen, Ph.D. Thesis, Technical University of Denmark, 1990.

[45] R. M. Feenstra, *Semicond. Sci. Technol.* **9**, 2157 (1994).

[46] R. S. Goldman, *J. Phys. D* **37**, 163 (2004).

[47] K. H. Schmidt, G. Medeiros-Ribeiro, M. Oestreich, P. M. Petroff, and G. H. Döhler, *Phys. Rev. B* **54**, 11346 (1996).

[48] G. Medeiros-Ribeiro, D. Leonard, and P. M. Petroff, *Appl. Phys. Lett.* **66**, 1767 (1995).

[49] P. Blood, *Semicond. Sci. Technol.* **1**, 7 (1986).

[50] P. N. Brounkov, A. Polimeni, S. T. Stoddart, M. Henini, L. Eaves, P. C. Main, A. R. Kovsh, Y. G. Musikhin, and S. G. Konnikov, *Appl. Phys. Lett.* **73**, 1092 (1998).

[51] K. H. Schmidt, G. Medeiros-Ribeiro, M. Oestreich, P. M. Petroff, and G. H. Döhler, *Phys. Rev. B* **54**, 11346 (1996).

[52] P. N. Brounkov, A. Polimeni, S. T. Stoddart, M. Henini, L. Eaves, P. C. Main, A. R. Kovsh, Y. G. Musikhin, and S. G. Konnikov, *Appl. Phys. Lett.* **73**, 1092 (1998).

# Chapter 2

# Experimental Procedures

## 2.1 Overview

This chapter describes the experimental procedures used for the fabrication and characterization of the low-dimensional structures examined in this thesis. All samples were grown by molecular beam epitaxy (MBE), and their structures were examined using scanning tunneling microscopy (STM). Scanning tunneling spectroscopy (STS) was used to measure the band structure of the InAs QDs, $Sb_2Te_3$ nanowires, and the topologically-insulating BiSbTe thin films. Furthermore, scanning thermoelectric microscopy (SThEM) was used to probe the thermoelectric voltage across the GaAs p-n junction, InAs QD, $Sb_2Te_3$ nanowires presented in this dissertation.

## 2.2 Molecular Beam Epitaxy (MBE)

MBE involves the sublimation or evaporation of solid sources, followed by the deposition of atoms or molecules on the growth surface via reaction and condensation of the molecular beams to produce high quality epitaxial films.[1,2] The GaAs p-n junction described in Chapter 3 was grown in the Goldman MBE lab at the University of Michigan by Dr. R. L. Field III. In Chapter 4, the InAs QD samples for SThEM and APT were grown

by Dr. S. Huang, Mr. D. Del Gaudio, and Mr. T. Jen. The $Sb_2Te_3$ and BiSbTe thin films described in Chapters 5 and 6 were grown by Dr. V.A. Stoica, Dr. W. Liu, and Mr. L. Endicott in the laboratory of Professor Ctirad Uher at the University of Michigan, in collaboration with Professor Roy Clarke. Details of the sample structures and growth procedures will be given in the respective chapters, including the $Sb_2Te_3$ nanowire fabrication by Dr. Y. Li.

### 2.3 Scanning Tunneling Microscopy (STM)

In this section, an overview of plan-view and cross-sectional scanning tunneling microscopy (STM and XSTM) is provided. The XSTM experiments on the GaAs p-n junction discussed in Chapter 3 and the plan-view STM experiments on InAs quantum dots discussed in Chapter 4 were carried out using a Park Scientific Instruments Autoprobe VP2 STM. The plan-view STM experiments on the $Sb_2Te_3$ nanowires and BiSbTe alloys were carried out in both the Park STM and an Oxford Instruments Omicron VT-STM. A comprehensive review of the Park STM system used in these investigations has been discussed Section 2.3 of the Ph.D. theses of Dr. B. Lita and Dr. V. Dasika, and some details are repeated here for completeness.[3,4] Furthermore, a description of the Omicron VT-STM system can be found in Section 6.2.3 of Dr. V. Dasika's Ph.D. thesis, and a comparison of the Omicron and Park systems will be presented here.

### 2.3.1 Cross-sectional and plan-view STM

Figure 2.1 illustrates the orientation of the sample and tip for plan-view and cross-sectional STM on a III-V heterostructure sample. For plan-view STM, the growth surface ([001] for III-V samples) is imaged directly with constant-current STM. For cross-sectional STM (XSTM), a cross-section of the sample under investigation is prepared by cleaving it in ultra-high vacuum (UHV), to expose an atomically flat [110] surface, as illustrated in Fig. 2.1. In constant-current STM, a feedback loop is activated to move the tip towards or away from the surface to maintain a constant tunneling current, typically 100-300 pA. For plan-view STM of topographic features such as uncapped quantum dots, the height of the tip corresponds to the feature height. However, for XSTM, with the achievement of a nearly atomically flat surface, the tunneling current is proportional to the LDOS at the applied potential.

All the STM and STS experiments described in this dissertation were performed with commercially available Pt/Ir or W STM tips from Bruker.[5,6] The STM tips were cleaned *in situ* by electron bombardment from a heated molybdenum filament.[3,7] The tip cleaning procedure for the Park STM is described in detail in Section 2.3.4 of Dr. V. Dasika's thesis, and a slightly modified procedure for the VT-STM is described in Section 2.6.4 of Dr. A.S. Chang's thesis.[4,8] Additionally, XSTM requires special sample preparation. The samples are lapped to a thickness of ~150-200 μm and scribed along a cleavage plane. Further details of the sample preparation for the XSTM GaAs p-n samples will be presented in Section 3.3.

The samples are then mounted into either a plan-view or cross-sectional sample holder and transferred to the UHV STM chamber via a load lock. The ion gauge is switched off ~12 hours before an experiment begins to reduce thermal drift of the tip. For XSTM, on the day of the experiment, the samples are cleaved *in-situ* to reveal a nearly atomically-flat surface. The sample surface is examined using a CSB-175 CCD camera with a 10x Comstar lens (Park STM system) or a telescope with a magnification of 40x (Omicron STM system), and the tip is auto-approached to the sample.

### 2.3.2 Park Autoprobe VP2 and Omicron VT-STM

There are several key differences between the Park Autoprobe VP2 STM and the Omicron VT-STM, including the sample-tip orientation, sample and tip holder designs, vibration isolation, and electronic configuration.

In the Park, the tip and sample are oriented horizontally with respect to the ground, while the VT-STM configures the tip and sample vertically, as illustrated in Fig. 2.2. The Omicron configuration is shown in Fig. 2.2(a), with the tip facing up towards the sample, and the Park configuration, with the tip and sample oriented horizontally, is shown in Fig. 2.2(b). The vertical configuration in the Omicron system is superior for noise reduction because oscillations of the tip induced by gravity are suppressed. Furthermore, the vertical configuration allows easier manipulation of the tip in all spatial directions, while the Park requires a specialized scan head design to enable both +y and –y motion, as described in Section 2.3.2 of Dr. B. Lita's Ph.D. thesis.[3]

Second, the tip holder design for the Park and Omicron differ significantly. The Park tip holder, shown in Fig 2.3(a), is designed to enable both STM and atomic force microscopy (AFM). The STM tip is installed using a single screw to hold the tip in place, while specialized Si piezo-cantilevers for AFM are held in place by a metal clip. The tip holder is secured to the scan head via magnets, and metal contacts on the back of the holder enable the electrical connection for the measurement of the tunneling current for STM or force for AFM. The Omicron tip holders, shown in Fig. 2.3(b) are much simpler in design. The STM tip is placed in the gold metal cylinder and secured by crimping. The tip holder is then magnetically secured to a tip transfer plate for transfer into the UHV chamber and for loading and unloading the tip from the scan head. The Park STM tip holders have the advantage of re-usability, but their complicated structure increases their failure rate over time, while the most common problem with the Omicron STM tip holders is misalignment in the tip transfer plate which prevents proper securement to the scan head, rendering the tip unusable. However, the Omicron STM is able to hold twelve tips *in-situ*, while the Park can accommodate only four.

The vibration isolation method also differs significantly between the Park STM and the VT-STM. The Park STM employs a dual-stage spring suspension system, with metal springs fastened to the stage with Viton rings, while the Omicron VT-STM employs a spring suspension system in conjunction with eddy current magnetic damping, providing superior vibration isolation. However, both systems are still susceptible to vibrations at low frequencies on the order of 1 Hz. The Park STM is mounted on an external air table to provide additional isolation, but the VT-STM has no external isolation.

Finally, there are several key differences between the electronic configurations of the STM systems. First, in the Park, the bias voltage is applied to the sample, and the tip is grounded, while in the Omicron, the reverse is true. Additionally, the VT-STM pre-amplifier, which amplifies the measured tunneling current and converts it to a voltage to be interpreted by the software, has a more sophisticated design which includes a larger gain (so it is more sensitive to pA-range currents) and internal capacitive compensation to reduce parasitic currents that arise during modulation of the voltage during scanning tunneling spectroscopy measurements, which are described in the following section.

### 2.4 Scanning Tunneling Spectroscopy (STS)

For the research presented in this dissertation, STS is used to probe the local band structure. In STS, the bias voltage is varied in a controlled manner, and the resulting tunneling current and differential conductance are measured. The feedback loop is deactivated, and a continuous linear voltage ramp is applied to the sample or the tip. A lock-in amplifier is used to modulate the applied bias and measure the differential conductance, dI/dV, which is proportional to the LDOS and enables determination of the effective band gap. Further details of the principles behind scanning tunneling spectroscopy can be found in Section 2.4.1 of the thesis of Dr. V. Dasika.[4]

A modulation voltage with frequency of 900-1000 Hz and amplitude of 30-100 mV was typically used in these experiments. The Park often required a larger modulation voltage than the Omicron due to the differences in vibration isolation and pre-amplifier sensitivity. The same SR580 lock-in amplifier was used for both the Park and the Omicron

STM. However, there are a few differences in the procedure for STS collection in the Park vs. the Omicron. In the Park STM, STS spectra are collected after an image is completed, while in the Omicron, the raster scanning is paused while collecting an image to take spectra on features of interest. The Park software allows the user to control the bias range, speed of collection, and number of spectra taken at each point. The Matrix software from Omicron also allows the user to specify the number of measurement points collected during a single spectrum.

Previous dissertations from the Goldman group have employed variable-separation STS (VS-STS), in which both the tip height and bias voltage are varied during collection of the spectra.[9,10] VS-STS increases the sensitivity of the measurement near the band edges, but requires a calibrated band gap measurement on a known sample. For the works presented in this thesis, the precise band gap values of the samples were unknown. Thus, constant-separation STS was used, and the band gaps were determined using extrapolation of the linear onsets of the band edges, based on the work by R. Timm et al,[11] as described in detail in Appendix A.

## 2.5 Scanning Thermoelectric Microscopy (SThEM)

In this section, an overview of scanning thermoelectric microscopy (SThEM) is presented. The SThEM experiments on the GaAs p-n junction discussed in Chapter 3 and the plan-view STM experiments on InAs quantum dots discussed in Chapter 4 were carried out using a modified Park Scientific Instruments Autoprobe VP2 STM. The following sections provide an overview of SThEM measurements, followed by a description of the

modification to the Park STM system to enable SThEM and a description of the experimental procedures.

### 2.5.1 Overview

SThEM [12-14] is a technique in which an STM probe tip is used to induce and measure a thermoelectric voltage, generated according to the Seebeck effect

$$V = S\Delta T \qquad (2.1)$$

where V is the thermoelectric voltage, S is the Seebeck coefficient (also known as the thermopower), and ΔT is the induced temperature difference.[15] Figure 2.4 shows an illustration of the Seebeck effect for a sample with conduction dominated by electrons. As a temperature difference is induced, electrons flow according to the energy difference from hot to cold, producing a negative steady state voltage, while hole conduction produces a positive voltage. Thus, S is negative (positive) for n-type (p-type) conduction.

For the experiments described in this thesis, SThEM was performed in UHV, with the substrate side of the sample heated uniformly to a temperature of ~20 K above room temperature.[16] After several hours of heating in UHV, the entire sample is expected to reach an equilibrium temperature.[12] A tungsten tip is prepared in UHV using electron bombardment using the same procedures as for STM measurements. The tip is then used to locally cool the sample and measure the thermoelectric voltage (between the tip and the sample), as shown in Fig. 2.5. For tip-sample temperature differences, ($T_{Sample}$-$T_{Tip}$) < 30 K, S is typically temperature-independent, and $V_{SThEM}$ is proportional to ($T_{Sample}$-$T_{Tip}$).

Thus, the position-dependent thermoelectric voltage, $V_{SThEM}(x)$ is related to S(x) according to

$$V_{SThEM}(\mathrm{x}) = f(\mathrm{x}) \times (T_{Sample} - T_{Tip}) \times S(\mathrm{x}) \qquad (2.2)$$

where $T_{Tip}$ and $T_{Sample}$ are the temperatures of the room-temperature tip and the heated sample, S(x) is the Seebeck coefficient profile, and f(x) is the position-dependence of the fraction of the temperature drop which contributes to the thermoelectric voltage in the sample. The f-factor is described in Appendix B, which includes the details of a Fourier law model which predicts f as a function of tip geometry and thermal conductivity. The materials parameters for this calculation, including the thermal conductivity values, can be found in Appendix C. Because the STM tip is nearly atomically sharp, the point of contact between the tip and sample is sufficiently small that the resulting thermoelectric voltage allows nanoscale-resolved measurements of S.[12,14,17]

### 2.5.2 SThEM Instrumentation

To modify an STM to enable SThEM measurements, several alterations are required, which will be described in detail here. First, it is necessary to install a switch between the tip and the pre-amplifier to be able to disconnect the tunneling current and measure the thermoelectric voltage. We decided to modify the Park Autoprobe VP2 STM rather than the Omicron VT-STM to enable SThEM for because the VT-STM pre-amplifier is split into two stages. The first stage, the I-V converter, is located inside the UHV chamber, while the second stage, the amplifier, is external to the chamber. In contrast, the entire pre-amplifier in the Park system is external. Thus, the VT-STM would require more

significant modifications both inside and outside the chamber than the Park STM, and the insertion of a switch between the STM tip and first stage of the pre-amplifier would have permanently increased the noise floor of the Omicron STM.

Next, a heater and thermometer on the sample plate were installed. We designed a modified sample plate and sample plate holder, shown in Fig. 2.6(a) and (b). In Fig. 2.6(a), the back side of the SThEM sample plate is shown. The heater, shown in red, is home-made and composed of nickel wire wound around an aluminum post, with a resistance of ~80 **Ω**. It is fastened into an inset in the sample plate using Epo-Tek H77 epoxy which is thermally but not electrically conductive. The temperature diode is a Lakeshore Si diode, also fastened to the sample plate using the Epo-Tek epoxy. The electrical connections for the heater and Si diode are made using Pogo pins, mounted on the back of the sample. Figure 2.6(b) shows the sample plate holder, where the Pogo pins make electrical contact with the receptor pins. The sample plate is held in place with clips, and a notch at the top of the sample plate holder assures firm contact between the Pogo pins and receptors.

Finally, we designed and built a break out box to enable switching between tunneling current and thermoelectric voltage measurements. This requires two electrical relays to disconnect both the tunneling current and applied bias and switch to measuring the voltage between those two points. The details of this modification, including diagrams for the modified electrical connections, are explained in detail in Appendix D. Furthermore, after the collection of all the SThEM data presented in this thesis, the Park Autoprobe VP2 controller failed and was replaced with a RHK SPM100 STM controller. Appendix E describes the modifications necessary for this change in detail.

### 2.5.3 Experimental procedure

Once the sample plate is mounted into the holder in the UHV STM chamber, the heater is turned on by supplying a voltage and current from an HP 6614C power supply. The heater should be left on for at least 12 hours before an experiment begins to allow the temperature to stabilize. STM scanning is then used to find the feature(s) of interest. After the STM image is collected, the tip is brought close to the sample at the point of interest by approaching the sample using a high tunneling current (~ 1 nA). Then, the feedback loop is interrupted, and the SThEM relay is switched on to disconnect the bias voltage and tunneling current to measure the thermoelectric voltage and tip-sample resistance using a Keithley 2000 multimeter. Using the fine tip motion of the z-piezo extension, the tip is pressed further into the sample until solid electrical and thermal contact are established. Figure 2.7(a) shows the tip-sample resistance as a function of tip extension for a GaAs sample with Seebeck coefficient, S = 392 μV/K. After the tip is extended less than 100 nm, the electrical resistance has fallen into the kΩ range, indicating good electrical contact. To determine the tip extension needed for good thermal contact, the tip is extended further until $V_{SThEM}$ reaches the value expected based on the known S, for a total tip extension of ~ 400 nm as shown in Fig. 2.7(b). The tip extension does not necessarily reflect the actual distance the tip moves. For example, the tip is not digging hundreds of nm below the surface of the sample; this number more accurately represents the force applied by the piezo as the tip is pressed firmly into the sample.

Once solid thermal and electrical contact has been established, both the resistance and voltage at that point are recorded using a Keithley 2000 multimeter and LabView data

acquisition program developed by Dr. Yen-Hsiang Lin and presented in detail in Appendix F. The tip is then moved several nm across the surface to the next point of the nanostructure of interest. After pausing for 1-3 minutes to let the tip settle, the voltage and resistance data is acquired again. If the resistance value has increased indicating a loss of good electrical contact, the tip is pressed further into the sample until contact is re-established. An investigation of the influence of geometry on SThEM measurements is presented in Appendix G. If the tip is moved back and forth across the nanostructure to acquire multiple measurements, the apparent horizontal position of the tip needs to be corrected for piezo hysteresis (i.e. the nonlinear nature of piezo creep). For the Park Autoprobe VP, the difference in apparent position when moving the tip in –x vs +x was typically ~20 nm.

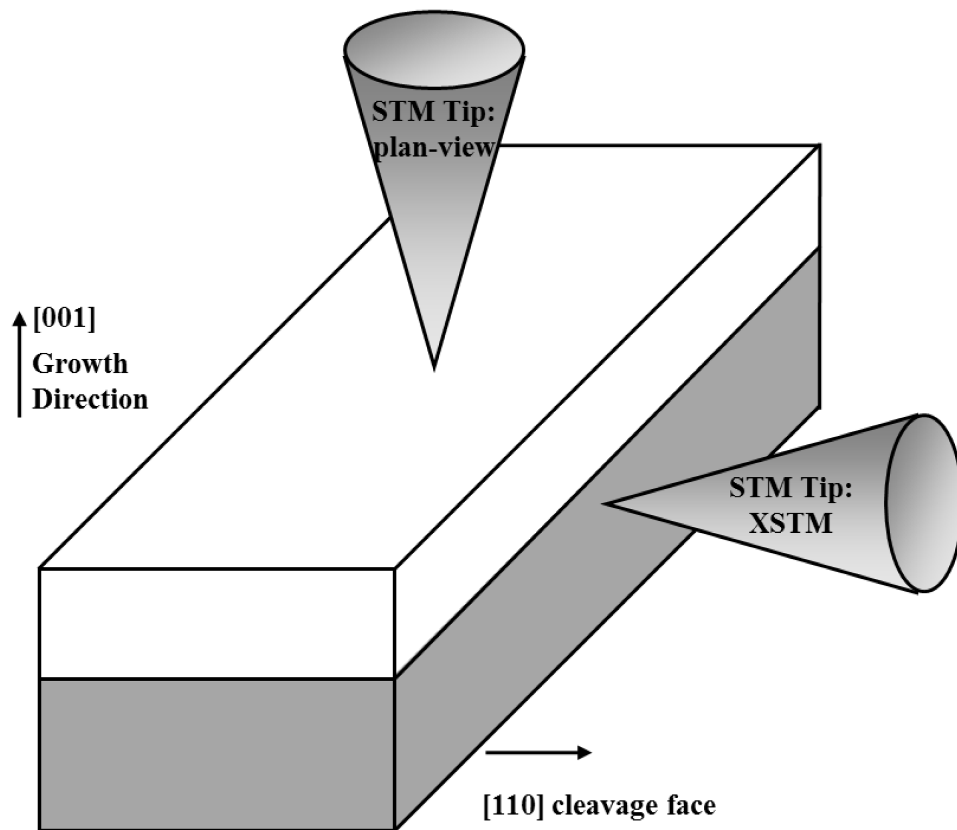


Figure 2.1: Schematic of plan-view and cross-sectional STM applied to a III-V heterostructure. The STM tip is brought within a few angstroms of the growth [001] (plan-view) or cleaved [110] (cross-sectional) face.

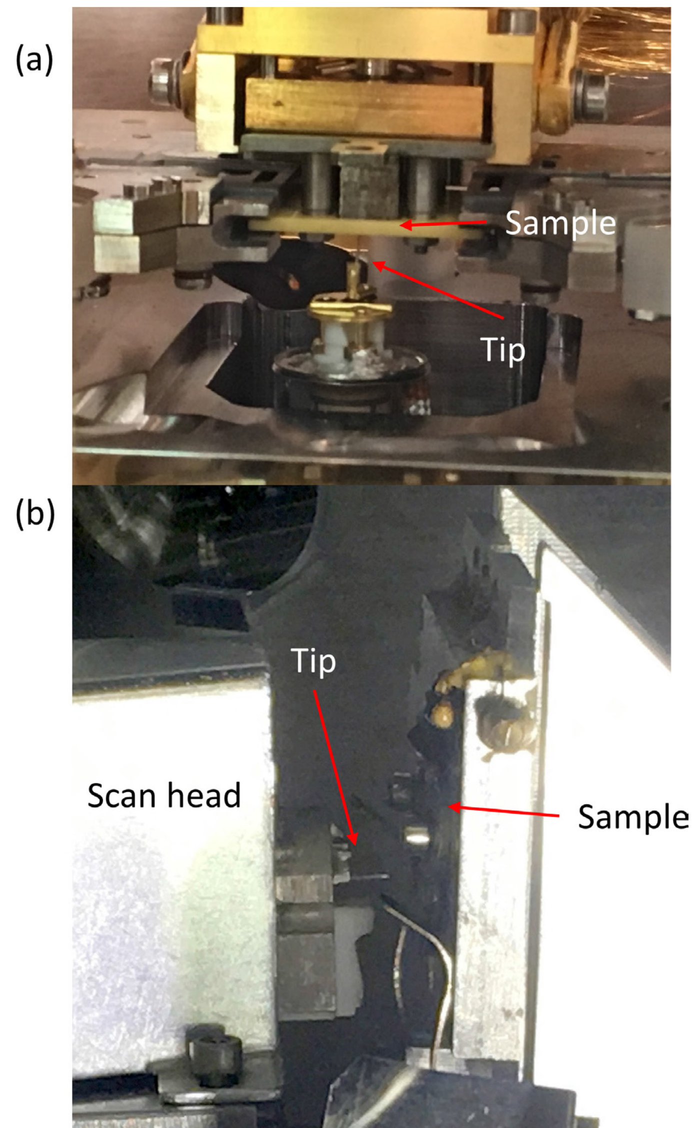


Figure 2.2: Tip and sample configurations in the (a) Omicron VT-STM and (b) Park Autoprobe VP2. The Omicron has a vertical configuration where the tip is facing up towards the sample, and the Park has a horizontal configuration, with the tip and sample oriented parallel to the floor.

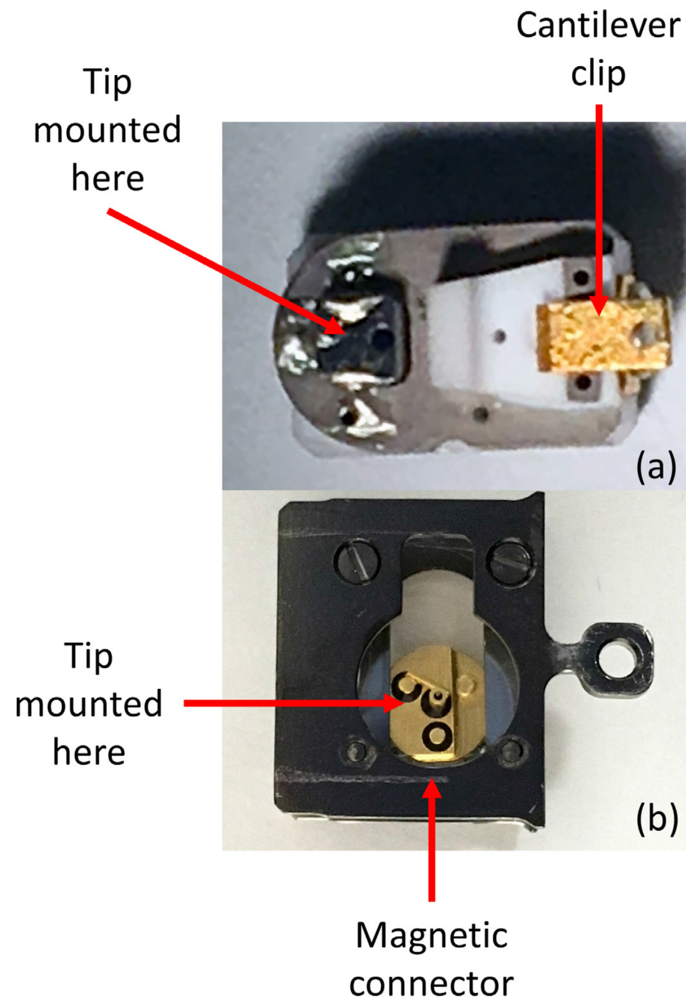


Figure 2.3: (a) Park STM tip holder, designed to enable both STM and AFM. The STM tip is secured using a single screw, while specialized Si piezo-cantilevers for AFM are held in place by a metal clip, both marked by red arrows. (b) The Omicron tip holder and tip transfer plate. The STM tip is placed in the gold metal cylinder and secured by crimping. The tip holder is then magnetically secured to a tip transfer plate for transfer into the UHV chamber and for loading and unloading the tip from the scan head. The tip position and magnetic connector are marked by red arrows.

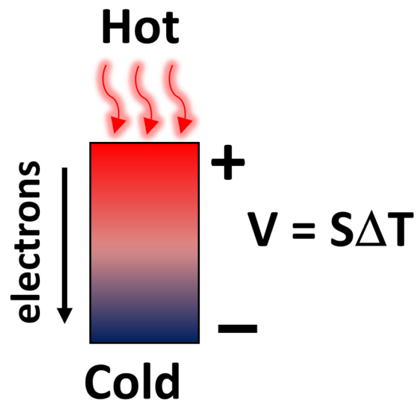


Figure 2.4: Simple demonstration of the Seebeck effect for electron-dominated conduction. The electrons respond to the applied temperature gradient and develop a steady-state voltage proportional to the applied temperature difference and the Seebeck coefficient of the material.

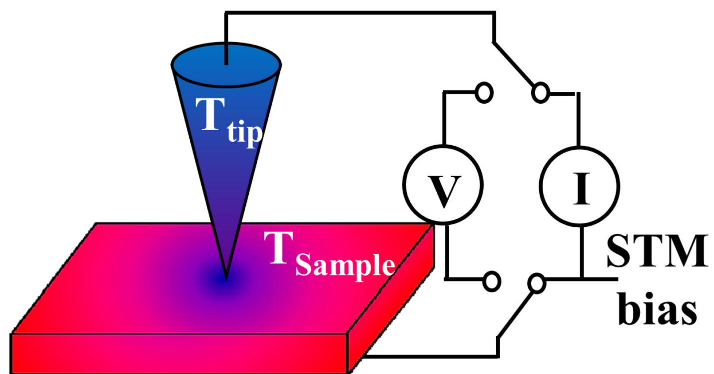


Figure 2.5: Schematic of SThEM setup: A room-temperature STM tip is brought into contact with a heated sample, generating a local thermoelectric voltage. Relays allow switching between measuring the thermoelectric voltage and the STM tunneling current.

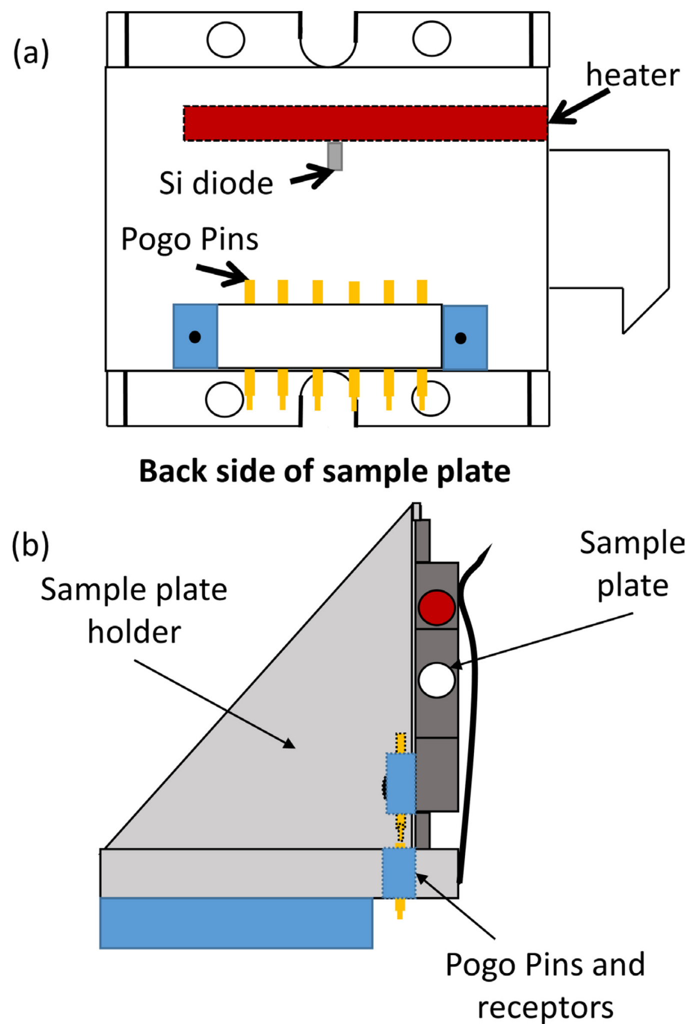


Figure 2.6: (a) Back side of the SThEM sample plate and (b) side-view of the sample plate holder. In (a), the positions of the heater (red) and Si diode (grey) are shown. The electrical connections for the heater and Si diode are made using Pogo pins, mounted on the back of the sample. (b) The sample plate holder, where the Pogo pins make electrical contact with the receptor pins. The sample plate is held in place with clips, and a notch at the top of the sample plate holder assures firm contact between the Pogo pins and receptors.

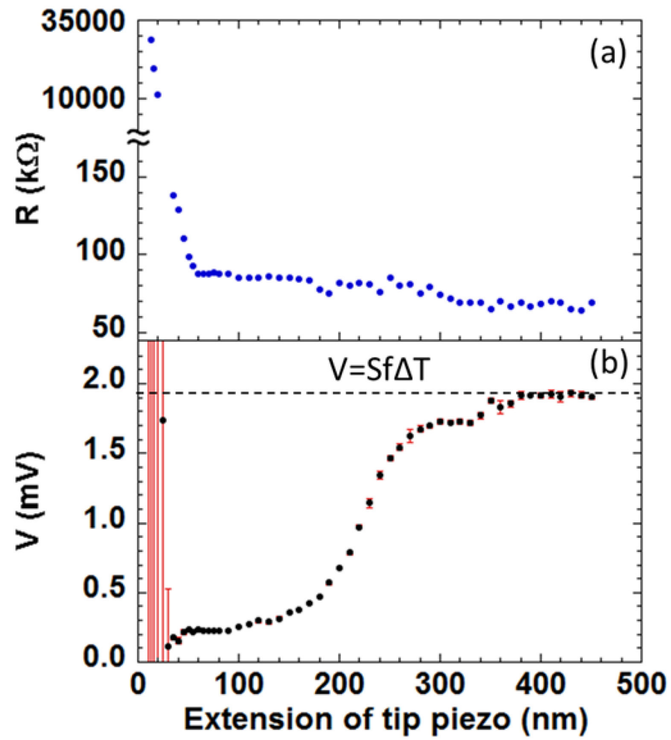


Figure 2.7: (a) The tip-sample resistance and (b) thermoelectric voltage measured between the tip and sample as a function of tip extension for a GaAs sample with Seebeck coefficient, S = 392 μV/K. Using the fine tip motion of the z-piezo extension, the tip is pressed further and further into the sample until solid electrical and thermal contact are established. In (a), after the tip is extended less than 100 nm, the electrical resistance has fallen into the kΩ range, indicating good electrical contact. (b) To determine the tip extension needed for good thermal contact, the tip is extended further until $V_{SThEM}$ reaches the value expected based on the known S, for a total tip extension of ~ 400 nm.

### 2.6 References

[1] A. Y. Cho and S. E. Stokowsk, *Solid State Commun.* **9**, 565 (1971).

[2] M. A. Herman, W. Richter, and H. Sitter, *Epitaxy Physical Principles and Technical Implementation*. (Springer, 2004).

[3] B. Lita, Ph.D. Thesis, University of Michigan, 2001.

[4] V. Dasika, Ph.D. Thesis, University of Michigan, 2010.

[5] Bruker Model TT10 Etched Tungsten STM Probes S/N: 120613

[6] Bruker Model PT10 Cut Platinum/Iridium STM Probes S/N: 101713

[7] R. M. Feenstra, *Phys. Rev. B* **50**, 4561 (1994).

[8] A.S. Chang, Ph.D. Thesis, University of Michigan, 2016.

[9] V. Dasika, Ph.D. Thesis, University of Michigan, 2010.

[10] A.S. Chang, Ph.D. Thesis, University of Michigan, 2016.

[11] R. Timm, H. Eisle, A. Lenz, L. Ivanova, V. Vosseburger, T. Warming, D. Bimberg, I. Farrer, D.A. Ritchie, and M. Dahne, *Nano Lett.* **10**, 2972 (2010).

[12] J. C. Walrath, Y. H. Lin, K. P. Pipe, and R. S. Goldman, *Appl. Phys. Lett.* **103**, 212101 (2013).

[13] H.K. Lyeo, Ph.D. Thesis, University of Texas at Austin, 2003.

[14] H.K. Lyeo, A. A. Khajetoorians, L.Shi, K.P. Pipe, R.J. Ram, A.Shakouri, C. K. Shih, *Science*, **303**, 816 (2004).

[15] H. J. Goldsmid, *Thermoelectric Refrigeration*, Plenum Press, New York, 1964.

[16] To minimize thermal drift, $\Delta T$ is typically limited to values $\leq 30$ K.

[17] Z. Bian, A. Shakouri, L. Shi, H.K. Lyeo and C.K. Shih, *Appl. Phys. Lett.* **87**, 053115 (2005).

# Chapter 3

# Quantifying the local Seebeck coefficient with SThEM

## 3.1 Overview

In this chapter a method is presented for quantifying the local Seebeck coefficient with SThEM, using a direct approach to convert the thermoelectric voltage to a local S profile. Using XSTM and SThEM, the thermoelectric voltage is profiled across a GaAs p-n junction. We then use a quasi-3D conversion matrix that considers both the sample geometry and the temperature profile to convert the thermoelectric voltage to a nanometer resolution profile of S. For a GaAs p-n junction, the resulting S-profile is consistent with that computed using the free carrier concentration profile. Although deconvolutions based on tip geometries are often used to enhance lateral resolution of scanning probe measurements, this is the first deconvolution which allows direct conversion of a measured proxy quantity to the quantity of interest. Therefore, this approach could be extended to other techniques such as scanning voltage microscopy and scanning spreading resistance microscopy.

The STM and SThEM data were collected by the author and Dr. Y.H. Lin, who jointly developed the quasi-3D deconvolution method. The GaAs p-n junction was grown in the Goldman MBE lab at the University of Michigan by Dr. R. L. Field III. This work was supported by the Department of Energy under Award Number DE-PI0000012 and the

National Science Foundation Graduate Student Research Fellowship under Grant No. DGE 1256260. Y.H.L. and R.S.G. were also supported in part by the U.S. DOE, Office of Basic Energy Sciences under contract DE-FG02-06ER46339. This work was published in *Applied Physics Letters.*[1]

### 3.2 Background

Nanostructured materials have been identified as promising candidates for high figure-of-merit thermoelectrics.[2,3] For example, enhancements of S, apparently due to low dimensionality, have been reported for embedded Bi nanowires and $Bi_2Te_3/Sb_2Te_3$ superlattices, in comparison to their bulk counterparts.[4,5] To directly examine the mechanisms for nanostructure-induced S enhancement, a quantitative measurement of S on a nanometer scale is needed. Recently, a modified scanning probe microscope has been used to measure the thermoelectric voltage induced by contact between a room-temperature tip and a heated sample, according to $V=S\Delta T$. Scanning of the probe tip enables nanometer-scale spatially resolved measurements of the thermoelectric voltage. It is generally assumed that $\Delta T$ occurs at an infinitely small tip-sample contact.[6,7] However, since temperature is only physically meaningful within a region larger than the phonon mean free path $\Lambda$, $\Delta T$, and therefore S, cannot be well defined on a scale smaller than $\Lambda$.[8] Bian et al.[9] instead assumed a constant sample temperature within one $\Lambda$ of the tip-sample contact point. The sample was then modeled as a 3D network of resistors and voltage sources, with the solutions to Kirchhoff's laws at each tip-sample contact point providing the predicted thermoelectric voltage profile, V(x). The goal of the work presented here is

to demonstrate a direct conversion of V(x) to a Seebeck coefficient profile, S(x). In the rest of this chapter, we report the results of a quasi-3D conversion matrix which considers both the sample geometry and the temperature profile, applied to a SThEM measurement across a GaAs p-n junction.

### 3.3 MBE growth and sample preparation

The GaAs p-n junction consists of a 1 μm thick layer of Si-doped GaAs grown at 580 °C on epiready Zn-doped GaAs (001) substrates by molecular beam epitaxy (MBE), using solid Ga and $As_2$ sources, by Dr. R. L. Field III in the Goldman MBE lab at the University of Michigan. The surface reconstruction was monitored *in situ* with an 18 keV reflection high-energy electron diffraction (RHEED) source. The targeted free carrier concentration of the Si-doped layer is n = $8x10^{16}$ $cm^{-3}$, and the Zn-doped GaAs substrate has a measured carrier concentration of p = 1.3 x $10^{19}$ $cm^{-3}$.

To prepare the sample for XSTM, the same sample preparation procedures were used as have been reported in the theses of previous group members.[10-13] Following growth, the sample was removed from the chamber and cleaved along the $(110)$ and $(\bar{1}10)$ directions using a diamond scriber and glass slides, such that each piece had dimensions of ~ 15 mm x 2 mm, where the long edge of the sample was cut along the $(\bar{1}10)$ direction. The samples were then thinned to approximately 200 μm by mechanical polishing from the substrate side.

Following polishing, a shallow scratch, called a scribe mark, was made by hand with a diamond scriber along the $(\bar{1}10)$ direction. The samples were mounted in an XSTM

holder such that the scribe mark is parallel to the edge of the jaw, with the epilayer side facing up, as shown in the schematic photos in Section 6.2.3 of the Ph.D. thesis of Dr. V. Dasika.[12] The sample was then loaded into the load lock of the Park STM system and pumped down with a turbo pump for subsequent transfer into the UHV STM chamber.

Once the sample plate was mounted in the holder described in Section 2.5.2, the SThEM heater was switched on, and the ion gauge was switched off. The experiment proceeded 12 hours later when the temperature of the sample had stabilized at ~20 K above room temperature. The sample was then cleaved in UHV (base pressure < $6 \times 10^{-11}$ Torr) by lowering a 60° diamond tip attached to an XYZ manipulator.[13] When the cleaver makes contact with the end of the cantilever sample, the sample breaks along the scribe mark, often resulting in a nearly atomically-flat surface.[11,12] The tip was then auto-approached to a region of the sample far from the scribe mark. The orientation of the tip and sample is shown in Fig. 3.1(a), where the tip is approached to the cleaved $(\bar{1}10)$ face.

### 3.4 XSTM of GaAs p-n junction

For most XSTM experiments in the Goldman group, a walk-off procedure is performed to find the edge of the epilayer and to search for a marker layer which signals the beginning of the layers of interest, as described in the theses of Drs. B. Lita and A.S. Chang.[11,13] However, this GaAs p-n junction did not have a marker layer, so we were not able to locate the p-n junction using a traditional walk-off procedure. Instead, we used SThEM to determine whether $V_{SThEM}$ at the position of the tip approach was positive, indicating the p-type conduction of the substrate, or negative, indicating the n-type

conduction of the growth layer. If $V_{SThEM}$ was positive, the tip was retracted from the surface and moved up toward the growth edge by ~ 1-3 μm. The tip was approached again, and $V_{SThEM}$ was noted to be positive or negative. This procedure was repeated until $V_{SThEM}$ was measured to be negative. Then, the tip was retracted away from the surface once more and moved down ~ 1 μm. Subsequent STM scans located the p-n junction, shown in Fig 3.1(b).

### 3.5 SThEM of GaAs p-n junction

Following collection of the STM image, the STM was switched into SThEM mode. Figure 3.1(a) shows the SThEM probe tip trajectory (white dotted line) across the p-n interface (black dashed line), and the thermoelectric voltage at each tip-sample contact point, $V_i$, is measured. To determine the f-factor, we measured the $V_{SThEM}$ of a p-type GaAs substrate with known S, resulting in f=0.2, consistent with the value predicted assuming negligible tip-sample contact resistance using the equations presented in Appendix B.

For comparison, we compute the Seebeck coefficient profile, $S_{comp}(x)$, using the targeted position-dependence of the free carrier concentration as input into the Boltzmann transport equations within the relaxation time approximation.[9] Assuming full activation of $Zn_{Ga}$ and $Si_{Ga}$, the targeted dopant profiles correspond to the dashed lines in Fig. 3.1(c). Using averaged literature values for Si and Zn diffusivities in GaAs,[14-17] the dopant redistribution during GaAs growth at 580°C is expected to lead to the solid line profile shown in Fig. 3.1(c), with the effective p-n junction defined as x=0. For this diffused dopant

profile, solutions to the 1D Poisson equation[18] result in the position-dependence of free electron (black) and free hole (blue) concentrations shown in Fig. 3.2(a), revealing a depletion width of approximately 200 nm. The details of the 1D Poisson calculation can be found in Appendix H, and the materials parameters used are presented in Appendix C.

### 3.6 Quasi-3D deconvolution

To convert V(x) to a Seebeck coefficient, S(x), we define an N-dimensional array, $\{V_i\}$, which is related to an array of Seebeck coefficients, $\{S_j\}$, as follows:

$$V_i \equiv \sum_{j=1}^{N} \Delta T_{ij} S_j \qquad (3.1)$$

For both the $\{V_i\}$ and $\{S_j\}$ arrays, the grid size is greater than or equal to Λ. We note that the matrix $\Delta T_{ij}$ captures the both the geometry of the sample and the T-profile, T(r). We assume that the temperature within one Λ of the tip-sample contact point is fixed at $T_{Contact}$, with heat conduction governed by Fourier's Law, where the thermal conductivity, κ, of the sample is constant. The radial dependence of the T profile becomes:

$$T(r) = \begin{cases} T_{Contact} + (T_{Sample} - T_{Contact})(\frac{r-\Lambda}{r}), r > \Lambda \\ T_{Contact}, r < \Lambda \end{cases} \qquad (3.2)$$

where r = 0 is the center of the tip-sample contact point. For our GaAs p-n junction, Λ = 6nm.[9] For other heterostructures, it may be necessary to vary the grid size depending on the local mean free path.[19]

To implement Eq. 3.1, we assume that $V_i$ contains contributions from 3 directions parallel and 2 directions perpendicular to the p-n junction interface, a "quasi-3D" matrix

conversion approach, shown in Fig. 3.3. We further assume that the conductance $G_i$ is position-independent, such that

$$V_i = \frac{\sum_j V_j}{5} \tag{3.4}$$

where $V_j$ are the voltages along all 5 directions shown in Fig. 3.3. For the 3 directions parallel to the p-n junction interface, $S_j$ is position-independent. Thus, the diagonal terms of $\Delta T_{ij}$ become

$$\Delta T_{i=j} \equiv \frac{3}{5}\left(T_{Sample} - T_{Conctact}\right) \tag{3.5}$$

On the other hand, for the 2 directions perpendicular to the p-n junction interface, $S_j$ is position-dependent; the off-diagonal terms of $\Delta T_{ij}$ become

$$\Delta T_{i\neq j} \equiv \frac{1}{5}\sum_{i\neq j}[T(r_{ij}) - T(r_{ij\pm 1})] \tag{3.6}$$

where $r_{ij}$ is the distance between the location j and the tip-sample contact point, i. Finally, to directly convert $V_i$ to $S_j$ using the quasi-3D matrix approach, we define the following inverse matrix, $\Delta T_{ij}^{-1}$:

$$S_j = \sum_i \Delta T_{ij}^{-1} V_i \tag{3.7}$$

### 3.7 Measured $V_{SThEM}$ and converted S profiles

Figure 3.2(b) shows the position-dependence of the measured thermoelectric voltage, $V_{SThEM}$, with the junction at x = 0. For comparison, we use $S_{comp}(x)$ to calculate V(x) with the δT(r), 3D network, and quasi-3D conversion methods, also shown in Fig. 3.2(b). The Matlab code used to carry out the quasi-3D calculations, written by the author and Dr. Y.H. Lin, is provided in Appendix I. At the junction, since the thermal voltages due to electrons

and holes cancel each other, $V_{SThEM} = 0$. On the n-side (p-side) of the junction, the transport is dominated by electrons (holes). Moving away from the junction interface, $V_{SThEM}$ becomes increasingly negative (positive), up to a maximum value, beyond which $V_{SThEM}$ decreases asymptotically to values inversely proportional to the carrier concentration. The most significant variations in $V_{SThEM}$ occur within 100 nm of the p-n junction interface, consistent with the estimated depletion width of 200 nm, as discussed above. For comparison, $V_{\delta T(r)}$ represents the thermoelectric voltage assuming the temperature gradient occurs at an infinitely small tip-sample contact, such that $V_{\delta T(r)} = S_{Comp} \times (T_{Sample}-T_{Contact})$. Since $(T_{Sample}-T_{Contact})$ actually occurs in a finite region surrounding the tip-sample contact, $V_{\delta T(r)}$ is much larger than $V_{SThEM}$ in the vicinity of the p-n junction interface, similar to earlier studies.[6,9]

For $V_{3D}$ and $V_{quasi\text{-}3D}$, $T_{Sample}$ is assumed to be constant to within one $\Lambda$ of the tip-sample contact point. $V_{3D}$ is calculated with the 3D network method of Bian et al.,[9] while $V_{quasi\text{-}3D}$ is calculated using Eq. 3.1 with $S_{Comp}$. The values and position-dependences of $V_{3D}$ and $V_{quasi\text{-}3D}$ are similar, except in the immediate vicinity of the p-n junction, where $dV_{quasi\text{-}3D}/dx$ is greater than $dV_{3D}/dx$. The overall agreement between the position-dependences of $V_{quasi\text{-}3D}$ with $V_{3D}$ suggests that the quasi-3D matrix approximation can be used in lieu of the 3D network simulation. On the n-side of the junction, $V_{3D}$ and $V_{quasi\text{-}3D}$ are in good agreement with the measured $V_{SThEM.}$ However, on the p-side, the predicted values $V_{\delta T(r)}$, $V_{3D}$, and $V_{quasi\text{-}3D}$ are all larger than $V_{SThEM}$, suggesting that the p-type carrier concentration has been underestimated. Although the $V_{SThEM}$ error bars on the n-side of the junction in Fig. 3.2(b) are noticeably larger than on the p-side, the value of the error

bars is simply proportional to the value of the thermoelectric voltage. In other words, spatial variation in the signal to noise ratio across the junction is insignificant.

We now convert the measured $V_{SThEM}$ to S using our quasi-3D matrix approach, $S_{quasi-3D}$, the δT(r) approach, $S_{\delta T(r)} = V_{SThEM}/(T_{Sample}-T_{Contact})$, and $S_{Comp}$, as described above. For the inverse quasi-3D matrix approach, we calculate $S_{quasi-3D}$ from $V_{SThEM}$ using $\Delta T_{ij}^{-1}$ in Eq. 3.6. As shown in Fig. 3.4, the spatial profiles of $S_{quasi-3D}$ and $S_{\delta T(r)}$ are similar to those of $V_{SThEM}$ in Fig. 3.2(b). At the junction, since the Seebeck coefficients due to electrons and holes cancel each other, $S_{quasi-3D}$ and $S_{\delta T(r)}$ are zero. On the n-side (p-side) of the junction, the transport is dominated by electrons (holes). Moving away from the junction interface, $S_{quasi-3D}$ and $S_{\delta T(r)}$ become increasingly negative or positive, up to maximum values, beyond which both decrease asymptotically to values inversely proportional to the carrier concentration. The most significant variations in $S_{quasi-3D}$ and $S_{\delta T(r)}$ occur within 100 nm of the p-n junction interface, consistent with the estimated depletion width of 200 nm, as discussed above. Interestingly, the magnitude of $S_{\delta T(r)}$ is generally smaller than $S_{Comp}$, especially in the vicinity of the interface, while $S_{quasi-3D}$ shows better overall agreement with $S_{Comp}$. With more detailed information about the position-dependence of the electrical and thermal conductivity in the vicinity of the p-n junction, the elements $\Delta T_{ij}$ of the quasi-3D conversion matrix may be tuned to provide improved agreement between $S_{quasi-3D}$ and $S_{Comp}$.

### 3.8 Summary and Conclusions

In summary, we demonstrate an approach to quantify the local Seebeck coefficient using SThEM data in conjunction with a quasi-3D conversion matrix to directly convert the measured temperature gradient-induced voltage profile to a Seebeck coefficient profile. For a GaAs p-n junction, we assume that V contains contributions from 3 directions parallel and 2 directions perpendicular to the p-n junction interface, with a position-independent conductance. Using the δT(r) method and quasi-3D method to convert $V_{SThEM}$ to $S_{\delta T(r)}$ and $S_{quasi\text{-}3D}$, we find that $S_{quasi\text{-}3D}$ exhibits better overall agreement with $S_{Comp}$ than $S_{\delta T(r)}$. Since our quasi-3D conversion approach only considers the temperature profile and geometry of the sample, this provides a basic framework for developing a conversion matrix even when details such as the thermal and electrical conductivity profiles of a sample are not well known. Although deconvolutions based on tip geometries are often used to enhance lateral resolution of scanning probe measurements,[20,21,22] this deconvolution allows direct conversion of a measured proxy quantity to the quantity of interest. Therefore, this approach could be extended to other techniques such as scanning voltage microscopy and scanning spreading resistance microscopy.[23]

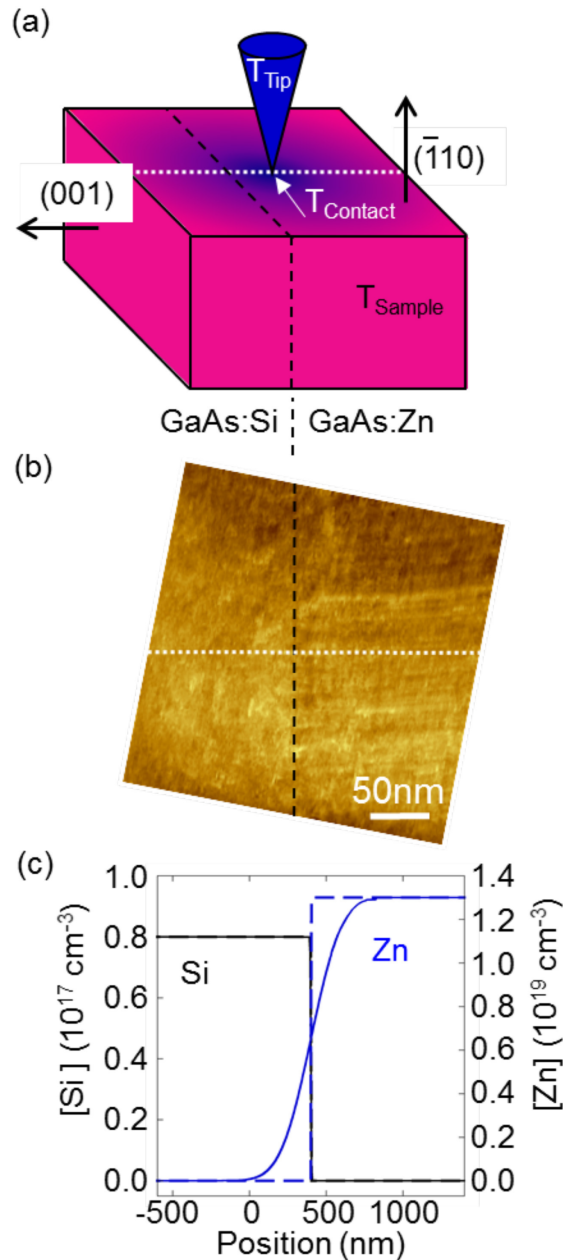


Figure 3.1: (a) Schematic of SThEM setup with room temperature ($T_{Tip}$) probe tip in contact with heated ($T_{Sample}$) sample, consisting of the cleaved ($\bar{1}10$) surface of a GaAs p-n junction. (b) Cross-sectional STM image of a p-n junction, with junction location defined by the black dashed line and SThEM tip trajectory defined by the white dotted line. (c) Dashed lines represent the targeted dopant profiles, assuming full activation of $Zn_{Ga}$ and $Si_{Ga}$; solid lines represent the redistributed dopant profiles following diffusion during GaAs growth at 580°C. Reprinted with permission from Ref. 1 (Copyright 2013, AIP Publishing LLC).

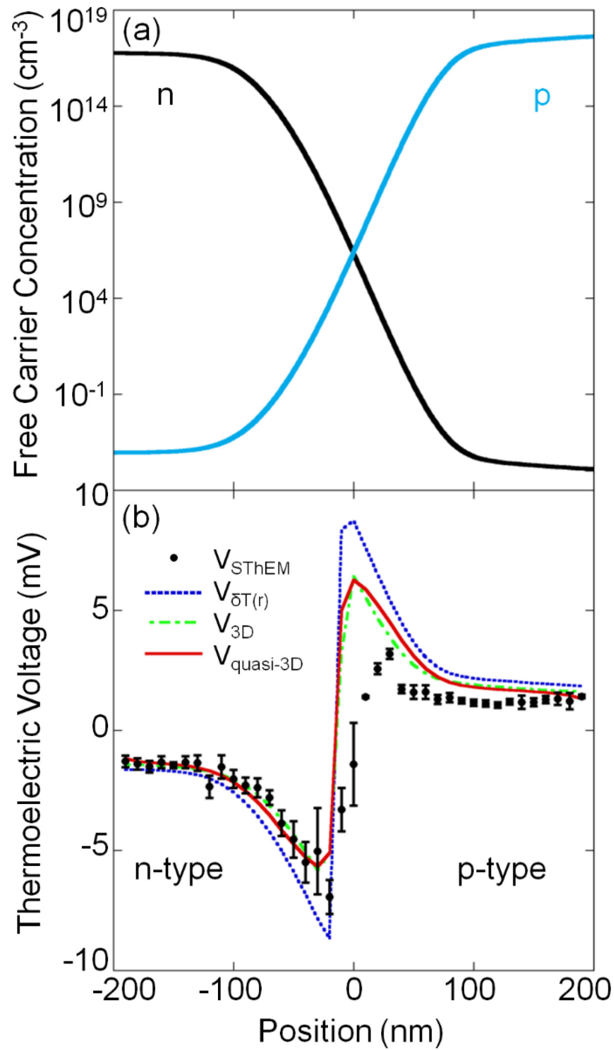


Figure 3.2: (a) Position-dependence of free electron (black) and hole (blue) concentrations calculated using the 1D Poisson equation for the diffused dopant profile in Fig 3.1(c). (b) Position-dependence of the measured thermoelectric voltage, $V_{SThEM}$, with the junction at x = 0. For comparison, the Seebeck coefficient computed using the free carrier concentration profile was used to determine the voltage profiles using the $\delta T(r)$, 3D network, and quasi-3D conversion methods, labeled $V_{\delta T(r)}$, $V_{3D}$, and $V_{quasi\text{-}3D}$ in the plot. The most significant variations in $V_{SThEM}$ occur within 100 nm of the p-n junction interface, consistent with the estimated depletion width of 200 nm. The general agreement between the position-dependences of $V_{quasi\text{-}3D}$ and $V_{3D}$ suggests that the quasi-3D matrix approximation can be used in lieu of the 3D network simulation. Reprinted with permission from Ref. 1 (Copyright 2013, AIP Publishing LLC).

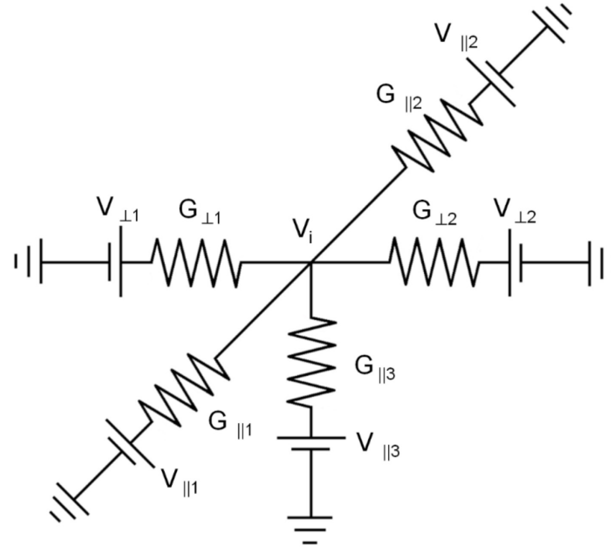


Figure 3.3: Effective circuit diagram of the tip-sample contact point with position-independent conductances, G, and voltage sources connected in three directions perpendicular and two directions parallel to the p-n junction interface. For isotropic G, the voltage, $V_i$, is reduced to the average of V in the five directions. Reprinted with permission from Ref. 1 (Copyright 2013, AIP Publishing LLC).

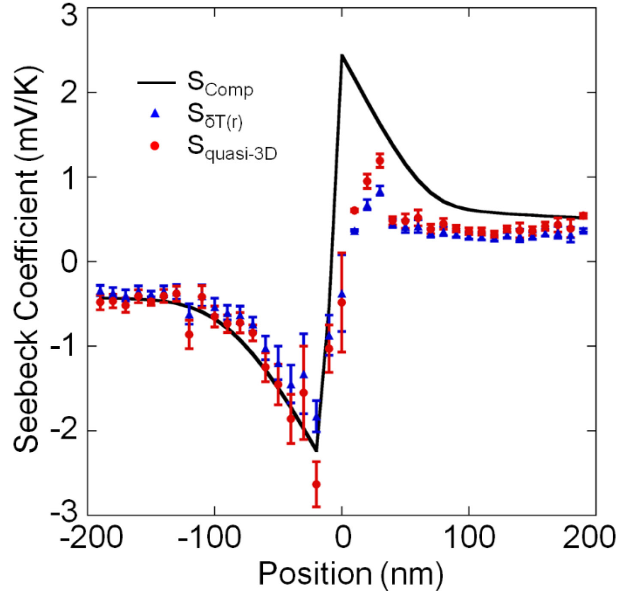


Figure 3.4: Position-dependence of $S_{quasi\text{-}3D}$, $S_{\delta T(r)}$, and $S_{Comp}$. $S_{quasi\text{-}3D}$ is in general agreement with $S_{Comp}$, while the magnitude of $S_{\delta T(r)}$ is generally smaller than $S_{Comp}$, especially in the vicinity of the interface. Reprinted with permission from Ref. 1 (Copyright 2013, AIP Publishing LLC).

## 3.9 References

[1] J. C. Walrath, Y. H. Lin, K. P. Pipe, and R. S. Goldman, *Appl. Phys. Lett.* **103**, 212101 (2013).

[2] L. D. Hicks and M. S. Dresselhaus, *Phys. Rev. B* **47**, 12727 (1993).

[3] L. D. Hicks and M. S. Dresselhaus, *Phys. Rev. B* **47**, 16631 (1993).

[4] J. P. Heremans, C.M Thrush, D.T. Morelli, M.C. Wu, *Phys. Rev. Lett.* **88**, 216801 (2002).

[5] R. Venkatasubramanian, E. Siivola, T. Colpitts, B. O'Quinn, *Nature* **413**, 597 (2001).

[6] H.K. Lyeo, A. A. Khajetoorians, L.Shi, K.P. Pipe, R.J. Ram, A.Shakouri, C. K. Shih, *Science* **303**, 816 (2004).

[7] B. Lee, K. Kim, S. Lee, J.H. Kim, D.S. Lim, O. Kwon, J.S. Lee, *Nano Lett.*, **12**, 4472 (2013).

[8]Similarly, S must be defined in a region larger than the electron/hole relaxation length or the inter-dopant spacing of the material (~5 nm).

[9] Z. Bian, A. Shakouri, L. Shi, H. K. Lyeo and C. K. Shih, *Appl. Phys. Lett.* **87**, 053115 (2005).

[10] J. N. Gleason, Master's Thesis, University of Michigan, 2006.

[11] B. Lita, Ph.D. Thesis, University of Michigan, 2001.

[12] V. Dasika, Ph.D. Thesis, University of Michigan, 2010.

[13] A. S. Chang, Ph.D. Thesis, University of Michigan, 2016.

[14] E. F.Schubert, J. B.Stark, T. H.Chiu, B. Tell, *Appl. Phys. Lett.* **53**, 293 (1988).

[15] T. Y. Tan, U. Gösele, *Mater. Sci. Eng. B*. **1**, 47 (1988).

[16] N. H. Ky, L. Pavesi, D. Araujo, J. D. Ganière, F. K. Reinhart, *J. Appl. Phys.* **69**, 7585 (1991).

[17] V. Quintana, J. J. Clemencon, A. K. Chin, *J. App. Phys.* **63**, 2454 (1990).

[18] I. H. Tan, G. L. Snider, L. D. Chang, and E. L. Hu, *J. Appl. Phys.* **68**, 4071(1990).

[19] A. J. Minnich, J. A. Johnson, A. J. Schmidt, K. Esfarjani, M. S. Dresselhaus, K. A. Nelson, G. Chen, *Phys. Rev. Lett.*, **107**, 095901 (2011).

[20] D. Keller, *Surf. Sci*., **253**, 353 (1991).

[21] P. Markiewicz and M. C. Goh, *Langmuir*, **10**, 5 (1994).

[22] T. Machleidt, E. Sparrer, D. Kapusi, and K-H Franke, *Meas. Sci. Technol.*, **20**, 084017 (2009).

[23] S. B. Kuntze, D. Ban, E. H. Sargent, St. J. Dixon-Warren, J. K. White & K. Hinzer, Crit. Rev. *Solid State Mater. Sci.*, **30**, 71 (2005).

# Chapter 4

## Profiling the local carrier concentration across a semiconductor quantum dot

### 4.1 Overview

This chapter presents a profile of the local carrier concentration, n, across epitaxial InAs/GaAs QDs consisting of 3D islands on top of a 2D alloy layer. We use STM to locate an isolated QD and SThEM to profile the local thermoelectric voltage and Seebeck coefficient. The S profile is then converted to a conduction band-edge profile and compared with Poisson-Schrodinger band-edge simulations. The combined computational-experimental approach suggests a reduced carrier concentration in the QD center in comparison to that of the 2D alloy layer. The relative roles of free carrier trapping and/or dopant expulsion are discussed. We further use 3D atom probe tomography to profile the distribution of Si dopants. Preliminary data indicates a higher Si dopant concentration within the QDs than in the surrounding WL, with an increase in the number of dopants in the vicinity of the QD with growth layer. This work is the first measurement of a carrier concentration across a single quantum dot, and this approach can be applied to a wide range of semiconductor heterostructures, providing key insight necessary for achieving nanostructured semiconductor device design goals.

The STM and SThEM data were collected by the author and Dr. Y.H. Lin. The InAs QD sample for SThEM was grown in the Goldman MBE lab at the University of Michigan by Dr. S. Huang, who also collected the AFM image of the QD topography. The multi-layer InAs QD sample for APT was grown in the Goldman MBE lab at the University of Michigan by Mr. D. Del Gaudio and Mr. T. Jen. APT data was collected by the author and Dr. A.S. Chang using a CAMECA LEAP 4000X Si system in the Michigan Center for Materials Characterization. This material is based upon work supported by the Department of Energy (DoE) under Award Number DE-PI0000012 and the National Science Foundation Graduate Student Research Fellowship under Grant No. DGE 1256260. Y.H.L. and R.S.G. were also supported in part by the U.S. DoE, Office of Science, Office of Basic Energy Sciences under contract DE-FG02-06ER46339. SH was supported by the Center for Solar and Thermal Energy Conversion, an Energy Frontier Research Center funded by the U.S. DoE, Office of Science, Office of Basic Energy Sciences under Award No. DE-SC0000957. Parts of this work have been published in *Applied Physics Letters*.[1]

### 4.2 Background

Self-assembled semiconductor QDs are promising materials for a variety of solid-state applications, including solar cells,[2,3] lasers,[4] photodetectors,[5,6] light-emitting diodes,[7,8] and thermoelectric generators.[9] Due to the practical and fundamental limitations of existing local probe techniques, [10] understanding and manipulating the local electronic properties of QDs, such as the carrier concentration (n), remains challenging. Using C-V measurements of capped InAs QD layers, several groups have reported carrier depletion in

the vicinity of the QD layers.[11-13] Since the carrier depletion occurs primarily for InAs coverage beyond 3 monolayers (ML), it is often attributed to strain relaxation-induced defects which act as carrier traps.[14,15] However, for C-V and scanning capacitance microscopy, n is spatially averaged over 100's of $nm^2$ and $\mu m^2$, i.e. 10 to 100,000 QDs. Thus, carrier concentration profiling across a single QD and the surrounding 2D alloy layer, often termed the "wetting layer" (WL), has not been reported. SThEM provides nanoscale spatially-resolved quantitative measurements of S, which are then converted to a local n profile as described by Lyeo et al.[16] Here, we report a nanometer-resolution profile of S and n across a uniformly- and degenerately-doped, uncapped 3ML InAs/GaAs QD. We compare the corresponding conduction band-edge profile with Poisson-Schrodinger (PS) band-edge simulations, assuming a profile of In fraction, $x_{In}$, for an elastically relaxed QD. We further use 3D atom probe tomography to profile the distribution of Si dopants. The correlation between the Si dopant distribution and the observed carrier concentration profile is discussed.

### 4.3 MBE growth of InAs quantum dots

Two InAs QD samples were grown with MBE: a single layer, uncapped sample for STM and SThEM, and a multi-layer, capped sample for atom probe tomography (APT). For both samples, the InAs QDs were grown on epiready GaAs (001) substrates by MBE, using solid Ga, $As_2$, and In sources, and the surface reconstruction was monitored *in situ* with an 18 keV RHEED source.

For the uncapped, single layer InAs QD sample, the sample contained an initial 500 nm thick GaAs buffer layer grown at 580 °C with a growth rate of 1 μm/hr and a V/III beam-equivalent pressure ratio of ~17. Next, the buffer surface was annealed at 580 °C for 3 minutes, followed by 3 minutes of annealing at 530 °C with half of the original $As_2$ flux.[17] Finally, 3 ML of InAs was deposited at 500 °C at a rate of 0.1 ML/s. For all layers, a constant Si cell temperature was maintained, with a targeted free carrier concentration n = $6.8 \times 10^{18}$ $cm^{-3}$, corresponding to an average inter-dopant spacing of 5.7 nm. The sample was grown using $As_2$ on a c(4x4)β GaAs surface.[18] Following the growth, the sample was cooled from 500° C to 300° C in 15 minutes under As flux to prevent GaAs decomposition due to As evaporation from the sample surface. Once the sample reached 300° C, the As shutter and needle valve were closed completely before the sample was cooled from 300° C to room temperature within 10 minutes and transferred to the buffer chamber. This approach is expected to lead to the formation of a few monolayers of WL, followed by the nucleation of islands (i.e. QDs), via the Stranski-Krastanov (SK) growth mode transition.[19] For SThEM measurements, we aim for QDs with diameters and nearest neighbor separation at least 2x the phonon mean free path, i.e. > ~10 nm, such that the QDs can be distinguished from each other and from the WL. Thus, the MBE growth conditions were chosen accordingly.

For the multi-layer, capped sample for APT, the sample contained an initial 500 nm thick GaAs buffer layer grown at 580 °C with a growth rate of 1 μm/hr and a V/III beam-equivalent pressure ratio of ∼12. Next, the buffer surface was annealed at 580°C for ∼3 minutes. Subsequently, the substrate temperature was ramped to 500 °C. 5 layers of 3 ML InAs were deposited at a rate of 0.1 ML/s, separated by 30 nm GaAs layers deposited at a

rate of 0.3 μm/hr. Finally, a 50 nm GaAs cap was deposited at a rate of 1 μm/hr. For all layers, a constant Si cell temperature was maintained, with a targeted free carrier concentration n = $6.8 \times 10^{18}$ $cm^{-3}$. The sample was grown using $As_2$ on a (2×4) GaAs surface. Following the growth, the sample was cooled from 500° C to 300° C in 15 minutes under As flux to prevent GaAs decomposition due to As evaporation from the sample surface. Once the sample reached 300° C, the As shutter and needle valve were closed completely before the sample was cooled from 300° C to room temperature within 10 minutes and transferred to the buffer chamber.

### 4.4 Plan-view STM of InAs QDs

The surface morphology of the InAs QDs was examined *ex situ* with tapping mode AFM, as shown in Fig. 4.1 (a). These growth conditions led to a Gaussian distribution of QD sizes with an average diameter of 28 ± 11 nm and a 2D QD density of ~$3 \times 10^{10}$ $cm^{-2}$. Details about the QD size distribution are presented in Appendix J. The sample was then transferred in air to the UHV Park STM/SThEM where multiple large-area STM scans were utilized to locate large, isolated QDs (i.e. surrounded by WL), such as that outlined in blue in the AFM image in Fig. 4.1 (a) and shown in the STM image in Fig. 4.1 (b), which was used for the SThEM measurement. Due to the requirement of tip-sample contact during SThEM measurements, subsequent STM images, such as the one in Fig. 4.1 (b), typically do not exhibit atomic resolution.

## 4.5 SThEM across a single InAs QD

The SThEM trajectory across the QD is shown in Fig. 4.1(c). At the metal tip-semiconductor contact,[20] the induced depletion zone is expected to be 5.0 nm, smaller than the average inter-dopant spacing, suggesting that the contact is effectively ohmic. Furthermore, the length scale of the induced temperature gradient is on the order of tens of nm, comparable to or larger than the phonon mean free path.[14,21,22]

Since the InAs QD sample for SThEM is uncapped, it is important to consider the possibility of an oxidation layer on the surface that could interfere with the SThEM results. For an oxidation layer to influence the thermoelectric voltage, it must have a significant value of S and a thickness greater than the phonon mean free path, i.e. > 5 nm. The oxidation layer on the surface of InAs QDs is typically 1-2 nm and is primarily composed of $In_2O_3$ or other nonstoichiometric oxides such as $InO_x$ with a bandgap value of ~3.5-3.8 eV. [23-25] For our samples, STS reveals an effective band gap in excess of 2 eV, with the Fermi level positioned deep inside the gap (i.e. available electronic states are far from the Fermi level). Thus, S of the oxide layer is expected to be insignificant, and the oxide is not expected to contribute to $V_{SThEM}$. The insignificant influence of surface oxidation on the thermoelectric voltage is further supported by our measurement of an air-exposed p-type GaAs sample, for which similar values of S from $V_{SThEM}$ and bulk measurements were obtained.[26] STS measurements of the InAs QD surface and SThEM measurements on p-type GaAs are presented in Appendix J.

## 4.6 Conversion of $V_{SThEM}$ to free carrier concentration

For tip-sample temperature differences, ($T_{Sample}$-$T_{Tip}$) < 30 K, the position-dependent S(x) is typically temperature-independent, and $V_{SThEM}$ profile, $V_{SThEM}(x)$, is proportional to ($T_{Sample}$-$T_{Tip}$). Thus, $V_{SThEM}(x)$ is related to S(x) according to

$$V_{SThEM}(\mathrm{x}) = f(\mathrm{x}) \times (T_{Sample} - T_{Tip}) \times S(\mathrm{x}) \qquad (4.1)$$

where $T_{Tip}$ and $T_{Sample}$ are the temperatures of the room-temperature tip and the heated sample, S(x) is the Seebeck coefficient profile, and f(x) is the position-dependence of the fraction of the temperature drop which contributes to the thermoelectric voltage in the sample, as described in detail in Section 2.5.1 and Appendix B. Using Fourier's law[27], f(x) is calculated for a given tip and sample using[21]

$$f(\mathrm{x}) = \frac{T_{Sample} - T_{Contact}}{T_{Sample} - T_{Tip}} \approx \frac{\kappa_{Tip} \tan\left(\frac{\theta_{Tip}}{2}\right)}{\kappa_{Tip} \tan\left(\frac{\theta_{Tip}}{2}\right) + 2\kappa_{Sample}(\mathrm{x})} \qquad (4.2)$$

where $T_{Contact}$ is the unknown temperature at the tip-sample contact point. $\theta_{Tip}$ is the cone angle, as shown in Fig. 4.1 (c), and scanning electron microscopy images of similar tips reveal $\theta_{tip} = 25°$. $K_{Tip}$ is the thermal conductivity of the tip, $\kappa_W = 173$ W/mK. To determine the position-dependent thermal conductivity of the sample, $\kappa_{sample}(x)$, we use literature values of κ for $In_xGa_{1-x}As$ alloys, with a profile of $x_{In}$ values based upon those from a similar elastically-relaxed InAs/GaAs QD.[28] We consider a 2D composition map consisting of the in-plane, x, and out-of-plane, z, directions, where z is the growth direction. To account for the phonon mean free path-limited spatial resolution of SThEM, we perform a 2D (x-z) moving average over 5 x 5 nm$^2$ regions, followed by extraction of a 1D $x_{In}$

profile from a line cut through the QD center, defined as the position of highest $x_{In}$. The details of this composition averaging and a sensitivity analysis are presented in Appendix J. The resulting averaged 1D $x_{In}$ profile and position-dependence of $\kappa_{sample}(x)$ are shown in Figs. 4.2(a) and (b), respectively.[29] The f-factor ranges from 0.69 in the WL to 0.8 in the QD center, as shown in Fig. 4.2(c).

Figure 4.3(a) shows the thermoelectric voltage, $V_{SThEM}(x)$, measured along the yellow dashed-line trajectory of the QD shown in Figs. 4.1(b) and (c). In the plot, "0" marks the center of the InAs QD. We note that the measured $V_{SThEM}$ is negative due to electron-dominated transport in the n-type semiconductor. Interestingly, $V_{SThEM}$ reaches a maximum value at $x \approx \pm 10$ nm, which corresponds to the edges of the QD. Using Eq. 4.1, $V_{SThEM}$ (x) is converted to S(x), as shown in Fig. 3(b). The resulting S(x) also exhibits maxima at the edges of the QD.

To extract the conduction band structure from S(x), we assume a single parabolic band, ignoring the contribution from holes. Since the sample is degenerately-doped, the Fermi level, $E_F$, is located far above (>> $k_BT$) the conduction band, $E_C$. Since S is most sensitive to the density of states near $E_F$, the contributions of any quantum confined states are expected to be negligible. Thus, S is expressed as

$$S(x) = -\frac{\pi^2 k_B (r + 3/2)}{3e(E_F - E_C(x))/k_B T} \tag{4.3}$$

where $k_B$ is the Boltzmann constant, e is the elementary charge, and r is the scattering parameter (typically r = 1/2 due to the combination of acoustic phonon and ionized impurity scattering in GaAs and InAs).[30] In Fig 4.3(c), the resulting $E_C$ with respect to the Fermi level ($E_C$-$E_F$) is plotted as a function of x. $E_C(x)$ is lower at the InAs-rich QD center

relative to the GaAs-rich WL, and maxima occur at the QD edges ($x \approx \pm 10$ nm) due to band-bending at the QD/WL interface.

Finally, the carrier concentration profile, n(x), is expressed as

$$n(x) = 4\pi\left[\frac{2m^*(x)k_BT}{h^2}\right]^{3/2} F_{1/2}\left[\frac{E_F - E_C(x)}{k_BT}\right] \tag{4.4}$$

where h is the Planck constant, m* is the effective mass of electrons in the conduction band, and $F_j(\eta)$ is the $j^{th}$ Fermi integral given by

$$F_j(\eta) = \int_0^\infty \frac{\xi^j}{\exp(\xi - \eta) + 1} d\xi \tag{4.5}$$

To determine the effective mass profile, m*(x), shown in Fig. 4.4(a), we use linear interpolations of the binary compound effective masses, $m^*_{InAs}=0.023m_e$ and $m^*_{GaAs}=0.067m_e$, with the profile of $x_{In}$ shown in Fig. 4.2(a). Using the m*(x) in Fig. 4.4(a), the resulting position-dependent carrier concentration, n(x), is plotted in Fig. 4.4(b). The carrier concentration is significantly lower at the QD center than in the WL, with minimum values of n at the QD/WL interfaces. Interestingly, the value of n(x) at the QD center is 75% of that within the WL, despite the intended uniform doping across all layers. [31] The observed local reduction in n at the QD center may be due to limited dopant incorporation within the QDs, free carrier trapping in the QD, or free carrier expulsion from the QD.

### 4.7 Poisson-Schrodinger band structure calculations of InAs QD

For comparison, we use the $x_{In}$ profile from Fig. 4.2(a) to calculate the conduction band edge, $E_{C_1D}(x)$, using various n-profiles as input into a 1D Poisson-Schrodinger (P-

S) solver.[32] Further details of this calculation, including the materials parameters and exact script used for the program "1D Poisson," are located in Appendices C and H, respectively. For an n-profile with n = 5.9 x $10^{18}$ $cm^{-3}$ in the WL, n = 3 to 3.5 x $10^{18}$ $cm^{-3}$ at the QD edges, and n = 4.5 x $10^{18}$ $cm^{-3}$ at the QD center, as shown in blue lines in Fig. 4.4(b), we calculate a conduction band edge profile, $E_{C_1D}(x)$, shown in blue in Fig. 4.3(c). $E_{C_1D}(x)$ and $E_C(x)$ both exhibit maxima at the edges of the QD, similar to a recent report by Shusterman et al. [33] To consider alternative phenomena at the QD edges, such as a non-constant tip contact area or inhomogeneous doping, we computed $E_{C_1D}(x)$ using a constant $x_{In}$ value = 0.26 across the QD. Since the combination of maxima at the QD edges and minimum at the QD center is not reproduced in that case, the maxima are likely a result of band-bending at the InAs-rich QD/ GaAs-rich WL interfaces.

**4.8 Atom probe tomography investigations of dopant distribution**

To directly examine the position of the Si dopant atoms in InAs/GaAs QDs, we use atom probe tomography (APT). APT is an ex-situ, destructive technique which allows 3D reconstruction of a material with nearly atomic resolution.[34] Conical samples, called tips, are placed in an electric field, and ions are ripped from the surface using either voltage or laser pulsing. The ions are collected on a position-sensitive detector, and the time of flight is recorded, allowing a 3D reconstruction of the tip. APT data was collected by the author and Dr. A.S. Chang using a CAMECA LEAP 4000X Si system in the Michigan Center for Materials Characterization. APT tips were prepared using the procedure described in Section 2.5.1 of Dr. A. Chang's thesis.[35]

Ions were collected from prepared sample tips in laser mode with a detection rate of 0.1% and evaporation field of 15 V/nm, with a laser pule rate of 200 kHz and power 0.838 pJ at 20K. Appendix K presents further details of the APT procedures and analysis. The reconstruction of the tip is presented in Fig. 4.5(a), superimposed on an SEM image of the tip. Indium atoms are shown in blue, and isosurfaces with indium concentration $x_{In} > 0.05$ appear yellow, showing well-defined QD wetting layers. Cross-sections of the InAs WLs, (b) layer 3 (top), (c) layer 2 (middle), and (d) layer 3 (bottom) are shown with isosurfaces of $x_{In} > 0.25$ in yellow, revealing QDs with diameters ~5-10 nm.

For each layer, the Si dopant concentration is analyzed in several areas: the GaAs spacer, a section of the WL not including QDs (WL defined by $x_{In} = 0.05$ isosurfaces), a section of the WL including QDs, and the QD only, defined by the x = 0.25 isosurfaces. Details of this procedure are located in Appendix K. The resulting Si dopant concentration (atoms/volume) as a function of layer is presented in Figure 4.6. The Si concentration in the GaAs spacer (black) and WL not including QDs (red) is less than $5 \times 10^{18}$ cm$^{-3}$ and does not vary by layer. The Si concentration in the QDs (blue) is significantly larger than that in the GaAs spacer or WL, with values ranging from $1.2\text{-}2.2 \times 10^{19}$ cm$^{-3}$, while the SThEM results suggest a reduced carrier concentration at the QD center. In the final area examined, a section of the WL including QDs (green), the Si concentration is in between that of the GaAs spacer and the QDs, but a clear correlation with layer is observed, where the Si concentration increases from the bottom layer to the top layer.

### 4.9 Discussion

Recently, reduced doping within QDs has been reported by several groups and explained by a number of models. In the "self-purification" model, for small QDs, dopant incorporation on the QD surface is energetically favored over its incorporation at the QD center.[36] For example, it has been reported that dopants such as Mn are expelled from capped InAs QDs.[37] In the framework of the "self-purification" model, Si dopant incorporation at either the surface or core is predicted to occur for InAs QDs larger than 60nm diameter. Thus, the "self-purification" model might explain the reduced value of n inside the QD compared to the WL. In the case of epitaxial QDs, an apparently reduced n inside capped InAs QD layers has been attributed to carrier trapping at dislocations.[11,14,38,39] For SK InAs/GaAs QDs, high-resolution TEM studies have revealed misfit dislocations at the substrate/QD interface[40] or within the QD.[38]

The SThEM results indicate a reduced carrier concentration inside the QD relative to that in the WL, while the APT results indicate an increased Si dopant concentration inside the QDs relative to the WL. Therefore, it is possible that a fraction of Si atoms within the InAs QDs are electronically inactive or that carrier trapping within in the QDs is responsible for the decreased carrier concentration; however, further analysis is needed.

Furthermore, the correlation with growth layer of Si concentration in the section of the WL including QDs suggests the dopant incorporation mechanism is dependent on the growth layer. The larger Si concentration in the WL around the QDs at the higher growth layers (2 and 3) indicates a buildup of Si dopants in the vicinity of the QD as the growth

progresses, which could indicate a saturation effect of the dopant concentration within single QDs.

### 4.10 Summary and Conclusions

In summary, we have profiled the local carrier concentration across a uniformly- and degenerately-doped uncapped InAs SK QD grown on GaAs. We converted the local S profile to a local n profile assuming a single parabolic band with literature values for the effective masses. A comparison of the corresponding conduction band-edge profile with Poisson-Schrodinger band-edge simulations revealed a reduced carrier concentration in the QD center in comparison to that of the WL. This local reduction in n at the QD center suggests that either the free carriers are trapped at the QD centers, or that the dopants prefer to incorporate into the WL rather than into the QD. We further use 3D atom probe tomography to profile the distribution of Si dopants. Preliminary data indicates a higher Si dopant concentration within the QDs than in the surrounding WL, with an increase in the number of dopants in the vicinity of the QD with growth layer.

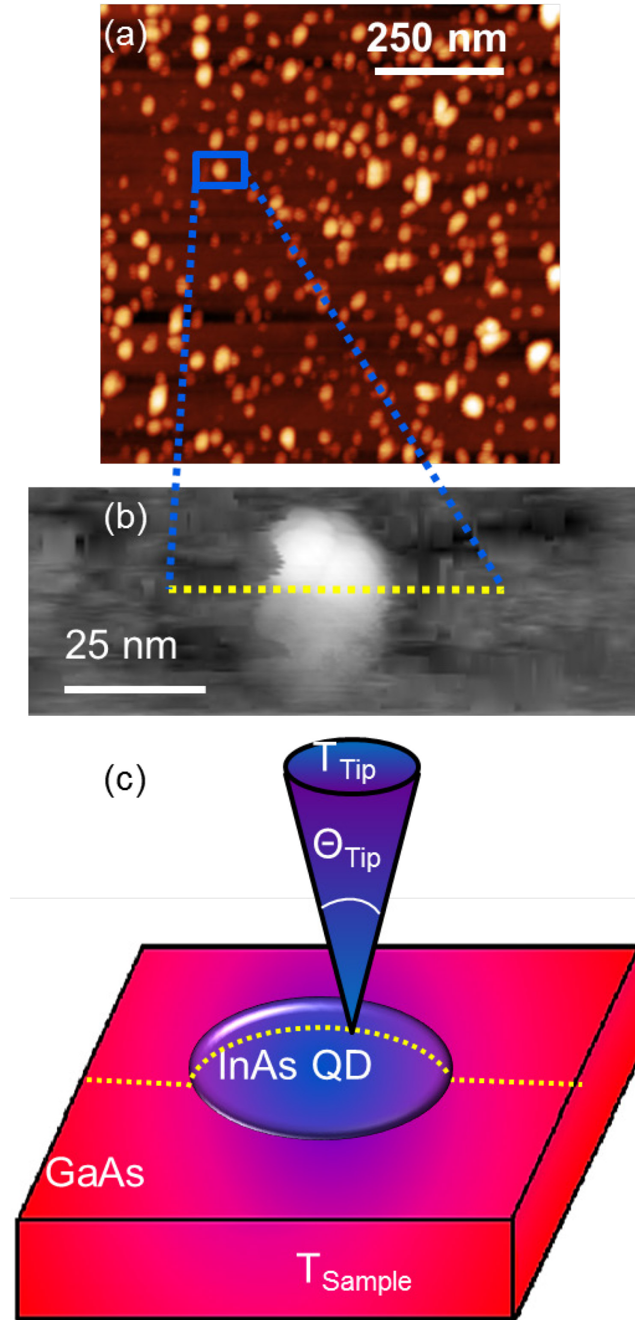


Figure 4.1: (a) Tapping mode AFM image of an uncapped InAs SK QD ensemble. (b) Plan-view STM image of an isolated QD used for the SThEM measurement. Due to the requirement of tip-sample contact during SThEM measurements, the tip often does not retain its atomic resolution. Thus, subsequent STM images typically do not exhibit atomic resolution. (c) Schematic of SThEM setup, which consists of a room temperature probe tip (i.e. $T_{Tip}$ = room temperature) in contact with a heated sample (i.e. $T_{Sample} > T_{Tip}$). The thermoelectric voltage at each tip-sample contact point is measured along the yellow dashed line shown in (b) and (c). Reprinted with permission from Ref. 1 (Copyright 2015, AIP Publishing LLC).

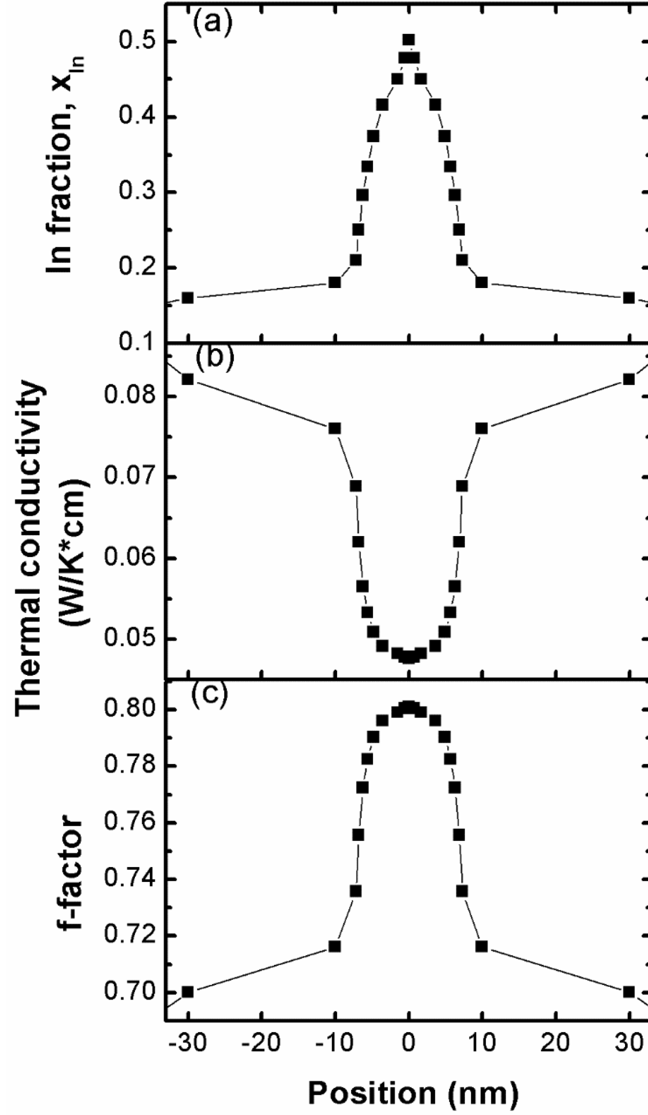


Figure 4.2: Position-dependence of the local (a) indium fraction, $x_{In}$, (b) thermal conductivity, $\kappa_{sample}$, and (c) f-factor, f(x). To determine the In fraction profile across the SK QD in (a), we perform a 2D (x-z) moving average over 5 x 5 $nm^2$ regions of the In composition map in Ref. 28, followed by extraction of a 1D $x_{In}$ profile from a line cut through the QD center, defined as the position of highest $x_{In}$. The resulting averaged 1D $x_{In}$ profile and position-dependence of $\kappa_{sample}(x)$ are shown in (a) and (b), respectively. For (c), $\kappa_{sample}(x)$ was used as input into Eq. 4.2 to determine f(x). Reprinted with permission from Ref. 1 (Copyright 2015, AIP Publishing LLC).

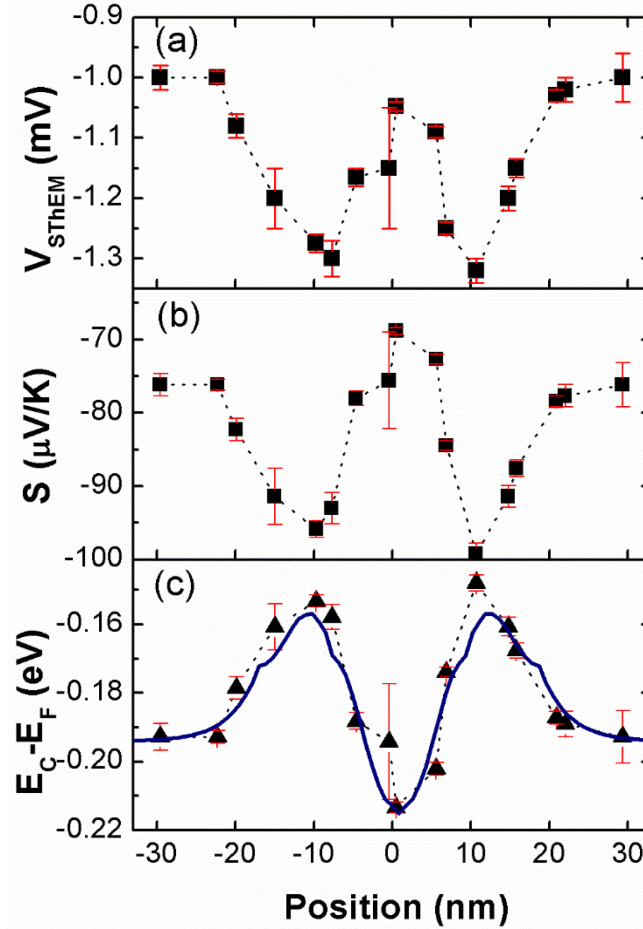


Figure 4.3: (a) $V_{SThEM}(x)$, the measured thermoelectric voltage, as a function of position across the QD, as shown in Fig. 4.1(b). $V_{SThEM}(x)$ is negative due to electron-dominated transport in the n-type semiconductor; $V_{SThEM}(x)$ reaches a maximum at $x \approx \pm 10$ nm, which corresponds to the edge of the QD. (b) S(x), the position dependence of the Seebeck coefficient, converted from the measured $V_{SThEM}(x)$ using Eq. 4.1. S(x) also exhibits maxima at the edges of the QD. (c) $E_C$-$E_F(x)$, the position dependence of the conduction band edge relative to the Fermi level, converted from S(x) using Eq. 4.3, where the Fermi level is defined at E = 0. $E_{C_1D}(x)$, plotted in blue, is calculated using a 1D Poisson-Schrodinger calculation of the band structure. The maxima in $E_C(x)$ at $x \approx \pm 10$ nm indicate the presence of band-bending at the QD/WL interfaces. Reprinted with permission from Ref. 1 (Copyright 2015, AIP Publishing LLC).

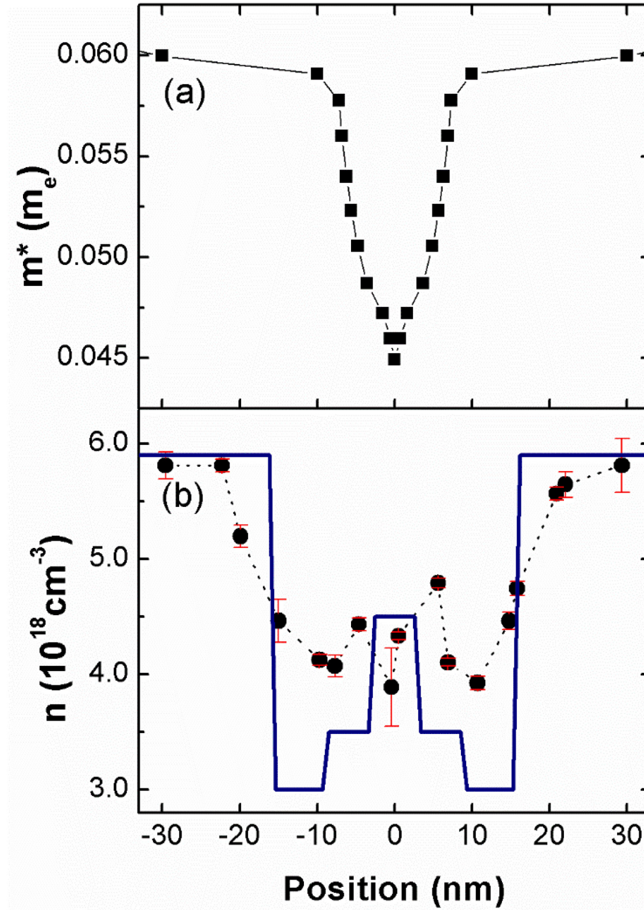


Figure 4.4: Position-dependence of the local (a) effective mass, m*(x), and (b) carrier concentration, n(x). m*(x) is determined using linear interpolations of the binary compound effective masses, $m^*_{InAs}= 0.023m_e$ and $m^*_{GaAs}= 0.067m_e$, and the profile of $x_{In}$ shown in Fig. 2(a). n(x) is converted from $E_C(x)$ using the m*(x) profile shown in (a) and Eq. 4.4. The values of n(x) inside the QD are 75% of those outside the QD, despite the intended uniform doping across all layers. Reprinted with permission from Ref. 1 (Copyright 2015, AIP Publishing LLC).

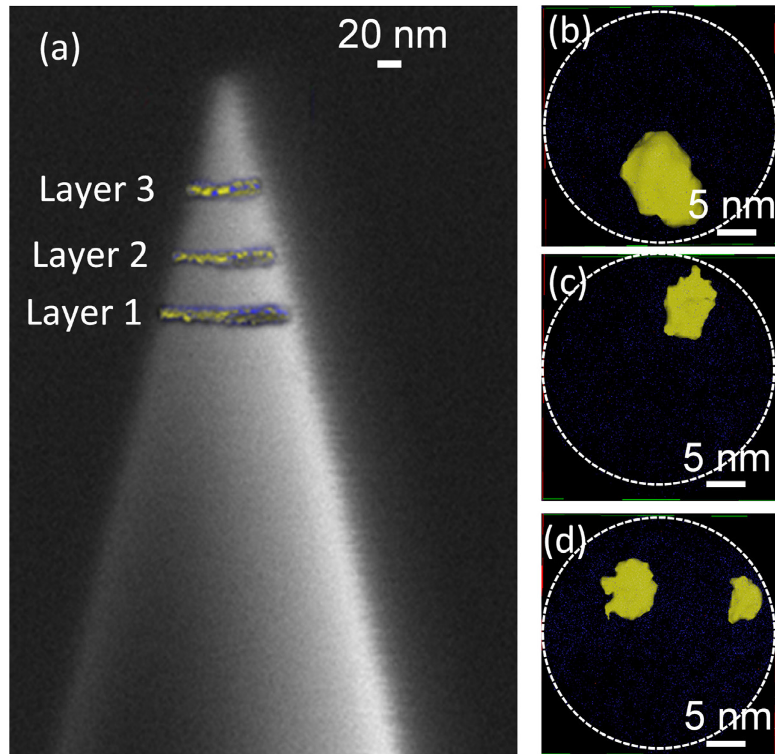


Figure 4.5: (a) Reconstruction of laser-pulsed APT data of InAs/GaAs QDs superimposed on an SEM image of the tip. Indium atoms are shown in blue, where isosurfaces with indium concentration $x_{In} > 0.05$ appear yellow, revealing well-defined QD wetting layers. A cross-section of the reconstructed data of the InAs QD layers, (b) layer 3 (top), (c) layer 2 (middle), and (d) layer 3 (bottom). Yellow denotes an isosurface of $x_{In} > 0.25$, revealing QDs with diameters ~5-10 nm. Adapted and printed with permission from Ref. 35. (Copyright 2016, A.S. Chang).

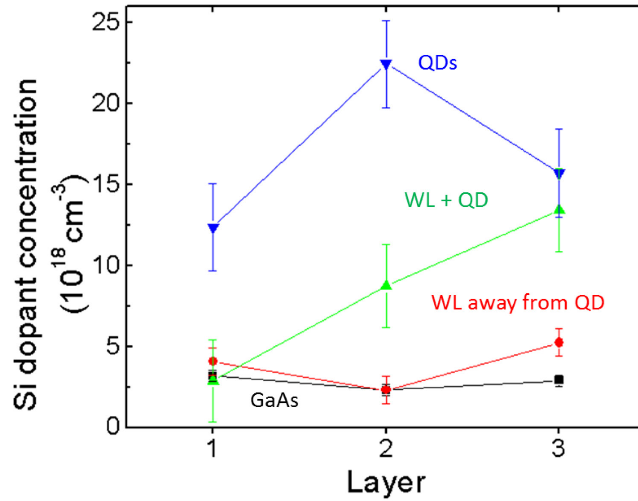


Figure 4.6: For each layer, the Si dopant concentration is analyzed in several areas: the GaAs spacer, a section of the WL not including QDs (WL defined by $x_{In}$ = 0.05 isosurfaces), a section of the WL including QDs, and the QD only, defined by the x = 0.25 isosurfaces. Here the Si concentration is plotted as a function of growth layer. The Si concentration in the GaAs spacer (black) and WL not including QDs (red) is less than 5 x $10^{18}$ cm$^{-3}$ and does not vary by layer. The Si concentration in the QDs (blue) is significantly larger than that in the GaAs spacer or WL, with values ranging from 1.2-2.2 x $10^{19}$ cm$^{-3}$, while the SThEM results suggest a reduced carrier concentration at the QD center. Therefore, it is possible that a fraction of Si atoms within the InAs QDs are electronically inactive or that carrier trapping within in the QDs is responsible for the decreased carrier concentration In the section of the WL including QDs (green), the Si concentration is in between that of the GaAs spacer and the QDs, but a clear correlation with layer is observed, where the Si concentration increases from the bottom layer to the top layer, which could indicate a saturation effect of the dopant concentration within single QDs.

## 4.11 References

[1] J. C. Walrath, Y. H. Lin, S. Huang, and R. S. Goldman, *Appl. Phys. Lett.* **106**, 192101 (2015).

[2] A. Marti, E. Antolin, C. R. Stanley, C. D. Farmer, N. Lopez, P. Diaz, E. Canovas, P. G. Linares, and A. Luque, *Phys. Rev. Lett.* **97**, 247701 (2006).

[3] S. Huang, A. V. Semichaevsky, L. Webster, H. T. Johnson, and R. S.Goldman, *J. Appl. Phys.* **110**, 073105 (2011).

[4] L. Huffaker, G. Park, Z. Zou, O. B. Shchekin, and D. G. Deppe, *Appl. Phys. Lett.* **73**, 2564 (1998).

[5] J. Phillips, K. Kamath, and P. Bhattacharya, *Appl. Phys. Lett.* **72**, 2020 (1998).

[6] Z. Y. Zhao, C. Yi, K. R. Lantz, and A. D. Stiff-Roberts, *Appl. Phys. Lett.* **90**, 233511 (2007).

[7] N. M. Park, T. S. Kim, and S. J. Park, *Appl. Phys. Lett.* **78**, 2575 (2001).

[8] J. X. Chen, A. Markus, A. Fiore, U. Oesterle, R. P. Stanley, J. F. Carlin, R. Houdre, M. Ilegems, L. Lazzarini, L. Nasi, M.T. Todaro, E. Piscopiello, R. Cingolani, M. Catalano, J. Katcki, and J. Ratajczak, *J. Appl. Phys.* **91**, 6710 (2002).

[9] G. D. Mahan and J. O. Sofo, *Proc. Natl. Acad. Sci.* **93** 7436 (1996).

[10] P. De Wolf, R. Stephenson, T. Trenkler, T. Clarysse, T. Hantschel, and W. Vandervorst, *J. Vac. Sci. Technol., B* **18**, 361 (2000).

[11] J. S. Wang, J. F. Chen, J. L. Huang, P. Y. Wang, and X. J. Guo, *Appl. Phys. Lett.* **77**, 3027 (2000).

[12] J.F. Chen, R.S. Hsiao, Y.P. Chen, J.S. Wang, and J.Y. Chi, *Appl. Phys. Lett.* **87**, 141911 (2005).

[13] J.C. Rimada, M. Prezioso, L. Nasi, E. Gombia, R. Mosca, G. Trevisi, L. Seravalli, P. Frigeri, C. Bocchi, and S. Franchi, *Mater. Sci. Eng., B* **165**, 111 (2009).

[14] P. Frigeri, L. Nasi, M. Prezioso, L. Seravalli, G. Trevisi, E. Gombia, R. Mosca, F. Germini, C. Bocchi, and S. Franchi, *J. Appl. Phys.* **102**, 083506 (2007).

[15] E. Gombia, R. Mosca, S. Franchi, P. Frigeri, and C. Ghezzi, *Mater. Sci. Eng., C* **26**, 867 (2006).

[16] H. K. Lyeo, A. A. Khajetoorians, L. Shi, K. P. Pipe, R. J. Ram, A. Shakouri, C. K. Shih, *Science*, **303**, 816 (2004).

[17] W. Ye, S. Hanson, M. Reason, X. Weng, and R.S. Goldman, *J. Vac. Sci. Technol., B* **23**, 1736 (2005).

[18] S. Huang, J. Kim, R. Levy, X. Q. Pan, and R. S. Goldman., *Appl. Phys. Lett.* **103**, 132104 (2013).

[19] I. N. Stranski and Von L. Krastanow, *Akad. Wiss. Lit. Mainz. Abh. Math. Naturwiss. K1.* **146**, 797 (1939).

[20] The size of the tip-sample contact is assumed to be ~1 nm. The QD is a spherical cap with diameter ~20 nm and height ~8 nm, while the tip is expected to be nearly atomically sharp. Thus, the difference in the tip-surface contact area at the edge and center of the QD is not likely to be larger than a few nm. Unless the tip-sample contact area becomes significantly larger than the phonon mean free path (i.e. >>~5 nm), the contact area is unlikely to significantly affect the measured $V_{SThEM}$.

[21] J. C. Walrath, Y. H. Lin, K. P. Pipe, R. S. Goldman, *Appl. Phys. Lett.* **103**, 212101 (2013).

[22] Z. Bian, A. Shakouri, L. Shi, H. K. Lyeo, and C. K. Shih, *Appl. Phys. Lett.* **87**, 053115 (2005).

[23] Z. B. Chen, W. Lei, B. Chen, Y. B. Wang, X. Z. Liao, H. H. Tan, J. Zou, S. P. Ringer, C. Jagadish, *Nanoscale Res. Lett.* **7**, 486 (2012).

[24] A. Zolotaryov, A. Bolz, A. Schramm, W. Hansen, and R.L. Johnson, *Phys. Stat. Sol. (a)* **204**, 2662 (2007).

[25] K. Smaali, A. E. Hdiy, M. Molinari, and M. Tryon, *IEEE Trans. Electron Devices* **57**, 1455 (2010).

[26] D. A. Allwood, R. T. Carline, N. J. Mason, C. Pickering, B. K. Tanner, and P. J. Walker, *Thin Solid Films* **364**, 33 (2000).

[27] $Q = C\Delta T = \frac{1}{R}\Delta T$ where Q is heat, C is thermal conductance, R is thermal resistance, and T is temperature

[28] A. D. Giddings, J.G. Keizer, M. Hara, G.J. Hamhuis, H. Yuasa, H. Fukuzawa, and P.M. Koenraad, *Phys. Rev. B* **83**, 205308 (2011).

[29] S. Adachi, *J. Appl. Phys.* **54**, 1844 (1983).

[30] A.F. Ioffe, *Semiconductor Thermoelements and Thermoelectric Cooling*, Infosearch Limited, London (1957).

[31] For comparison, we also performed 2D moving averages over 10 x 10 $nm^2$ regions and 30 x 10 $nm^2$ regions, prior to extraction of the 1D $x_{In}$ profile, followed by conversion of $V_{SThEM}(x)$ to n(x), as described above; in all cases, n values at the QD center are lower than those in the WL.

[32] I. H. Tan, G. L. Snider, L. D. Chang, and E. L. Hu, *J. Appl. Phys.* **68**, 4071-4076 (1990).

[33] S. Shusterman, A. Raizman, A. Sher, Y. Paltiel, A. Schwarzman, E. Lepkifker, and Y. Rosenwaks, *Nano Letters* **7**, 2089 (2007).

[34] A. Cerezo, P. H. Clifton, M. J. Galtrey, C. J. Humphreys, T. F. Kelly, D. J. Larson, S. Lozano-Perez, E. A. Marquis, R. A. Oliver, G. Sha, K. Thompson, M. Zandbergen, and R. L. Alvis, *Materials Today* **10**, 36 (2007).

[35] A.S. Chang, Ph.D. Thesis, University of Michigan, 2016.

[36] J.P. Petropoulos, T.R. Christian, P.B. Dongmo, and J.M.O. Zide, *Nanotechnology* **22**, 245704 (2001).

[37] V. D. Dasika, A. V. Semichaevsky, J. P. Petropoulos, J. C. Dibbern, A. M. Dangelewicz, M. Holub, P. K. Bhattacharya, J. M. O. Zide, H. T. Johnson, and R. S. Goldman, *Appl. Phys. Lett.* **98**, 141907 (2011).

[38] L. Nasi, C. Bocchi, F. Germini, M. Prezioso, E. Gombia, R. Mosca, P. Frigeri, G. Trevisi, L. Seravalli, and S. Franchi*, J. Mater Sci : Mater Electron* **19**, 96 (2008).

[39] Z. Y. Zhao, W. M. Zhang, C. Yi, A. D. Stiff-Roberts, B. J. Rodriguez, and A. P. Baddorf, *Appl. Phys. Lett.* **92**, 092101 (2008).

[40] Y. Chen, X. W. Lin, Z. Liliental-Weber, J. Washburn, J. F. Klem, J. Y. Tsao, *Appl. Phys. Lett.* **68**, 111 (1996).

# Chapter 5

## Ordered horizontal $Sb_2Te_3$ nanowires induced by femtosecond lasers

### 5.1 Overview

Chapter 5 presents STM/S and SThEM investigations of the surface composition and band structure of ordered horizontal $Sb_2Te_3$ nanowires induced by femtosecond laser irradiation of a thin film. Initial STM and STS studies revealed a widened band gap in the nanowire region compared to pristine $Sb_2Te_3$, but SThEM indicated the thermoelectric voltage of the nanowires remained unchanged from pristine $Sb_2Te_3$, suggesting the presence of an insulating material surrounding buried nanowires. Cross-sectional transmission electron microscopy (X-TEM) studies confirmed the presence of single-crystal $Sb_2Te_3$ nanowires surrounded by a polycrystalline material, but revealed gaps in this material in some areas of the nanowires. Subsequently, a more targeted STS study directly measured the band gap modulation between the nanowires and insulating material. These horizontal $Sb_2Te_3$ nanowires are promising for a variety of applications, including thermoelectrics and optoelectronics, and the novel fabrication method using fs laser-irradiation in ambient conditions provides a pathway for scalable manufacturing.

The STM/S and SThEM data obtained using the Park STM were collected by the author and Dr. Y.H. Lin, and the STS data obtained using the VT-STM were collected by

the author and Dr. A.S. Chang. The $Sb_2Te_3$ thin film was grown in the laboratory of Prof. Ctirad Uher at the University of Michigan. The formation of the nanowires by laser irradiation was performed by Dr. Y. Li in Prof. Roy Clarke's laboratory in collaboration with Prof. K.P. Pipe. Dr. Y. Li conducted extensive work developing the nanowire formation method and the subsequent characterization, which will be further referenced throughout the chapter. This work was supported by several sources including the Center for Solar and Thermal Energy Conversion, an Energy Frontier Research Center funded by the U.S. Department of Energy, Office of Science, and Office of Basic Energy Sciences under Award No. DE-SC00000957; the U.S. DOE under Award No. DE-PI0000012 and Contract No. DE-FG02-06ER46339; and the National Science Foundation Graduate Student Research Fellowship under Grant No. DGE 1256260. Parts of this work were published in *Applied Physics Letters*.[1]

### 5.2 Background

Semiconductor nanowires are promising for a wide range of applications, including electronic[2] and spintronic[3] devices, thermoelectrics[4] and optoelectronics.[5] In particular, horizontal nanowires oriented along the substrate are often desirable for integrated planar devices such as sensors[6,7] and photo-detectors.[8] Common fabrication methods for horizontal nanowires include vapor-liquid-solid synthesis of vertical nanowires followed by transfer to a substrate[9] and fabrication by patterning with high-resolution lithography.[10,11] However, these fabrication methods require cumbersome post-processing steps or are cost-intensive. Thus, improved fabrication of in-plane nanowires conducive to

large-scale production is needed. Here we present an investigation of the structural and electronic properties of horizontal nanowires fabricated using femtosecond (fs) laser irradiation of an $Sb_2Te_3$ thin film. $Sb_2Te_3$ is of particular interest for nanowire applications due to its excellent thermoelectric[12] and topologically insulating properties.[13] Here STM, STS, and SThEM are used to investigate the surface morphology of laser-irradiated horizontal $Sb_2Te_3$ nanowires as well as the buried structures beneath the surface, which have not been well explored.[14-16]

### 5.3 MBE growth and nanowire formation

The details of the nanowire formation method can be found in the thesis of Dr. Y. Li as well as the works published in *Applied Physics Letters* by Dr. Y. Li et al., but a brief overview is provided in this section.[1,17,18] The 100 nm $Sb_2Te_3$ film was grown on a *c*-plane sapphire substrate with a 10 nm $Bi_2Te_3$ buffer layer, shown in Fig. 5.1. The sample is mounted on a translation stage and irradiated with a femtosecond laser (1560 nm, 150 fs) at a scan rate of 5 μm/s and fluence of 14 mJ/cm$^2$ at room temperature in ambient conditions. The laser is scanned along the film, forming nanowires perpendicular to the laser polarization. A portion of the film was left unaltered, leaving a large section of pristine $Sb_2Te_3$.

## 5.4 STM and SThEM studies

We used the Park STM to investigate the structure and electronic properties of the nanowires using STM, STS, and SThEM. Traditional electronic and Seebeck measurements, with contacts made on top of the nanowires, indicated the sample was completely insulating. One goal of the STS and SThEM studies was to test whether the nanowires were indeed insulating, or if the laser irradiation merely formed an insulating phase on the surface of the nanowires. An STM image of the nanowires is shown in Figure 5.2(a). The nanowires are typically ~100 nm in diameter and separated by valleys of 50-100 nm. To investigate the electronic structure of the surface, we used STS to measure the effective bandgap in the region of the nanowires and the pristine $Sb_2Te_3$ thin film. The dI/dV as a function of bias voltage is plotted in Fig. 5.2(b) for the unmodified $Sb_2Te_3$ film and the irradiated surface of the nanowires. dI/dV collected on the pristine $Sb_2Te_3$ revealed an effective band gap ~0.2 eV, consistent with that of bulk $Sb_2Te_3$.[19] However, dI/dV collected in the laser-irradiated region revealed an insulating phase, with a band gap in excess of 1.5 eV.

To probe beneath the surface of the nanowires, we used SThEM to measure the thermoelectric voltage inside and outside the irradiated region. Figure 5.3(a) illustrates the different regions probed by SThEM and STS. As explained in Section 4.5, SThEM is able to probe buried nanostructures for two reasons: First, as explained in Section 2.5.3, the tip is pressed firmly into the sample to ensure good thermal and electrical contact. In this process, the tip may dig a few nm into the surface of the sample.[20] Second, as explained in detail in Chapter 3, SThEM measured a spatially-averaged thermoelectric voltage, $V_{SThEM}$,

over a region up to 10's of nm. Thus, SThEM is able to probe beneath a sufficiently small insulating layer.

The SThEM results are plotted in Fig. 5.3(b). On the left are measurements of $V_{SThEM}$ taken in the unmodified region, and on the right are measurements taken on the irradiated nanowires. The average $V_{SThEM}$ values are indicated by the horizontal dashed lines. $V_{SThEM}$ of the pristine $Sb_2Te_3$ is 2.15 ± 0.1 mV, and $V_{SThEM}$ of the nanowires is 2.24 ± 0.07 mV, where the errors represent the standard deviation of the data. Thus, $V_{SThEM}$ does not differ significantly between the irradiated and non-irradiated region. The STS and SThEM results indicate the presents of an insulating phase induced by the laser covering buried, pristine $Sb_2Te_3$ nanowires.

### 5.5 Cross-sectional transmission electron microscopy of $Sb_2Te_3$ nanowires

To investigate the structure underneath the insulating layer, Dr. Yi Li conducted X-TEM imaging of the nanowires. Figure 5.4 shows a high-angular annular dark field (HAADF) image of the $Sb_2Te_3$ nanowires.[1,17] The top of the figure shows well-ordered bright spots, the nanowires, surrounded by a darker material. The bottom figure is zoomed in on this region, revealing a clear distinction between the nanowires and the surrounding insulating phase. Elemental mapping using energy-dispersive x-ray spectroscopy coupled with high-resolution TEM confirms that the material in the nanowires is single-crystal $Sb_2Te_3$, while the insulating phase in the valleys is polycrystalline and primarily comprised of $Sb_2O_3$.[1,17] While the nanowires are mostly covered by this insulating phase, the HAADF image in Figure 5.4 reveals spots where the $Sb_2Te_3$ nanowires are exposed to the surface.

Thus, a more targeted STS investigation could directly measure the band gap of the buried nanowires to confirm their composition and electrical properties.

### 5.6 STS investigations

Using the VT-STM, we conducted further investigations of the nanowires. Figure 5.5(a) illustrates the locations probed by STS, including the valley between the nanowires and the regions on the surface of the nanowires not fully covered by the insulating phase. The dI/dV versus bias voltage is plotted in Figure 5.5(b). dI/dV of the valley (red) reveals an effective band gap in excess of 1.5 eV, consistent with the previous STS results. However, dI/dV of the nanowire surface (black) reveals an effective band gap ~ 0.2 eV, consistent with that of the unmodified $Sb_2Te_3$ film. Thus, the STS results indicate a substantially increased bandgap in the region between the nanowires compared to that of the $Sb_2Te_3$ nanowires, consistent with the presence of a $Sb_2O_3$ polycrystalline phase which is much more electrically insulating than $Sb_2Te_3$.

### 5.7 Summary and Conclusions

We have conducted STM/S and SThEM investigations of the composition and band structure of ordered horizontal $Sb_2Te_3$ nanowires induced by femtosecond laser irradiation of a thin film. Initial STM and STS studies revealed a widened band gap in the nanowire region compared to that of pristine $Sb_2Te_3$, but SThEM investigations indicated that the thermoelectric voltage of the nanowires remained unchanged from pristine $Sb_2Te_3$. The

presence of an insulating material surrounding buried nanowires was confirmed by cross-sectional TEM studies. With subsequent STS studies we directly measured the band gap modulation between the $Sb_2Te_3$ nanowires and insulating material. These horizontal $Sb_2Te_3$ nanowires are promising for a variety of applications, including thermoelectrics and optoelectronics, and the novel fabrication method using fs laser-irradiation in ambient conditions provides a pathway for scalable manufacturing.

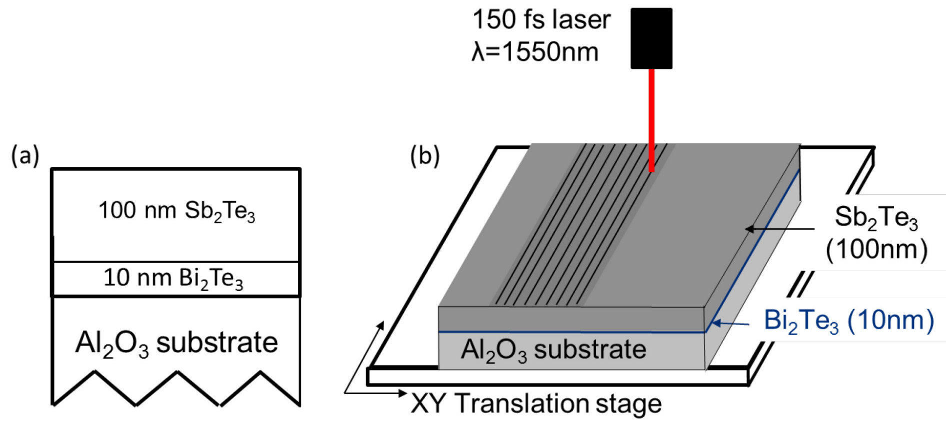


Figure 5.1: Schematic of $Sb_2Te_3$ film composition and laser irradiation method. (a) Cross-sectional view of the sample structure where the 100 nm $Sb_2Te_3$ film was grown on a *c*-plane sapphire substrate with a 10 nm $Bi_2Te_3$ buffer layer. (b) The sample is mounted on a translation stage and irradiated with a femtosecond laser (1560 nm, 150 fs) at a scan rate of 5 μm/s and fluence of 14 mJ/cm$^2$ at room temperature in ambient conditions.

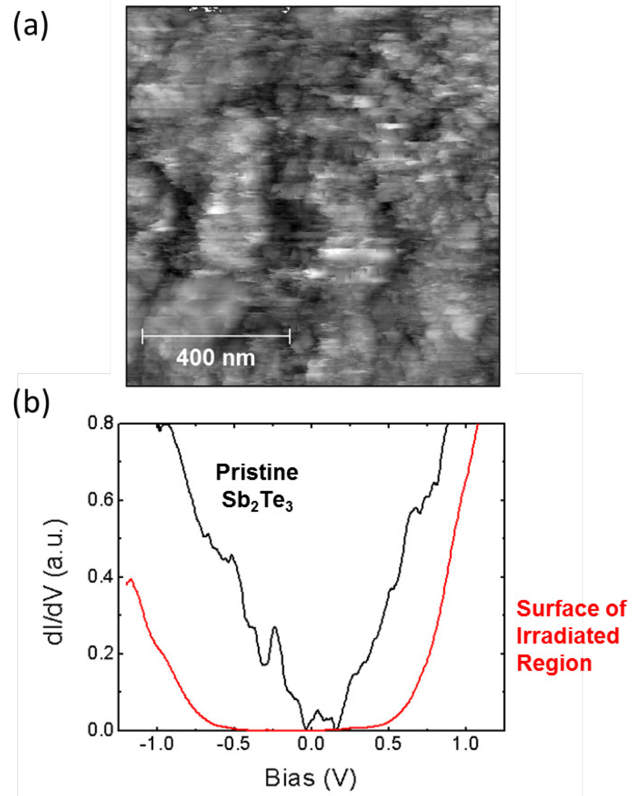


Figure 5.2: (a) STM image of the nanowires, revealing nanowires with diameters ~100 nm and separated by valleys of 50-100 nm. The color scale of this image represents a height difference $\Delta z = 40$ nm. (b) dI/dV as a function of bias voltage for the unmodified $Sb_2Te_3$ film (black) and the irradiated surface of the nanowires (red). dI/dV collected on the pristine $Sb_2Te_3$ reveals an effective band gap ~0.2 eV, while dI/dV collected in the laser-irradiated region revealed an insulating phase, with a band gap in excess of 1.5 eV.

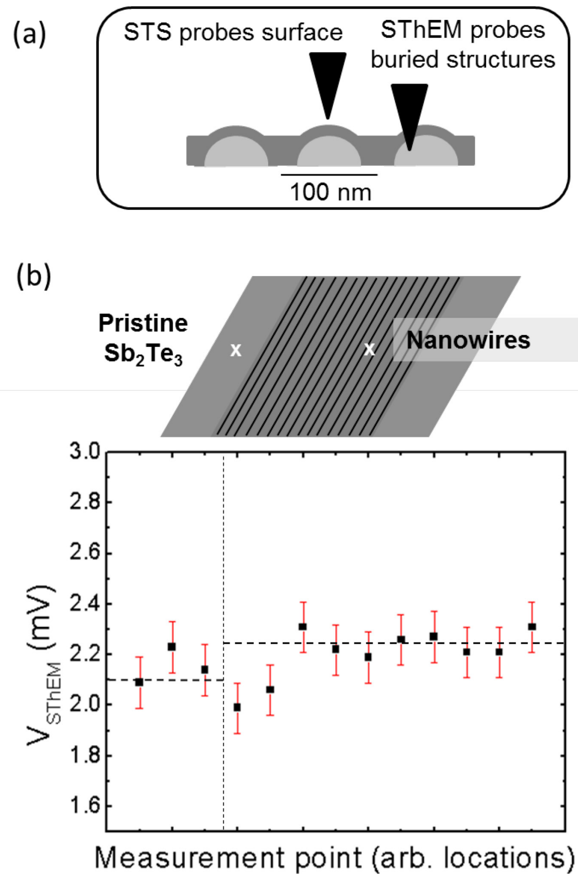


Figure 5.3: (a) Illustration of the different regions probed by SThEM and STS. STS probes the first few atomic layers of the surface, while SThEM is able to probe buried structures. (b) SThEM measurements taken in the unmodified region (left) reveal $V_{SThEM} = 2.15 \pm 0.1$ mV, and the measurements taken on the irradiated nanowires (right) $V_{SThEM} = 2.24 \pm 0.07$ mV. The errors represent the standard deviation of the data. Thus, $V_{SThEM}$ does not differ significantly between the irradiated and non-irradiated region.

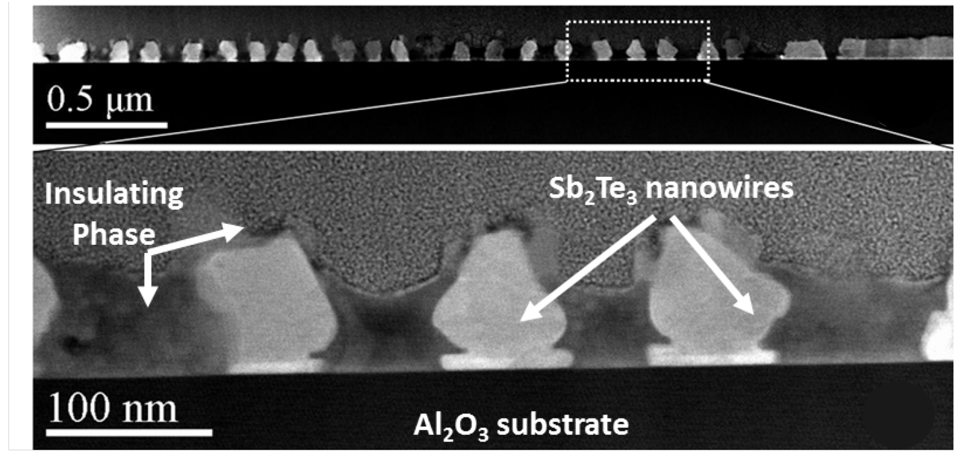


Figure 5.4: HAADF image of the $Sb_2Te_3$ nanowires. The top of the figure shows well-ordered bright spots, the nanowires, surrounded by a darker material. The bottom figure is zoomed in on this region, revealing a clear distinction between the nanowires and the surrounding insulating phase. Adapted and printed with permission from Ref. 1 (Copyright 2014, AIP Publishing LLC).

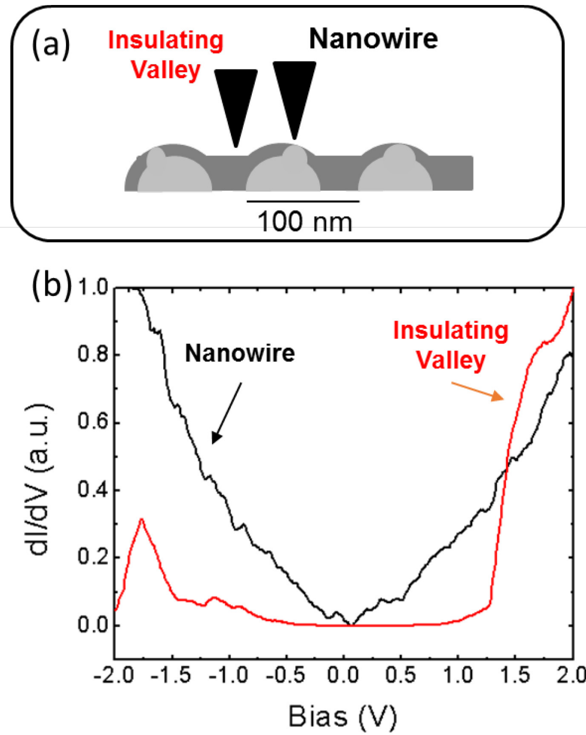


Figure 5.5: (a) Illustration of the locations probed by STS, including the valley between the nanowires and the regions on the surface of the nanowires not fully covered by the insulating phase. (b) dI/dV versus bias voltage of the valley (red) reveals an effective band gap in excess of 1.5 eV, consistent with the previous STS results. However, dI/dV of the nanowire surface (black) reveals an effective band gap ~ 0.2 eV, consistent with that of the unmodified $Sb_2Te_3$ film. Adapted and printed with permission from Ref. 1 (Copyright 2014, AIP Publishing LLC).

## 5.8 References

[1] Y. Li, V. A. Stoica, K. Sun, W. Liu, L. Endicott, J. C. Walrath, A. S. Chang, Y. H. Lin, K. P. Pipe, R. S. Goldman, C. Uher, and R. Clarke, *Appl. Phys. Lett.* **105**, 201904 (2014).

[2] J. Xiang, W. Lu, Y. Hu, Y. Wu, H. Yan, C.M. Lieber, *Nature* **441**, 489 (2006).

[3] J. Tang, C. Wang, M. Hung, X. Jiang, L. Chang, L. He, P. Liu, H. Yang, H. Tuan, L. Chen, K.L. Wang, *ACS Nano* **6**, 5710 (2012).

[4] A. I. Hochbaum, R. Chen, R. D. Delgado, W. Liang, E. C. Garnett, M. Najarian, A. Majumdar, P. Yang, *Nature* **451**, 163 (2008).

[5] X. Duan, Y. Huang, Y. Cui, J. Wang, C. M. Lieber, *Nature* **409**, 66 (2001).

[6] S. Zhang, L. Lou, C. Lee, *Appl. Phys. Lett.* **100**, 023111 (2012).

[7] Y. Cui, Q. Wei, H. Park, C.M. Lieber, *Science* **293**, 1289 (2001).

[8] C. Kim, H. Lee, Y. Cho, K. Kang, M. Jo, *Nano Lett.* **10**, 2043 (2010).

[9] Y. Cui, L. J. Lauhon, M. S. Gudiksen, J. Wang, C. M. Lieber, *Appl. Phys. Lett.* **78**, 2214 (2001).

[10] J. Yeon, Y. J. Lee, D. E. Yoo, K. J. Yoo, J. S. Kim, J. Lee, J. O. Lee, S. Choi, G. Yoon, D. W. Lee, G. S. Lee, H. C. Hwang, Y. Yoon, *Nano Lett.* **13**, 3978 (2013).

[11] K. J. Jeon, J. M. Lee, E. Lee, W. Lee, *Nanotechnology* **20**, 135502 (2009).

[12] J. H. Yang and C. Thierry, *MRS Bull.* **31**, 224 (2006).

[13] Y. Jiang, Y.Y. Sun, M. Chen, Y. Wang, Z. Li, C. Song, K. He, L. Wang, X. Chen, Q.K. Xue, X. Ma, and S.B. Zhang, *Phys. Rev. Lett.* **108**, 066809 (2012).

[14] E. M. Hsu, T. H. R. Crawford, C. Maunders, G. A. Botton, H. K. Haugen, *Appl. Phys. Lett.* **92**, 221112 (2008).

[15] M. Couillard, A. Borowiec, H. K. Haugen, J. S. Preston, E. M. Griswold, *J. Appl. Phys.* **101**, 033519 (2007).

[16] E. M. Hsu, N. A. Mailman, G. A. Botton, H. K. Haugen, *Appl. Phys. A* **103**, 185 (2011).

[17] Y. Li, Ph.D. thesis, University of Michigan, 2014.

[18] Y. Li, V. A. Stoica, L. Endicott, G. Wang, H. Sun, K. P. Pipe, C. Uher, and R. Clarke, *Appl. Phys. Lett.* 99, 121903 (2011).

[19] Y. M. Zuev, J. S. Lee, C. Galloy, H. Park, P. Kim, *Nano Lett.* **10**, 3037 (2010).

[20] H.K. Lyeo, Ph.D. Thesis, University of Texas at Austin, 2003.

# Chapter 6

## Identification of topological surface states in $(Bi_{1-x}Sb_x)_2Te_3$ alloy films

### 6.1 Overview

In this chapter, STM and STS are used to investigate the band structure of $(Bi_{1-x}Sb_x)_2Te_3$ alloys at room temperature, revealing both the Fermi level and Dirac point located inside the bulk bandgap, indicating bulk-like insulating behavior with accessible surface states. Prior to this work, direct detection of topological surface states in BiSbTe systems has been achieved for only T < 10 K. However, for device applications, room-temperature identification of topological surface states is needed. This work demonstrates the first direct measurement of topological surface states using STS at room temperature for any material. Additionally, we discuss the alloy composition and film thickness dependence of the band structure and transport properties, showing evidence for a conductive interface layer beneath the insulating bulk.

The STM and STS data were taken by the author in collaboration with the rest of the Goldman STM lab, including Dr. Y.H. Lin, Dr. A. Chang, and Ms. C. Greenhill. The author conducted the analysis of the BiSbTe images and STS data with assistance from Mr. A. Ahsan and Mr. Y. Zhi. The BiSbTe thin films were grown by MBE in the lab of Prof. Ctirad Uher at the University of Michigan, by Dr. V.A. Stoica, Dr. W. Liu, and Mr. L. Endicott. The transport measurements were conducted by Drs. V.A. Stoica, W. Liu, and H.

Chi. This material is based upon work supported by the Department of Energy (DoE) under Award Number DE-PI0000012 and the National Science Foundation Graduate Student Research Fellowship under Grant No. DGE 1256260. Y.H.L. and R.S.G. were also supported in part by the U.S. DoE, Office of Science, Office of Basic Energy Sciences under contract DE-FG02-06ER46339. This work is currently being prepared for publication.

## 6.2 Background

Topological insulators (TIs) have emerged as an exciting class of quantum materials, with a bulk energy band gap and surface states consisting of a single Dirac cone, for which the resulting spin-momentum locking makes them desirable for spintronics and quantum computing. $Bi_2Te_3$ and $Sb_2Te_3$ are of particular interest for spintronics, due to observations that Te anti-site ($Te_{Bi}$) defects ($Bi_2Te_3$) and Sb vacancy ($V_{Sb}$) and Sb anti-site ($Sb_{Te}$) defects ($Sb_2Te_3$) lead to n-type and p-type conduction, respectively.[1,2] Furthermore alloys of $Bi_2Te_3$-$Sb_2Te_3$ may contain combinations of $Te_{Bi}$, $V_{Sb}$, and $Sb_{Te}$ leading to carrier compensation with the Fermi level inside the band gap, forming an insulating bulk. [2] To date, $Bi_2Te_3$-$Sb_2Te_3$ alloying has been reported to induce a mid-gap Dirac point, allowing a decoupling of bulk and surface transport. Prior to this work, direct detection of topological surface states in BiSbTe systems has been achieved only for $T < 10$ K.[2,3] However, for device applications, room-temperature identification of topological surface states is needed.[4] Here, we use STM and STS to reveal a Fermi level and Dirac point both located inside the bulk bandgap, indicating bulk-like insulating behavior with

accessible surface states. This work demonstrates the first direct measurement of topological surface states using STS at room temperature for any material. We discuss the alloy composition and film thickness dependence of the band structure and transport properties, showing evidence for a conductive interface layer beneath the insulating bulk. Thus, while alloying can be used to achieve tunable surface states, the film/substrate interface needs to be carefully considered to achieve an insulating bulk.

## 6.3 Experimental Details

For these investigations, $Bi_2Te_3$-$Sb_2Te_3$ alloy films were grown by MBE on sapphire (0001) substrates, followed by annealing in a tellurium flux for 3.5 hours. The growth conditions were monitored in-situ by reflection high-energy electron diffraction (RHEED KSA 400), and the Bi:Sb ratio was controlled by the temperatures of the Bi and Sb Knudsen-type cells. Several films with varying Sb/Bi fractions and thicknesses were grown, as listed in

Table 6.1, where x is the Sb fraction.

| ***Sample*** | ***x*** | ***Film thickness*** | ***Carrier type*** | ***Band gap (eV)*** |
|---|---|---|---|---|
| A | 0.64 | 18 nm | n-type | 0.19 ± 0.10 |
| B | 0.58 | 30 nm | n-type | 0.20 ± 0.10 |
| C | 0.64 | 30 nm | p-type | 0.21 ± 0.10 |
| D | 0.68 | 6 nm | p-type | 0.20 ± 0.10 |

Table 6.1: $(Bi_{1-x}Sb_x)_2Te_3$ sample composition, thickness, carrier type, and effective band gap measured using STS.

Both STM and STS were performed in UHV (base pressure < 6 x $10^{-11}$ Torr) with electrochemically-etched polycrystalline W[5] and cut Pt/Ir[6] tips, which were cleaned *in situ* by electron bombardment. STS measurements were performed using a modified variable tip-sample separation method, in which the tip-sample separation is maintained constant during acquisition of a given spectrum, but is adjusted between spectra to enable measurements of bulk and surface states.[7-10] Since the band gap is sufficiently larger than $k_BT$ ($E_g$ >> 26 meV), if the Dirac point lies within the band gap, the surface states are detected directly by modifying the tunneling current, and thus the tip-sample separation.[11,12] STS is more (less) sensitive to states near the Fermi level as the tip is moved closer to (away from) the sample. All images were obtained with sample bias voltages ranging from -3 V to 1 V and constant tunneling currents ranging from 100 to 200 pA. Electronic transport properties were measured from 2 K to 300 K in a Quantum-Design Magnetic Property Measurement System by Drs. V.A. Stoica, W. Liu, and H. Chi. In some cases the transport measurements were conducted on samples similar to, but not identical to, those investigated with STM and STS.

**6.4 STM of BiSbTe films**

Figure 6.1 shows large-scale STM images of the surface topography for (a) 18 nm x = 0.64 (b) 30 nm x = 0.58, (c) 30 nm x = 0.64, and (d) 6 nm x = 0.68[13] films. For all samples, line cuts across the images reveal terraces with step heights of ~1 nm, as expected for quintuple layer structures in high-quality layer-by-layer growth of the Van der Waals bonded layers.[14] However, the STM images reveal diverse morphology of the terraces.

Samples B, C, and D have roughly circular terraces and surrounding steps, while sample A has more oblong features. Prior to the STM/S measurement, sample A underwent variable-temperature transport measurements, which likely affected the surface morphology. The terrace sizes vary from around 10-20 nm in sample A to 50-100 nm in samples B, C, and D, and the number of steps around each terrace varies as well, from 1-2 in sample D to 3-5 in samples B and C.

### 6.5 STS of bulk and surface states

Figure 6.2 shows dI/dV as a function of bias voltage, corresponding to the energy relative to the Fermi level. The effective band gaps and carrier types are listed in Table 6-1 above. For all samples, the effective bandgap ranges from 0.19-0.21 ± 0.10 eV, consistent with previous studies of $(Bi_{1-x}Sb_x)_2Te_3$ alloys.[2] Sample A is distinctly n-type, with the Fermi level (black dashed line) located at the conduction band edge. For sample B, $E_F$ is located mid-gap, making it difficult to judge the carrier type from the bulk spectrum alone. Samples C and D show p-type conduction, with $E_F$ at or near the valence band edge. Thus, the Fermi level is tuned across the gap, with an n-p transition occurring with the increasing Sb fraction, x = 0.58 in sample B to x = 0.64 in sample C. The conduction type of BiSbTe alloys is known to shift from p to n (or vice versa) with composition differences of less than 0.1, consistent with our STS observations.[2]

To detect the surface state spectra for samples B and C, we adjust the tip-sample separation to reveal two distinct states of surface and bulk conduction, shown in Figs. 6.3(a) and (b). In Fig. 6.3(a), STS spectra taken on sample B with a lower tunneling impedance

reveal V-shaped spectra within the bulk band gap, indicative of topological surface states, similar to recent STS studies of $Sb_2Te_3$ thin films.[15,16] For sample C in Fig. 6.3(b), the lower tunneling impedance spectra reveal a sharp feature near the conduction band edge. The energy of zero conductance corresponds to the Dirac point, $E_D$. The approximate positions of $E_D$ are marked by arrows on Figs. 6.2(a) and (b). For sample B, $E_D$ is located between the Fermi level, $E_F$, and the valence band edge, while for sample C, $E_D$ is near the conduction band edge. The shift in $E_D$ from below to above $E_F$ indicates a change in carrier type from electrons to holes.[2,17] Both $E_F$ and $E_D$ are located within the bulk band gap, indicating bulk insulating behavior with accessible surface states. No distinct surface state spectra were observed for sample A, suggesting that the Dirac point is buried within the valence band.

### 6.6 Thickness-dependent electrical resistance of BiSbTe films

Resistivity vs. temperature for films of varying thickness is presented in Fig. 6.4 for sample A (18 nm, blue), a sample similar to B (30 nm, red), and an 8 nm film (black). For thin films (8 nm), the resistance increases monotonically as a function of temperature, indicating conductive behavior. For thicker films (>18 nm), the resistivity decreases with temperature, indicating resistive behavior.

A possible explanation for the thickness-dependent conductivity is the presence of a distinct film/substrate interface layer below the bulk insulating layer. Figure 6.5(a) shows the RHEED oscillations as a function of time, and an analysis of the streak spacing as a function of time is shown in Fig. 6.5(b). There is an increase in streak spacing around 275

s, corresponding to a decrease in the lattice constant which could indicate the presence of Bi intercalation resulting in a tsuomoite structure, giving way to the standard tetradymide structure later in the growth. The excess Bi in this growth mode could explain the increased conductivity of the thinner films in Fig 6.4. Figure 6.5(c) shows a cross-sectional view of the sample with the structure suggested by the electrical resistance and RHEED results. At the substrate/growth layer interface is a conductive layer, followed by an insulating layer of BiSbTe. The red lines indicate the topological surface states.

### 6.7 Summary and Conclusions

In summary, we use STM and STS of $(Bi_{1-x}Sb_x)_2Te_3$ alloys to reveal both the Fermi level and Dirac point located inside the bulk bandgap, indicating bulk-like insulating behavior with accessible surface states. However, electrical transport measurements indicate a thickness-dependent resistivity that suggests that the bulk is not uniformly insulating, likely due to a conductive interface layer below the bulk insulating layer. Thus, while alloying can be used to successfully achieve tunable surface states, the film/substrate interface needs to be carefully considered for the achievement of an insulating bulk. This work provides key insight necessary for engineering room-temperature topological insulator devices.

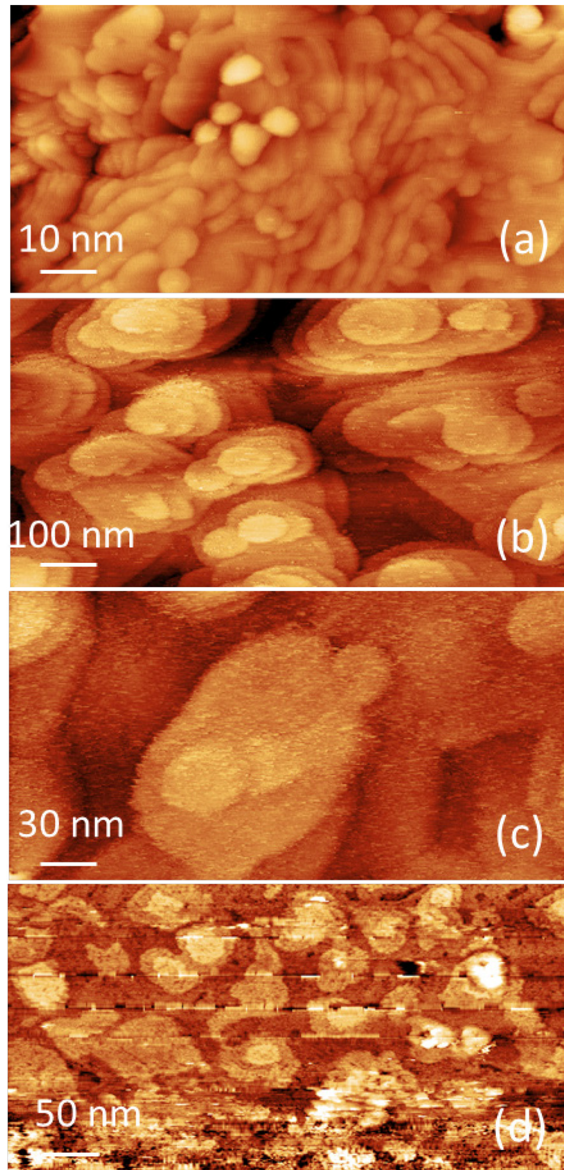


Figure 6.1: Large-scale STM images of the surface topography for (a) 18 nm (Δz = 9.5 nm) (b) 30 nm (Δz = 15.8 nm), (c) 30 nm (Δz = 9.8 nm), and (d) 6 nm (Δz = 15.5 nm) films. For all samples, large terraces with 1 quintuple layer steps are observed, indicating high-quality layer-by-layer growth of the Van der Waals bonded layers. (d) has been adapted and reprinted with permission from Ref. 13 (Copyright 2016, AIP Publishing LLC).

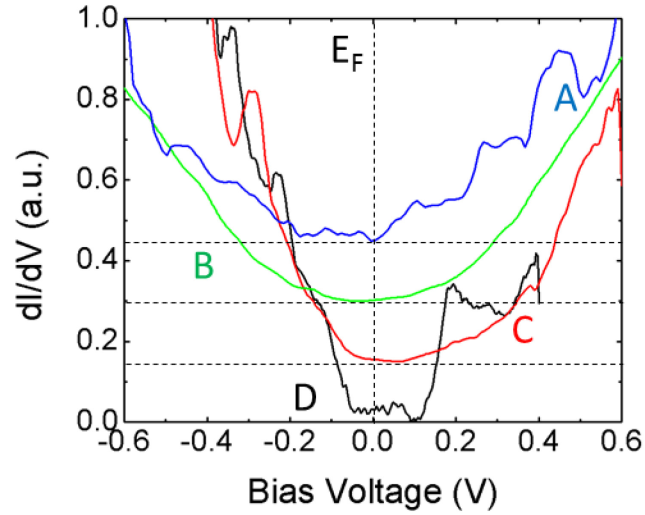


Figure 6.2: dI/dV as a function of bias voltage, corresponding to the energy relative to the Fermi level. The value of the bulk band gap is between 0.19-0.21 ± 0.10 eV, consistent with previous studies. The Fermi level is tuned across the gap, with an n-p transition occurring from composition B (x = 0.58) to composition C (x = 0.64).

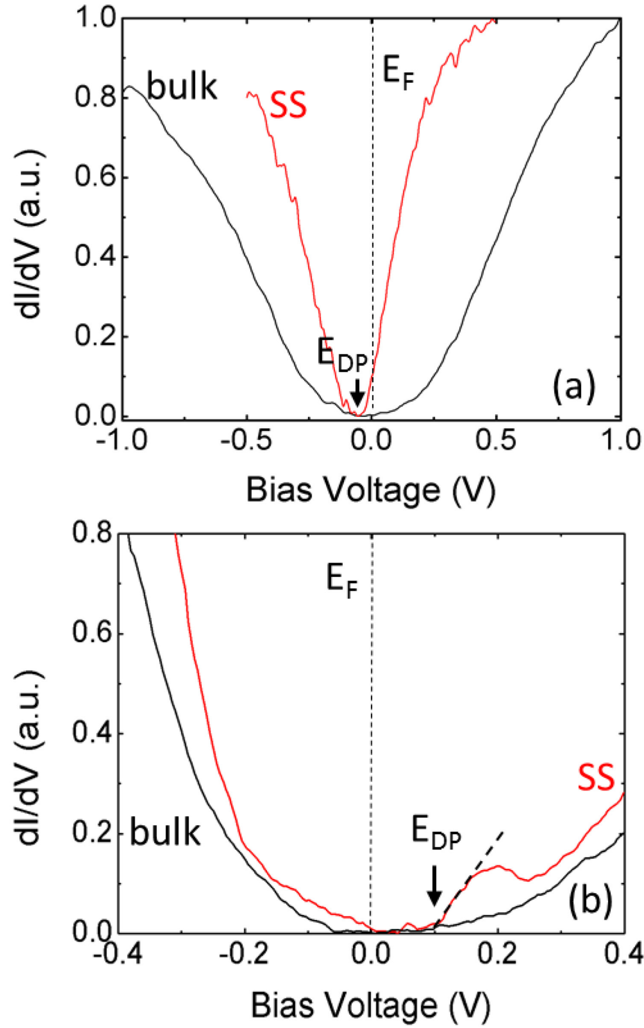


Figure 6.3: dI/dV of samples (a) B and (b) C as a function of bias voltage, corresponding to the energy relative to the Fermi level, $E_F$, revealing two distinct states of surface and bulk conduction. The bulk conduction (black) reveals an effective band gap of 0.20 (0.21) ± 0.10 eV for sample B (C). The surface state curves (red) were taken with a lower tunneling impedance, with the Dirac point, $E_D$, located between $E_F$ and the valence band edge for sample B ($x = 0.58$) and near the conduction band edge for sample C ($x = 0.64$).

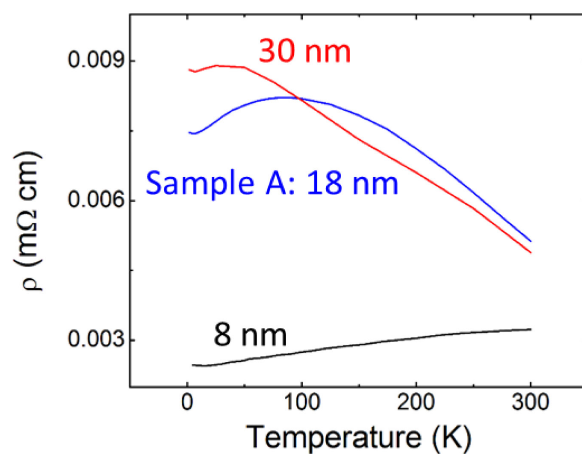


Figure 6.4: Resistivity vs. temperature for sample A (18 nm, blue), a sample similar to B (30 nm, red), and an 8 nm film (black). For thin films (8 nm), the resistance increases monotonically as a function of temperature, indicating conductive behavior. For thicker films (>18 nm), the resistivity decreases with temperature, indicating resistive behavior.

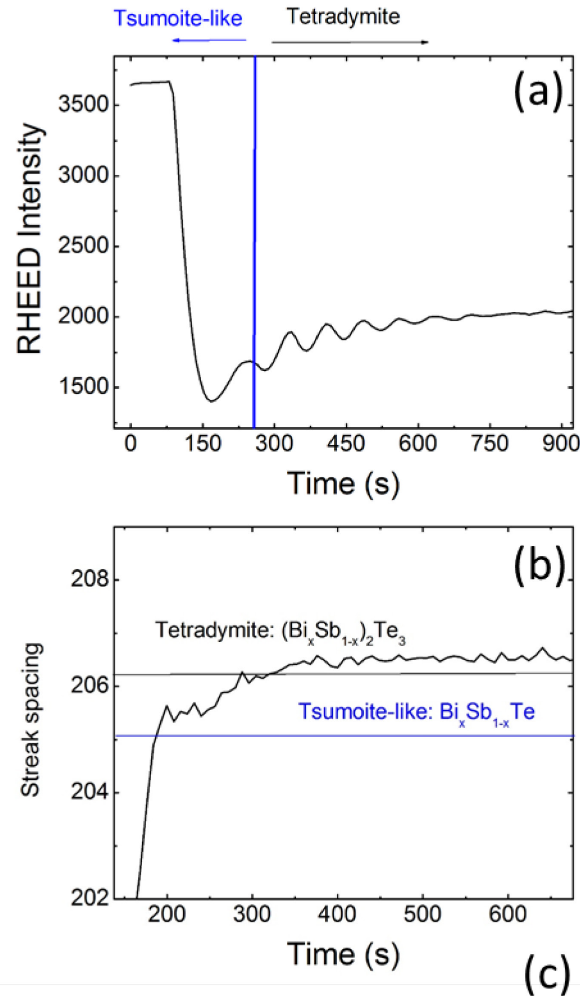


Figure 6.5: (a) RHEED intensity oscillations as a function of time and (b) an analysis of the streak spacing as a function of time. There is an increase in streak spacing around 275 s, corresponding to a decrease in the lattice constant which could indicate the presence of Bi intercalation resulting in a tsuomoite structure, giving way to the standard tetradymide structure later in the growth. (c) Cross-sectional view of the sample with the structure suggested by the electrical resistance and RHEED results. At the substrate/growth layer interface is a conductive layer, followed by an insulating layer of BiSbTe. The red lines indicate the topological surface states.

## 6.8 References

[1] D. West, Y. Y. Sun, H. Wang, J. Bang, and S.B. Zhang, *Phys. Rev. B* **86**, 121201(R) (2012).

[2] J. Zhang, C. Z. Chang, Z. Zhang, J. Wen, X. Feng, K. Li, M. Liu, K. He, L. Wang, X. Chen, Q.K. Xue, X. Ma, and Y. Wang, *Nat. Commun.* **2**, 574 (2011).

[3] X. He, H. Li, L. Chen, and K. Wu, *Sci. Rep*. **5**, 8830 (2015).

[4] C. Chen, S. He, H. Weng, W. Zhang, L. Zhao, H. Liu, X. Jia, D. Mou, S. Liu, J. He, Y. Peng, Y. Feng, Z. Xie, G. Liu, X. Dong, J. Zhang, X. Wang, Q. Peng, Z. Wang, S. Zhang, F. Yang, C. Chen, Z. Xu, X. Dai, Z. Fang, and X.J. Zhou, *Proc. Natl. Acad. Sci. U.S.A.* **109**, 3694 (2012).

[5] Bruker Model TT10 Etched Tungsten STM Probes S/N: 120613

[6] Bruker Model PT10 Cut Platinum/Iridium STM Probes S/N: 101713

[7] B. Lita, thesis, University of Michigan, 2002.

[8] E. S. Zech, A. S. Chang, A. J. Martin, J. C. Canniff, Y. H. Lin, J. M. Millunchick, and R. S. Goldman, *Appl. Phys. Lett.* **103**, 082107 (2013).

[9] Y. Jiang, Y. Y. Sun, M. Chen, Y. Wang, Z. Li, C. Song, K. He, L. Wang, X. Chen, Q.K. Xue, X. Ma, and S.B. Zhang, *Phys. Rev. Lett.* **108**, 066809 (2012).

[10] T. Zhang, J. Ha, N. Levy, Y. Kuk, and J. Stroscio, *Phys. Rev. Lett.* **111**, 056803 (2013).

[11] Y. Jiang, Y.Y. Sun, M. Chen, Y. Wang, Z. Li, C. Song, K. He, L. Wang, X. Chen, Q.K. Xue, X. Ma, and S.B. Zhang, *Phys. Rev. Lett.* **108**, 066809 (2012).

[12] T. Zhang, J. Ha, N. Levy, Y. Kuk, and J. Stroscio, *Phys. Rev. Lett.* **111**, 056803 (2013).

[13] W. Liu, H. Chi, J. C. Walrath, A.S. Chang, V. A. Stoica, L. Endicott, X. Tang, R. S. Goldman, and C. Uher, *Appl. Phys. Lett.* **108**, 043902 (2016).

[14] L. He, X. Kou, M. lang, E.S. Choi, Y. Jiang, T. Nie, W. Jiang, Y. Fan, Y. Wang, F. Xiu, and K.L. Wang, *Sci. Rep.* **3**, 3406 (2013).

[15] Y. Jiang, Y.Y. Sun, M. Chen, Y. Wang, Z. Li, C. Song, K. He, L. Wang, X. Chen, Q.K. Xue, X. Ma, and S.B. Zhang, *Phys. Rev. Lett.* **108**, 066809 (2012).

[16] T. Zhang, J. Ha, N. Levy, Y. Kuk, and J. Stroscio, *Phys. Rev. Lett.* **111**, 056803 (2013).

[17] X. He, H. Li, L. Chen, and K. Wu, *Sci. Rep.* **5**, 8830 (2015).

# Chapter 7

## Summary and Suggestions for Future Work

### 7.1 Summary

Low-dimensional semiconductor structures are important for a wide variety of applications, including thermoelectric generators, laser diodes, photovoltaics, topological spintronic devices, and more. This dissertation presents the investigation of the band structure, local density of states, and local electronic properties of nanostructures ranging from zero-dimensional (0D) quantum dots to two-dimensional (2D) thin films, synthesizing computational and experimental approaches including Poisson-Schrodinger band structure calculations, STM, STS, and SThEM. In the following sections, a brief summary of these results will be presented.

#### 7.1.1 Quantifying the local Seebeck coefficient with nanometer resolution

We demonstrated an approach to quantify the local S using SThEM data in conjunction with a quasi-3D conversion matrix to directly convert the measured temperature gradient-induced voltage profile to an S profile. For a GaAs p-n junction, we assume that V contains contributions from 3 directions parallel and 2 directions perpendicular to the p-n junction interface, with a position-independent conductance. Using the δT(r) method and quasi-3D method to convert $V_{SThEM}$ to $S_{\delta T(r)}$ and $S_{quasi\text{-}3D}$, we

find that $S_{quasi\text{-}3D}$ exhibits better overall agreement with $S_{Comp}$ than $S_{\delta T(r)}$. Since our quasi-3D conversion approach only considers the temperature profile and geometry of the sample, this provides a basic framework for developing a conversion matrix even when details such as the thermal and electrical conductivity profiles of a sample are not well known. Although deconvolutions based on tip geometries are often used to enhance lateral resolution of scanning probe measurements, this deconvolution allows direct conversion of a measured proxy quantity to the quantity of interest. Therefore, this approach could be extended to other techniques such as scanning voltage microscopy and scanning spreading resistance microscopy.

### 7.1.2 Profiling the local carrier concentration across a semiconductor quantum dot

We profiled the local carrier concentration across a uniformly- and degenerately-doped uncapped InAs SK QD grown on GaAs. We converted the local S profile to a local n profile assuming a single parabolic band with literature values for the effective masses. A comparison of the corresponding conduction band-edge profile with Poisson-Schrodinger band-edge simulations revealed a reduced carrier concentration in the QD center in comparison to that of the WL. We further used 3D atom probe tomography to profile the distribution of Si dopants. Preliminary data indicated a higher Si dopant concentration within the QDs than in the surrounding WL, with an increase in the number of dopants in the vicinity of the QD with growth layer. This work is the first measurement of a carrier concentration across a single quantum dot, and this approach can be applied to

a wide range of semiconductor heterostructures, providing key insight necessary for achieving nanostructured semiconductor device design goals.

### 7.1.3 Ordered Horizontal $Sb_2Te_3$ Nanowires Induced by Femtosecond Laser

We have conducted STM/S and SThEM investigations of the composition and band structure of ordered horizontal $Sb_2Te_3$ nanowires induced by femtosecond laser irradiation of a thin film. Initial STM and STS studies revealed a widened band gap in the nanowire region, but SThEM indicated that the thermoelectric voltage of the nanowires remained unchanged from pristine $Sb_2Te_3$. The presence of an insulating material surrounding buried nanowires was confirmed by cross-sectional TEM studies. With subsequent STS studies we directly measured the band gap modulation between the $Sb_2Te_3$ nanowires and insulating material. These horizontal $Sb_2Te_3$ nanowires are promising for a variety of applications, including thermoelectrics and optoelectronics, and the novel fabrication method using fs laser-irradiation in ambient conditions provides a pathway for scalable manufacturing.

### 7.1.4 Identification of topological surface states in $(Bi_{1-x}Sb_x)_2Te_3$ alloy films

STM and STS of $(Bi_{1-x}Sb_x)_2Te_3$ alloys were used to reveal both the Fermi level and Dirac point located inside the bulk bandgap, indicating bulk-like insulating behavior with accessible surface states. Additionally, we discuss the alloy composition and film thickness dependence of the band structure and transport properties, showing evidence for

a conductive interface layer beneath the insulating bulk. Thus, while alloying can be used to achieve tunable surface states, the film/substrate interface needs to be carefully considered to achieve an insulating bulk. Prior to this work, direct detection of topological surface states in BiSbTe systems has been achieved only for $T < 10$ K. However, for device applications, room-temperature identification of topological surface states is needed. This work demonstrates the first direct measurement of topological surface states using STS at room temperature for any material.

### 7.2 Suggestions for Future Work

Suggestions for future work, including preliminary data, are presented in the following sections. These projects include SThEM investigations the uniformity of the composition, grain sizes, and electronic and thermoelectric properties of $Mg_2Si_{1-x}Sn_x$ thermoelectric devices; STM and STS investigations of the strain-dependent band gap in nanostructured graphene; and SThEM investigations of the local electronic properties of quantum dots.

#### 7.2.1 Investigating the composition of bulk thermoelectrics using SThEM

Bulk thermoelectric materials such as chalcogenides, half-Heusler compounds, and skutterudites provide a promising route to high-efficiency thermoelectric devices which can be manufactured on a large scale.[1-3] However, these materials are typically polycrystalline and are often inhomogeneous, especially on microscopic length scales.

With SThEM, the thermoelectric voltage can be probed on a nanometer to micron scale to elucidate inhomogeneity in the thermopower, thermal conductivity, or dopant distribution. Preliminary investigations have been conducted on a skutterudite sample of Sn-doped $CoSb_3$ synthesized by Mr. S. Hui in the groups of Profs. Uher and Pipe at the University of Michigan.[4] Figure 7.1 (a) shows an STM topography image of a polished bulk skutterudite sample. The sample was reasonably flat over a range of μm¸ with Δz for this image ≈ 13 nm. $V_{SThEM}$ was measured across the dotted white line, and the results are plotted in Fig. 7.1(b). The SThEM measurement reveals a large variation of the $V_{SThEM}$, varying up to 33% from the mean, with a maximum variation of a factor of 6 across the sample, indicating significant inhomogeneity.

The Uher group has recently acquired a spark plasma sintering (SPS) system for manufacturing bulk thermoelectrics. Their combustion synthesis will be used to prepare powders of $Mg_2Si_{1-x}Sn_x$,[5] and the SPS system will be employed to fabricate fully dense thermoelectric materials, including the electrical contacts needed for device fabrication. SThEM investigations will be used to provide key feedback to the SPS materials synthesis process regarding the uniformity of the composition, grain sizes, and electronic and thermoelectric properties. Figure 7.2 illustrates a possible experimental procedure for this investigation. An ingot produced using SPS (top) will be sliced into disks. Each disk will be probed with SThEM (bottom), providing a map of the uniformity of SPS thermoelectric materials from a nanometer to millimeter scale. Once the processing conditions are optimized, SThEM will be used to demonstrate the uniformity of both n- and p-type $Mg_2Si_{1-x}Sn_x$ materials for thermoelectric devices.

### 7.2.2 Strain-induced band gap opening in nanostructured graphene

Strained graphene nanostructures offer a route to controllable band gap engineering in graphene. Li et al. from the laboratory of Prof. Gary Cheng at Purdue University have demonstrated a method for scalable straining of graphene using laser shock-induced 3D shaping of graphene.[6] Using this method, Prof. Cheng's group manufactured nano-trenches of chemical-vapor-deposition (CVD) grown graphene on a $SiO_2$ mold. In the vicinity of the graphene nano-trenches, molecular dynamics simulations of the laser shock straining suggest that the strain is higher at the trench edges than in the regions between the trenches. Therefore, to examine the influence of strain on the local electronic structure of the graphene nano-trenches, we utilize STS. At various locations designated on the sample diagram in Fig. 7.3(a), we measure the dI/dV as a function of bias voltage, as shown in Fig. 7.3(b). For the unpatterned graphene on $SiO_2$ (black solid line), the conductance vs. bias voltage exhibits a "V" shape, without a discernable bandgap. However, at the edge of the trench (red dashed line) and in the region between trenches (blue dash-dot line), negligible conductance in the vicinity of zero bias voltage is observed, suggesting an opening of the bandgap. In Fig. 7.3(c) and (d), an STM image of graphene strained on a cylindrical trench mold with 400 nm width and 50 nm depth and corresponding effective band gaps as a function of position across the trench are shown. The highest effective bandgaps, 1.3 ± 0.38 eV and 1.7 ± 0.24 eV, are observed at the edges of the trench, marked with the dashed lines. On the other hand, smaller bandgaps, ranging from 0.55 ± 0.14 eV to 1.15 ± 0.14 eV, are observed between the trenches and in regions far away from the trenches. Thus, both the strain and bandgap appear to be maximized at the trench edges. We are currently

investigating the band gap opening of graphene nanostructures grown and laser-shocked on Cu foil.

### 7.2.3 Investigating the local electronic properties of quantum dots using SThEM

In Chapter 4, SThEM is used to profile the carrier concentration across a single quantum dot. This technique allows carrier concentration measurements with unprecedented resolution and opens up many avenues of exploration. In particular, SThEM can be used to investigate the effect of growth methods and conditions on the band structure of QDs. Furthermore, the same procedure used for profiling the conduction band of the Stranski-Krastanov (SK) quantum dots in Chapter 4 could be applied to droplet epitaxy (DE) or solid phase epitaxy quantum dots instead.[7] DE quantum dots are expected to have a significantly different strain profile from SK dots, and thus the band structure is expected to differ from that of SK dots. Therefore, SThEM would provide a nanometer-resolution tool for investigating a variety of effects, including strain and dislocations as well as dopant inhomogeneity. For QDs grown by the same method, the effect of size and density on the band profile or carrier concentration profile can be examined. Furthermore, a similar approach could be applied more broadly to other nanostructures. SThEM is uniquely able to probe across individual nanostructures, such as single nanowires. For cases where it is difficult to determine a relation to convert $V_{SThEM}$ to a carrier concentration, significant insights about the band structure and electronic properties can be determined from S.

To compliment the information on the electronic properties obtained using STS and SThEM, including conduction band profile and carrier concentration profile, APT can be

used to provide information about the 3D atomic structure, including the location of individual dopants, as in Chapter 4. With APT, differences in dopant incorporation as a function of growth methods and techniques, including for DE vs SK QDs can be investigated and correlated with the SThEM results. Together, APT and SThEM (and STS) provide a powerful combination of techniques which allows atomic to nanoscale investigations of doping mechanisms and the relationship between dopant incorporation and the band structure, including the mechanisms by which dopants are incorporated into nanostructures and electrically activated.

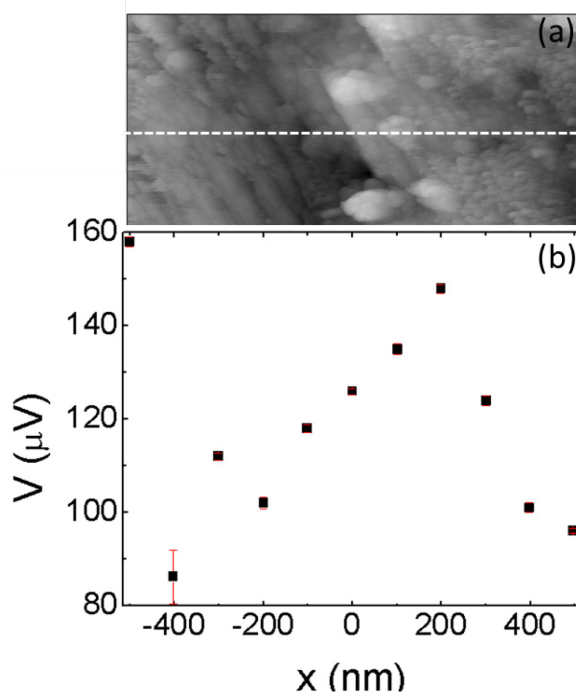


Figure 7.1: (a) STM topography image of a polished bulk skutterudite sample. The sample was reasonably flat over a range of μm¸ with $\Delta z$ for this image ≈ 13 nm. (b) $V_{SThEM}$ as a function of position, measured across the dotted white line in (a). The SThEM measurement reveals a large variation of the $V_{SThEM}$, varying up to 33% from the mean, with a maximum variation of a factor of 6 across the sample, indicating significant inhomogeneity.

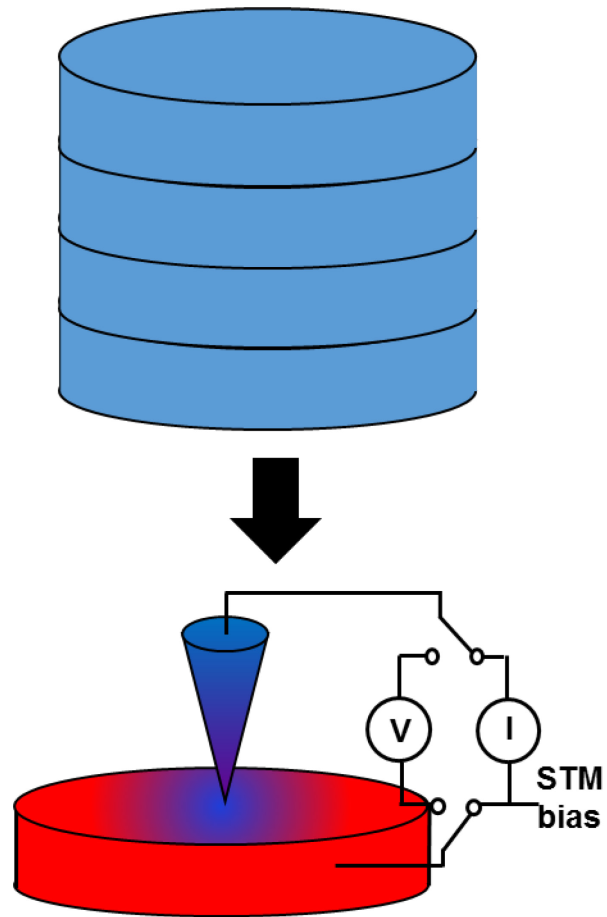


Figure 7.2: An ingot produced using SPS (top) will be sliced into disks. Each disk will be probed with SThEM (bottom), providing a map of the uniformity of SPS thermoelectric materials from a nanometer to millimeter scale.

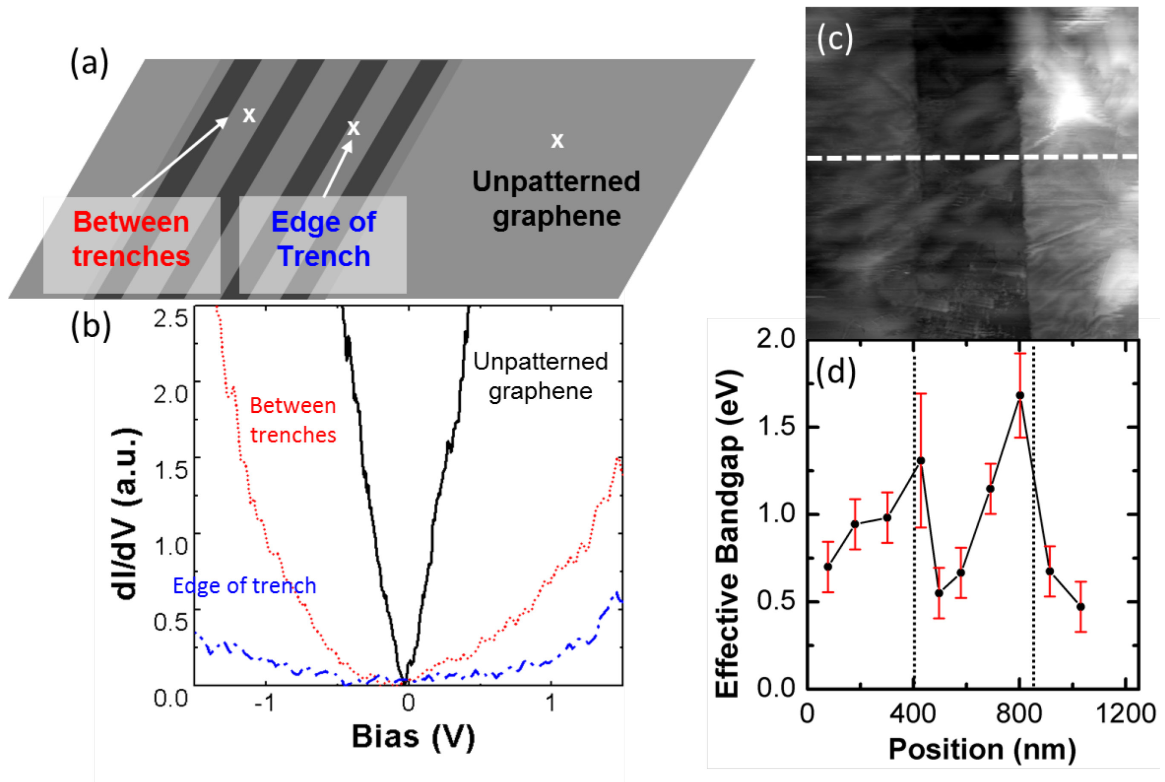


Figure 7.3: (a) Schematic of the graphene nano-trench sample (b) Representative dI/dV measurements on the unpatterned graphene, at the edge of a trench, and in the area between trenches. The unpatterned graphene has no distinguishable bandgap, while the edge of the trench has a significantly larger bandgap than the area between trenches, presumably due to differing levels of strain. (c) STM image of a nano-trench and (d) the corresponding effective bandgaps as a function of position. The highest bandgaps are observed at the trench edges, presumably due to their high strain which maximizes the bandgap opening.

## 7.3 References

[1] G. S. Nolas, J. Poon, and M. Kanatzidis, *MRS Bulletin* **31**, 199 (2006).

[2] X. Shi, J. Yang, J. R. Salvador, M. Chi, J. Y. Cho, H. Wang, S. Bai, J. Yang, W. Zhang, and L. Chen, *J. Am. Chem. Soc.* **133**,7837 (2011).

[3] M. Rull-Bravo, A. Moure, J. F. Fernandez, and M. Martin-Gonzalez, *RSC Adv.* **5**, 41653 (2015).

[4] S. Hui, M. D. Nielsen, M. R. Homer, D. L. Medlin, J. Tobola, J. R. Salvador, J. P. Heremans, K. P. Pipe, and C. Uher, *J. Appl. Phys.* **115**, 103704 (2014).

[5] W. Liu, H. Chi, H. Sun, Q. Zhang, K. Yin, X. Tang, Q. Zhang, and C. Uher, *Phys. Chem. Chem. Phys.* **16**, 6893 (2014).

[6] J. Li, T.F. Chung, Y.P. Chen, and G.J. Cheng, *Nano Lett.* **12**, 4577 (2012).

[7] S. Huang, S. J. Kim, R. Levy, X. Q. Pan, and R. S. Goldman, *Appl. Phys. Lett.* **103**, 132104 (2013).

## Appendix A

## Scanning tunneling spectroscopy data analysis

In this appendix, the analysis procedures for the STS spectra to determine the effective band gaps are described. The band gaps are determined using extrapolation of the linear onsets of the band edges, based on the work by R. Timm et al.[1] The analysis steps are outlined below, followed by the Matlab code and graphical interface used for the analysis, written by Dr. A.S. Chang and edited by the author.

### A.1 Band gap analysis procedure

First, the data are smoothed using the "smooth" algorithm in Matlab, which employs adjacent-averaging.[2] A smoothing constant is chosen such that the values are averaged over an energy less than or ~ $k_bT$. The data are then normalized to a range of 0 to 1 and plotted in a graphical user interface (GUI). The user defines ranges for the conductance and valence bands for which linear least-squares fits are performed. The band edges are defined at the intercept of these linear fits and dI/dV = 0. An example of the GUI applied to an STS spectra is shown in Fig. A.1,

The energy resolution of the STS measurement is determined using an approximation of the full width of half maximum δE,

$$\delta E \approx \sqrt{(3.3 \times k_B T)^2 + (1.8 \times eV_{mod})^2} \qquad \text{(A.1)}$$

where T is temperature, $k_B$ is Boltzmann's constant, e is the elementary charge, and $V_{mod}$ is the modulation voltage applied to the bias during the STS measurement.[3] For a modulation voltage of 30 mV at room temperature, $\delta E \approx 0.1$ eV.

### A.2 Band gap analysis code

```
function [] = normalization_code_2_subtraction_updated_slope_narrow_bandgap()
%9/9/15 version c ASC found and JCW fixed one bug:
    %if voltage sweeps from positive to negative, code won't work. Have
    %added if statement that flips v if this is the case and displays
    %warning text-- conduction band and valence will be switched. Working
    %on better solution.

%    1/15/2016 JCW modified to output processed v didv as text file with
%    name 'out + STS filename'
clear

close all

%*************Nota Bene****************111
%Changes made in this section need to be repeated in the section that updates the plot

list = dir('*.txt');
n = length(list);
input_text = [ 'Please input the value for i (from 1 to ',num2str(n),') = '];
global i;
i = input(input_text);

%for i = 1:(n/2);
%import the voltage values and the I(V) and dI/dV readings
aux = importdata(list(i).name);

%Save the variables in vectors
v = aux.data(:,1);
didv = (1*aux.data(:,2));

if v(1)>0
```

```
    v=-aux.data(:,1);
    display('Warning: Bias voltage has been inverted')
 end

%Obtain the number of smoothing processes from the user (use odd number)
smooth_constant = 11;


for j=1:10
   didv(1)=[];
   v(1)=[];
end
for j=length(didv)-10:length(didv)
   didv(length(didv))=[];
   v(length(v))=[];
end


%Smooth the dI/dV values
didv = smooth(didv, smooth_constant);

%Calculate the offset of the dI/dV curve from zero.
offset = min(didv);
didv = didv - offset;
didv = didv / max(didv);
% GUI Part

%save v and didv to text file with automatic name
%A = [v didv];

s=strcat('out',list(i).name);
fileID = fopen(s,'w');
fprintf(fileID,'%6s %12s\r\n','v','didv');
fprintf(fileID, '%f %f \n', [v didv]');
%fprintf(fileID,'%6.2f %12.8f\r\n',A);
fclose(fileID);



%   Creates the figure
S.fh = figure('units','pixels',...
              'position',[10 10 1150 650],...
              'menubar','none',...
              'name','STS band edge calc',...
              'numbertitle','off',...
              'resize','off');
```

```
%   Creates borders around slider sets
%   Must be done before other code in order to keep these in background
S.b1 = uicontrol('style','edit',...
              'unit', 'pix',...
              'enable', 'inactive',...
              'position', [10 10 580 200],...
              'backgroundc', get(S.fh,'color'));

S.b3 = uicontrol('style','edit',...
              'unit', 'pix',...
              'enable', 'inactive',...
              'position', [10 220 580 200],...
              'backgroundc', get(S.fh,'color'));

S.b4 = uicontrol('style','edit',...
              'unit', 'pix',...
              'enable', 'inactive',...
              'position', [10 430 580 200],...
              'backgroundc', get(S.fh,'color'));


%   Sets axes object
S.ax = axes('units','pixels',...
          'position',[650 50 480 520]);


%   Sets text boxes above states properties
S.Conductance = uicontrol('style','text',...
               'unit','pix',...
               'position',[20 180 300 20],...
               'fontsize',13,...
               'BackgroundColor',[.8 .8 .8],...
               'string','conduction band edge');
S.Valence = uicontrol('style','text',...
               'unit','pix',...
               'position',[20 390 300 20],...
               'fontsize',13,...
               'BackgroundColor',[.8 .8 .8],...
               'string','Valence band edge');
S.Zoom = uicontrol('style','text',...
               'unit','pix',...
               'position',[20 600 300 20],...
               'fontsize',13,...
               'BackgroundColor',[.8 .8 .8],...
               'string','Zoom in / out of graph');
```

```
%   Code to save picture of the plot
S.FMT = {[],'jpg','png','bmp'};  % List of file formats.


% Now we create a menu for the figure itself.
S.fm = uimenu(S.fh,'label','Save Plot As');
S.fm(2) = uimenu(S.fm(1),'label','jpg');
S.fm(3) = uimenu(S.fm(1),'label','png');
S.fm(4) = uimenu(S.fm(1),'label','bmp');
set(S.fm(2:4),'callback',{@fm_call})  % To save the drawing.

%   Left edge of conduction band
S.sl = uicontrol('style','slide',...
            'unit','pix',...
            'position',[60 60 180 20],...
            'min',-1,'max',1,'val',-1);
S.ed(1) = uicontrol('style','edit',...
              'unit','pix',...
              'position',[20 60 40 20],...
              'fontsize',10,...
              'string','-1');    % Displays the min.
S.ed(2) = uicontrol('style','edit',...
              'unit','pix',...
              'position',[95 90 100 20],...
              'fontsize',10,...
              'string','-1');  % Displays the value.
S.ed(3) = uicontrol('style','edit',...
              'unit','pix',...
              'position',[240 60 40 20],...
              'fontsize',10,...
              'string','1');     % Displays the max.
S.tex = uicontrol('style','text',...
             'unit','pix',...
             'position',[30 120 250 40],...
             'fontsize',10,...
             'BackgroundColor',[.8 .8 .8],...
             'string','Minimum value of conduction band');

%   Right edge of conduction band
S.sl2 = uicontrol('style','slide',...
            'unit','pix',...
            'position',[350 60 180 20],...
            'min',-1,'max',1,'val',1);
S.ed2(1) = uicontrol('style','edit',...
              'unit','pix',...
```

```
                'position',[310 60 40 20],...
                'fontsize',10,...
                'string','-1');   % Displays the min.
S.ed2(2) = uicontrol('style','edit',...
                'unit','pix',...
                'position',[385 90 100 20],...
                'fontsize',10,...
                'string','1');  % Displays the value.
S.ed2(3) = uicontrol('style','edit',...
                'unit','pix',...
                'position',[530 60 40 20],...
                'fontsize',10,...
                'string','1');    % Displays the max.
S.tex2 = uicontrol('style','text',...
               'unit','pix',...
               'position',[320 120 250 40],...
               'fontsize',10,...
               'BackgroundColor',[.8 .8 .8],...
               'string','Maximum value of conduction band');

%   Left edge of Valence band
S.sl3 = uicontrol('style','slide',...
              'unit','pix',...
              'position',[60 270 180 20],...
              'min',-1,'max',1,'val',-1);
S.ed3(1) = uicontrol('style','edit',...
                'unit','pix',...
                'position',[20 270 40 20],...
                'fontsize',10,...
                'string','-1');   % Displays the min.
S.ed3(2) = uicontrol('style','edit',...
                'unit','pix',...
                'position',[95 300 100 20],...
                'fontsize',10,...
                'string','-1');  % Displays the value.
S.ed3(3) = uicontrol('style','edit',...
                'unit','pix',...
                'position',[240 270 40 20],...
                'fontsize',10,...
                'string','1');    % Displays the max.
S.tex3 = uicontrol('style','text',...
               'unit','pix',...
               'position',[30 320 250 40],...
               'fontsize',10,...
               'BackgroundColor',[.8 .8 .8],...
               'string','Minimum value of valence band');
```

```
%   Right edge of valence band
S.sl4 = uicontrol('style','slide',...
                'unit','pix',...
                'position',[350 270 180 20],...
                'min',-1,'max',1,'val',1);
S.ed4(1) = uicontrol('style','edit',...
                  'unit','pix',...
                  'position',[310 270 40 20],...
                  'fontsize',10,...
                  'string','-1');   % Displays the min.
S.ed4(2) = uicontrol('style','edit',...
                  'unit','pix',...
                  'position',[385 300 100 20],...
                  'fontsize',10,...
                  'string','1');  % Displays the value.
S.ed4(3) = uicontrol('style','edit',...
                  'unit','pix',...
                  'position',[530 270 40 20],...
                  'fontsize',10,...
                  'string','1');    % Displays the max.
S.tex4 = uicontrol('style','text',...
                 'unit','pix',...
                 'position',[320 320 250 40],...
                 'fontsize',10,...
                 'BackgroundColor',[.8 .8 .8],...
                 'string','Maximum value of valence band');



%   Minimum value of the graph
S.sl5 = uicontrol('style','slide',...
                'unit','pix',...
                'position',[60 470 180 20],...
                'min',-1,'max',1,'val',-1);
S.ed5(1) = uicontrol('style','edit',...
                  'unit','pix',...
                  'position',[20 470 40 20],...
                  'fontsize',10,...
                  'string','-1');   % Displays the min.
S.ed5(2) = uicontrol('style','edit',...
                  'unit','pix',...
                  'position',[95 500 100 20],...
                  'fontsize',10,...
```

```
                 'string','-1');  % Displays the value.
S.ed5(3) = uicontrol('style','edit',...
                 'unit','pix',...
                 'position',[240 470 40 20],...
                 'fontsize',10,...
                 'string','1');    % Displays the max.
S.tex5 = uicontrol('style','text',...
               'unit','pix',...
               'position',[30 520 250 40],...
               'fontsize',10,...
               'BackgroundColor',[.8 .8 .8],...
               'string','Minimum value of graph');



%   Maximum value of the graph
S.sl6 = uicontrol('style','slide',...
              'unit','pix',...
              'position',[350 470 180 20],...
              'min',-1,'max',1,'val',1);
S.ed6(1) = uicontrol('style','edit',...
                 'unit','pix',...
                 'position',[310 470 40 20],...
                 'fontsize',10,...
                 'string','-1');   % Displays the min.
S.ed6(2) = uicontrol('style','edit',...
                 'unit','pix',...
                 'position',[385 500 100 20],...
                 'fontsize',10,...
                 'string','1');  % Displays the value.
S.ed6(3) = uicontrol('style','edit',...
                 'unit','pix',...
                 'position',[530 470 40 20],...
                 'fontsize',10,...
                 'string','1');    % Displays the max.
S.tex6 = uicontrol('style','text',...
               'unit','pix',...
               'position',[320 520 250 40],...
               'fontsize',10,...
               'BackgroundColor',[.8 .8 .8],...
               'string','Maximum value of graph');

%   Display the calculated band gap
S.ed9 = uicontrol('style','edit',...
                 'unit','pix',...
                 'position',[660 580 100 20],...
```

```
            'fontsize',10,...
            'string','100');  % Displays the value.
S.tex9 = uicontrol('style','text',...
           'unit','pix',...
           'position',[560 580 100 30],...
           'fontsize',10,...
           'BackgroundColor',[.8 .8 .8],...
           'string','Calculated bandgap');

% Display the file name
S.text10 = uicontrol('style','text',...
           'unit','pix',...
           'position',[800 620 250 30],...
           'fontsize',10,...
           'BackgroundColor',[.8 .8 .8],...
           'string',list(i).name);
%   Display the calculated valence edge
S.ed11 = uicontrol('style','edit',...
            'unit','pix',...
            'position',[855 580 100 20],...
            'fontsize',10,...
            'string','N/A');  % Displays the value.
S.tex11 = uicontrol('style','text',...
           'unit','pix',...
           'position',[770 580 80 20],...
           'fontsize',10,...
           'BackgroundColor',[.8 .8 .8],...
           'string','valence edge');
%   Display the calculated conduction edge
S.ed12 = uicontrol('style','edit',...
            'unit','pix',...
            'position',[1045 580 100 20],...
            'fontsize',10,...
            'string','N/A');  % Displays the value.
S.tex12 = uicontrol('style','text',...
           'unit','pix',...
           'position',[960 580 90 30],...
           'fontsize',10,...
           'BackgroundColor',[.8 .8 .8],...
           'string','conduction edge');

%   Display the calculated valence edge
S.ed13 = uicontrol('style','edit',...
            'unit','pix',...
            'position',[855 600 100 20],...
            'fontsize',10,...
```

```
                 'string','N/A');  % Displays the value.
S.tex13 = uicontrol('style','text',...
               'unit','pix',...
               'position',[770 600 80 20],...
               'fontsize',10,...
               'BackgroundColor',[.8 .8 .8],...
               'string','valence slope');
%   Display the calculated conduction edge
S.ed14 = uicontrol('style','edit',...
                 'unit','pix',...
                 'position',[1045 600 100 20],...
                 'fontsize',10,...
                 'string','N/A');  % Displays the value.
S.tex14 = uicontrol('style','text',...
               'unit','pix',...
               'position',[960 600 90 30],...
               'fontsize',10,...
               'BackgroundColor',[.8 .8 .8],...
               'string','conduction slope');


%   Display the calculated band gap
S.ed15 = uicontrol('style','edit',...
                 'unit','pix',...
                 'position',[660 600 100 20],...
                 'fontsize',10,...
                 'string','100');  % Displays the value.
S.tex15 = uicontrol('style','text',...
               'unit','pix',...
               'position',[560 600 100 30],...
               'fontsize',10,...
               'BackgroundColor',[.8 .8 .8],...
               'string','flat stdv');



 % END SLIDER DEFINTIONS


%   Gets values from sliders
S.plot1 = get(S.sl,{'min','value','max'});
S.plot2 = get(S.sl2,{'min','value','max'});
S.plot3 = get(S.sl3,{'min','value','max'});
S.plot4 = get(S.sl4,{'min','value','max'});
S.plot5 = get(S.sl5,{'min','value','max'});
S.plot6 = get(S.sl6,{'min','value','max'});
```

```
n_min_temp = [];
n_max_temp = [];
%Get the range for the plot
n_min_temp = [];
n_max_temp = [];

for j = 1: length(v)
    if S.plot5{2} < v(j)
        n_min_temp = [n_min_temp, j];
    end
end
n_min = min(n_min_temp);

for j = length(v):-1:1
    if S.plot6{2} > v(j)
        n_max_temp = [n_max_temp, j];
    end
end
n_max = max(n_max_temp);

plot(v(n_min:n_max),didv(n_min:n_max),'k')
datacursormode on

set(gca,'unit','pix','position',[650 50 480 520]);
grid on

%title(['smoothconstant=',smooth_constant,';',list(2*i,1).name]);
xlabel('Applied bias (V)')
ylabel('dI/dV (arb. unit)')

hold on;

%Get the range for linear fitting for the valence band
for j = 1: length(v)
    if S.plot3{2} < v(j)
        n_valence_min = j;
        break
    end
end

for j = length(v):-1:1
    if S.plot4{2} > v(j)
        n_valence_max = j;
        break
    end
```

```
end


%Get the range for linear fitting for the valence band
for j = 1: length(v)
    if S.plot1{2} < v(j)
        n_conduction_min = j;
        break
    end
end

for j = length(v):-1:1
    if S.plot2{2} > v(j)
        n_conduction_max = j;
        break
    end
end

fit_valence =
polyfit(v(n_valence_min:n_valence_max),didv(n_valence_min:n_valence_max),1);
v_fit = v*fit_valence(1) + fit_valence(2);
n_valence_end = length(v);
for j = 1: length(v_fit)
    if 0 > v_fit(j)
        n_valence_end = j;
        break
    end
end
plot(v(n_valence_min:n_valence_end), v_fit(n_valence_min:n_valence_end));

fit_conduction =
polyfit(v(n_conduction_min:n_conduction_max),didv(n_conduction_min:n_conduction_
max),1);
v_fit = v*fit_conduction(1) + fit_conduction(2);
n_conduction_end = 1;
for j = length(v_fit):-1:1
    if 0 > v_fit(j)
        n_conduction_end = j;
        break
    end
end
plot(v(n_conduction_end:n_conduction_max),
v_fit(n_conduction_end:n_conduction_max));

%Get the range for flat region
```

```
n_flat_min=n_valence_end;
n_flat_max=n_conduction_end;

numb_zero = length(v(n_flat_min:n_flat_max));
didv_0 = [];
for k = 1:numb_zero
    didv_0 = [didv_0; 0];
end
fit_flat = polyfit(v(n_flat_min:n_flat_max),didv_0,1);
%fit_flat = polyfit(v(n_flat_min:n_flat_max),didv(n_flat_min:n_flat_max),1);

plot(v(n_min:n_max), v(n_min:n_max)*fit_flat(1) + fit_flat(2),'r');



hold off

%   Updates plot after slider change
set([S.ed(:);S.sl],'call',{@sl_call,S});          % Shared Callback.
set([S.ed2(:);S.sl2],'call',{@sl_call2,S});       % Shared Callback.
set([S.ed3(:);S.sl3],'call',{@sl_call3,S});       % Shared Callback.
set([S.ed4(:);S.sl4],'call',{@sl_call4,S});       % Shared Callback.
set([S.ed5(:);S.sl5],'call',{@sl_call5,S});       % Shared Callback.
set([S.ed6(:);S.sl6],'call',{@sl_call6,S});       % Shared Callback.
%set([S.ed7(:);S.sl7],'call',{@sl_call7,S});      % Shared Callback.
%set([S.ed8(:);S.sl8],'call',{@sl_call8,S});      % Shared Callback.


%   Callback function for saving plot picture
function [] = fm_call(varargin)
    % Callback for the figure menu.
        N = inputdlg('Enter a file name.','FileName'); % Get a name.
        F = getframe(S.fh,get(S.ax,'OuterPosition') + [80 30 -190 30]);  % Only want to get
axes.
        FMT = S.FMT{varargin{1}==S.fm};  % User's format choice.
        imwrite(F.cdata,[N{1},'.',FMT],FMT)  % Write the image.
end

end


%   Each of these functions update the plot after changing
%   slider values
function [] = sl_call(varargin)
    % Callback for the edit box and slider.
    [h,S] = varargin{[1,3]};  % Get calling handle and structure.
```

```
    SL = get(S.sl,{'min','value','max'});  % Get the slider's info.
    E = str2double(get(h,'string'));  % Numerical edit string.

    switch h  % Who called?
        case S.ed(1)
            if E <= SL{2}
                set(S.sl,'min',E)  % E is less than current value.
                Updateplot(S)
            elseif E < SL{3}
                set(S.sl,'val',E,'min',E) % E is less than max value.
                set(S.ed(2),'string',E) % Set the current display.
                Updateplot(S)
            else
                set(h,'string',SL{1}) % Reset the value.
                Updateplot(S)
            end
        case S.ed(2)
            if E >= SL{1} && E <= SL{3}
                set(S.sl,'value',E)  % E falls within range of slider.
                Updateplot(S)
            else
                set(h,'string',SL{2}) % User tried to set slider out of range.
                Updateplot(S)
            end
        case S.ed(3)
            if E >= SL{2}
                set(S.sl,'max',E)  % E is less than current value.
                Updateplot(S)
            elseif E > SL{1}
                set(S.sl,'val',E,'max',E) % E is less than max value.
                set(S.ed(2),'string',E) % Set the current display.
                Updateplot(S)
            else
                set(h,'string',SL{3}) % Reset the value.
                Updateplot(S)
            end
        case S.sl
            set(S.ed(2),'string',SL{2}) % Set edit to current slider
            Updateplot(S)
        otherwise
            % Do nothing
    end
end

function [] = sl_call2(varargin)
    % Callback for the edit box and slider.
```

```
    [h,S] = varargin{[1,3]};  % Get calling handle and structure.
    SL = get(S.sl2,{'min','value','max'});  % Get the slider's info.
    E = str2double(get(h,'string'));  % Numerical edit string.


    switch h  % Who called?
        case S.ed2(1)
            if E <= SL{2}
                set(S.sl2,'min',E)  % E is less than current value.
                Updateplot(S)
            elseif E < SL{3}
                set(S.sl2,'val',E,'min',E) % E is less than max value.
                set(S.ed2(2),'string',E) % Set the current display.
                Updateplot(S)
            else
                set(h,'string',SL{1}) % Reset the value.
                Updateplot(S)
            end
        case S.ed2(2)
            if E >= SL{1} && E <= SL{3}
                set(S.sl2,'value',E)  % E falls within range of slider.
                Updateplot(S)
            else
                set(h,'string',SL{2}) % User tried to set slider out of range.
                Updateplot(S)
            end

        case S.ed2(3)
            if E >= SL{2}
                set(S.sl2,'max',E)  % E is less than current value.
                Updateplot(S)
            elseif E > SL{1}
                set(S.sl2,'val',E,'max',E) % E is less than max value.
                set(S.ed2(2),'string',E) % Set the current display.
                Updateplot(S)
            else
                set(h,'string',SL{3}) % Reset the value.
                Updateplot(S)
            end
        case S.sl2
            set(S.ed2(2),'string',SL{2}) % Set edit to current slider
        Updateplot(S)
        otherwise
            % Do nothing
    end
end
```

```
function [] = sl_call3(varargin)
   % Callback for the edit box and slider.
   [h,S] = varargin{[1,3]};  % Get calling handle and structure.
   SL = get(S.sl3,{'min','value','max'});  % Get the slider's info.
   E = str2double(get(h,'string'));  % Numerical edit string.

   switch h  % Who called?
      case S.ed3(1)
         if E <= SL{2}
            set(S.sl3,'min',E)  % E is less than current value.
            Updateplot(S)
         elseif E < SL{3}
            set(S.sl3,'val',E,'min',E) % E is less than max value.
            set(S.ed3(2),'string',E) % Set the current display.
            Updateplot(S)
         else
            set(h,'string',SL{1}) % Reset the value.
            Updateplot(S)
         end
      case S.ed3(2)
         if E >= SL{1} && E <= SL{3}
            set(S.sl3,'value',E)  % E falls within range of slider.
         else
            set(h,'string',SL{2}) % User tried to set slider out of range.
         end
      case S.ed3(3)
         if E >= SL{2}
            set(S.sl3,'max',E)  % E is less than current value.
            Updateplot(S)
         elseif E > SL{1}
            set(S.sl3,'val',E,'max',E) % E is less than max value.
            set(S.ed3(2),'string',E) % Set the current display.
            Updateplot(S)
         else
            set(h,'string',SL{3}) % Reset the value.
            Updateplot(S)
         end
      case S.sl3
         set(S.ed3(2),'string',SL{2}) % Set edit to current slider.
         Updateplot(S)
      otherwise
         % Do nothing
   end
end
```

```
function [] = sl_call4(varargin)
   % Callback for the edit box and slider.
   [h,S] = varargin{[1,3]};  % Get calling handle and structure.
   SL = get(S.sl4,{'min','value','max'});  % Get the slider's info.
   E = str2double(get(h,'string'));  % Numerical edit string.

   switch h  % Who called?
      case S.ed4(1)
         if E <= SL{2}
            set(S.sl4,'min',E)  % E is less than current value.
            Updateplot(S)
         elseif E < SL{3}
            set(S.sl4,'val',E,'min',E) % E is less than max value.
            set(S.ed4(2),'string',E) % Set the current display.
            Updateplot(S)
         else
            set(h,'string',SL{1}) % Reset the value.
            Updateplot(S)
         end
      case S.ed4(2)
         if E >= SL{1} && E <= SL{3}
            set(S.sl4,'value',E)  % E falls within range of slider.
            Updateplot(S)
         else
            set(h,'string',SL{2}) % User tried to set slider out of range.
            Updateplot(S)
         end
      case S.ed4(3)
         if E >= SL{2}
            set(S.sl4,'max',E)  % E is less than current value.
            Updateplot(S)
         elseif E > SL{1}
            set(S.sl4,'val',E,'max',E) % E is less than max value.
            set(S.ed4(2),'string',E) % Set the current display.
            Updateplot(S)
         else
            set(h,'string',SL{3}) % Reset the value.
            Updateplot(S)
         end
      case S.sl4
         set(S.ed4(2),'string',SL{2}) % Set edit to current slider.
         Updateplot(S)
      otherwise
         % Do nothing
   end
end
```

```
function [] = sl_call5(varargin)
   % Callback for the edit box and slider.
   [h,S] = varargin{[1,3]};  % Get calling handle and structure.
   SL = get(S.sl5,{'min','value','max'});  % Get the slider's info.
   E = str2double(get(h,'string'));  % Numerical edit string.

   switch h  % Who called?
      case S.ed5(1)
         if E <= SL{2}
            set(S.sl5,'min',E)  % E is less than current value.
            Updateplot(S)
         elseif E < SL{3}
            set(S.sl5,'val',E,'min',E) % E is less than max value.
            set(S.ed5(2),'string',E) % Set the current display.
            Updateplot(S)
         else
            set(h,'string',SL{1}) % Reset the value.
            Updateplot(S)
         end
      case S.ed5(2)
         if E >= SL{1} && E <= SL{3}
            set(S.sl5,'value',E)  % E falls within range of slider.
            Updateplot(S)
         else
            set(h,'string',SL{2}) % User tried to set slider out of range.
            Updateplot(S)
         end
      case S.ed5(3)
         if E >= SL{2}
            set(S.sl5,'max',E)  % E is less than current value.
            Updateplot(S)
         elseif E > SL{1}
            set(S.sl5,'val',E,'max',E) % E is less than max value.
            Updateplot(S)
            set(S.ed5(2),'string',E) % Set the current display.
            Updateplot(S)
         else
            set(h,'string',SL{3}) % Reset the value.
            Updateplot(S)
         end
      case S.sl5
         set(S.ed5(2),'string',SL{2}) % Set edit to current slider.
         Updateplot(S)
      otherwise
         % Do nothing
```

```
    end
end

function [] = sl_call6(varargin)
    % Callback for the edit box and slider.
    [h,S] = varargin{[1,3]};  % Get calling handle and structure.
    SL = get(S.sl6,{'min','value','max'});  % Get the slider's info.
    E = str2double(get(h,'string'));  % Numerical edit string.

    switch h  % Who called?
        case S.ed6(1)
            if E <= SL{2}
                set(S.sl6,'min',E)  % E is less than current value.
                Updateplot(S)
            elseif E < SL{3}
                set(S.sl6,'val',E,'min',E) % E is less than max value.
                set(S.ed6(2),'string',E) % Set the current display.
                Updateplot(S)
            else
                set(h,'string',SL{1}) % Reset the value.
                Updateplot(S)
            end
        case S.ed6(2)
            if E >= SL{1} && E <= SL{3}
                set(S.sl6,'value',E)  % E falls within range of slider.
                Updateplot(S)
            else
                set(h,'string',SL{2}) % User tried to set slider out of range.
                Updateplot(S)
            end
        case S.ed6(3)
            if E >= SL{2}
                set(S.sl6,'max',E)  % E is less than current value.
                Updateplot(S)
            elseif E > SL{1}
                set(S.sl6,'val',E*.9,'max',E) % E is less than max value.
                set(S.ed6(2),'string',E) % Set the current display.
                Updateplot(S)
            else
                set(h,'string',SL{3}) % Reset the value.
                Updateplot(S)
            end
        case S.sl6
            set(S.ed6(2),'string',SL{2}) % Set edit to current slider.
            Updateplot(S)
        otherwise
```

```
            % Do nothing
    end
end

%   Base function to update the plot as sliders change
function[] = Updateplot(varargin)
    [S] = varargin{[1]};
    global i;
    S.plot1 = get(S.sl,{'min','value','max'});
    S.plot2 = get(S.sl2,{'min','value','max'});
    S.plot3 = get(S.sl3,{'min','value','max'});
    S.plot4 = get(S.sl4,{'min','value','max'});
    S.plot5 = get(S.sl5,{'min','value','max'});
    S.plot6 = get(S.sl6,{'min','value','max'});


list = dir('*.txt');
n = length(list);
%i = input('Please input the value for i=  ');


%import the voltage values and the dI/dV readings
aux = importdata(list(i).name);

%Save the variables in vectors
v = aux.data(:,1);
didv = (1*aux.data(:,2));
 if v(1)>0
     v=-aux.data(:,1);
     display('Warning: Bias voltage has been inverted')
 end

for j=1:10
    didv(1)=[];
    v(1)=[];
end
for j=length(didv)-10:length(didv)
    didv(length(didv))=[];
    v(length(v))=[];
end

%Obtain the number of smoothing processes from the user (use odd number)
smooth_constant = 11;

%Smooth the dI/dV values
didv = smooth(didv, smooth_constant);
```

```
%Calculate the offset of the dI/dV curve from zero.
offset = min(didv);
didv = didv - offset;
didv = didv / max(didv);

%Get the range for the plot
n_min_temp = [];
n_max_temp = [];
%Get the range for the plot
for j = 1: length(v)
    if S.plot5{2} < v(j)
        n_min_temp = [n_min_temp, j];
    end
end
n_min = n_min_temp(1);

for j = length(v):-1:1
    if S.plot6{2} > v(j)
        n_max_temp = [n_max_temp, j];
    end
end
n_max = max(n_max_temp);


plot(v(n_min:n_max),didv(n_min:n_max),'k')
datacursormode on

set(gca,'unit','pix','position',[650 50 480 520]);
grid on

%title(['smoothconstant=',smooth_constant,';',list(2*i,1).name]);
xlabel('Applied bias (V)')
ylabel('dI/dV (a.u.)')

hold on;

%Get the range for linear fitting for the valence band
for j = 1: length(v)
    if S.plot3{2} < v(j)
        n_valence_min = j;
        break
    end
end

for j = length(v):-1:1
```

```
    if S.plot4{2} > v(j)
        n_valence_max = j;
        break
    end
end

%Get the range for linear fitting for the valence band
for j = 1: length(v)
    if S.plot1{2} < v(j)
        n_conduction_min = j;
        break
    end
end

for j = length(v):-1:1
    if S.plot2{2} > v(j)
        n_conduction_max = j;
        break
    end
end

fit_valence =
polyfit(v(n_valence_min:n_valence_max),didv(n_valence_min:n_valence_max),1);
v_fit = v*fit_valence(1) + fit_valence(2);
n_valence_end = length(v);
for j = 1: length(v_fit)
    if 0 > v_fit(j)
        n_valence_end = j;
        break
    end
end
plot(v(n_valence_min:n_valence_end), v_fit(n_valence_min:n_valence_end));

fit_conduction =
polyfit(v(n_conduction_min:n_conduction_max),didv(n_conduction_min:n_conduction_
max),1);
v_fit = v*fit_conduction(1) + fit_conduction(2);
n_conduction_end = 1;
for j = length(v_fit):-1:1
    if 0 > v_fit(j)
        n_conduction_end = j;
        break
    end
end
plot(v(n_conduction_end:n_conduction_max),
v_fit(n_conduction_end:n_conduction_max));
```

```
%Get the range for flat region

n_flat_min = n_valence_end;
n_flat_max= n_conduction_end;

numb_zero = length(v(n_flat_min:n_flat_max));
didv_0 = [];
for k = 1:numb_zero
    didv_0 = [didv_0; 0];
end
fit_flat = polyfit(v(n_flat_min:n_flat_max),didv_0,1);
%fit_flat = polyfit(v(n_flat_min:n_flat_max),didv(n_flat_min:n_flat_max),1);


plot(v(n_min:n_max), v(n_min:n_max)*fit_flat(1) + fit_flat(2),'r');
stdv_flat_region = std(didv(n_flat_min:n_flat_max),1);

%%%%%%%%%%%%%%%%%%%%%%%%%%
bandgap = 'N/A';
E_valence = (fit_flat(2) - fit_valence(2))/(fit_valence(1)-fit_flat(1));
E_conduction = (fit_flat(2) - fit_conduction(2))/(fit_conduction(1) - fit_flat(1));
E_bandgap = E_conduction - E_valence;
if abs(E_bandgap) < 5
    bandgap = num2str(E_bandgap);
else
    bandgap = 'N/A';
end

E_valence_text = 'N/A';
if abs(E_valence)< 5
    E_valence_text = num2str(E_valence);
else
    E_valence_text = 'N/A';
end

E_conduction_text = 'N/A';
if abs(E_conduction) < 5
    E_conduction_text = num2str(E_conduction);
else
    E_conduction_text = 'N/A';
end

set(S.ed11, 'string', E_valence_text);
set(S.ed12, 'string', E_conduction_text);
set(S.ed13, 'string', num2str(fit_valence(1)));
```

```
set(S.ed14, 'string', num2str(fit_conduction(1)));
set(S.ed15, 'string', num2str(stdv_flat_region));

set(S.ed9, 'string', bandgap)

E_valence_text = 'N/A';
if abs(E_valence) <5
    E_valence_text = num2str(E_valence);
else
    E_valence_text = 'N/A';
end

E_conduction_text = 'N/A';
if abs(E_conduction) <5
    E_conduction_text = num2str(E_conduction);
else
    E_conduction_text = 'N/A';
end
hold off
end
```

*Published with MATLAB® R2015b*

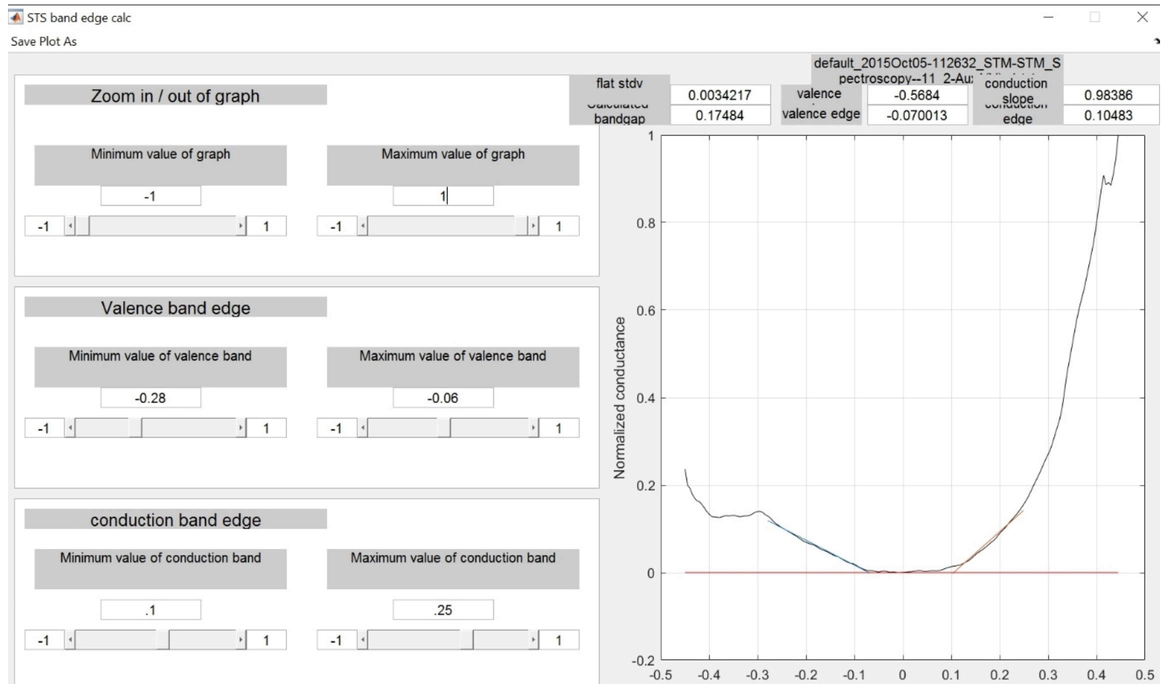


Figure A.1: Graphical user interface for the STS band gap calculation code. The user defines the linear regions of the valence and conductance band edges.

# Appendix B

## 1D Fourier model and f-factor

In this appendix, we present a 1D Fourier model of heat transfer in SThEM used to calculate the f-factor as a function of tip geometry and sample and tip thermal conductivity.

### B.1 f-factor definition

When the STM tip makes contact with the heated sample, the tip cools the sample, but the sample also heats the tip. Therefore, not all of the total temperature drop ($T_{Sample}$-$T_{Tip}$) contributes to $V_{SThEM}$. Thus, $V_{SThEM}$ is related to S according to

$$V_{SThEM} = f \times (T_{Sample} - T_{Tip}) \times S \qquad \text{(B.1)}$$

where $T_{Tip}$ and $T_{Sample}$ are the temperatures of the room-temperature tip and the heated sample, S is the Seebeck coefficient profile, and f is the fraction of the temperature drop that contributes to the thermoelectric voltage in the sample. The f-factor was first defined by Dr. H.K. Lyeo and observed to depend on the "bluntness" of the tip and the thermal conductivities of the tip and sample. [4] Here, we quantify the f-factor more precisely.

## B.2 1D Fourier model

Using the Fourier equation for heat transfer, we assume Q is constant and represent the SThEM system as a series of thermal resistances, shown in Figure B.1. There is a thermal resistance and temperature drop in the sample, the tip, and the tip-sample contact. Since Q is constant, it follows that

$$Q = \frac{1}{R}\Delta T = \frac{T_{Sample} - T_{Tip}}{R_{Sample} + R_{Contact} + R_{Tip}} = \frac{T_{Sample} - T_{C-sample}}{R_{Sample}} \qquad \text{(B.2)}$$

where $T_{Sample}$, $T_{Tip}$, $T_{C\text{-}Sample}$, and $T_{C\text{-}tip}$ denote the temperature in the sample, tip, or at the tip-sample contact point on the sample side or tip side, respectively, and $R_{Sample}$, $R_{Tip}$, $R_{Contact}$ denote the thermal resistance across the sample, tip, and tip-sample contact, respectively.

## B.3 f-factor calculation

The f-factor is the fraction of the total temperature drop that contributes to the thermoelectric voltage and thus is equal to

$$f = \frac{T_{Sample} - T_{C-sample}}{T_{Sample} - T_{Tip}} = \frac{R_{Sample}}{R_{Sample} + R_{Contact} + R_{Tip}} \qquad \text{(B.3)}$$

Assuming the tip-sample thermal resistance is negligible,[4] Eq. B.3 simplifies to

$$f = \frac{1}{1 + {R_{Tip}}/{R_{Sample}}} \qquad \text{(B.4)}$$

Then, $R_{Tip}$ and $R_{Sample}$ are calculated by integrating their thermal conductivities:

$$R_{Sample} = \int_{r_{Contact}}^{r} \frac{dr'}{2\pi r'^2 \kappa_{Sample}} = \frac{1}{2\pi\kappa_{Sample}} [\frac{1}{r_{Contact}} - \frac{1}{r}] \quad (B.5)$$

$$R_{Tip} = \int_{r_{Contact}}^{r_{Tip}} \frac{dr'}{\pi r'^2 \kappa_{Tip} tan \, ^{\theta_{Tip}}/_{2}}$$
$$= \frac{1}{\pi \kappa_{Tip} tan \, ^{\theta_{Tip}}/_{2}} [\frac{1}{r_{Contact}} - \frac{1}{r_{Tip}}] \quad (B.6)$$

Where r is position, κ is thermal conductivity, and $\theta_{Tip}$ is the angle of the tip, defined in Fig. B.1. Assuming that r, the distance from the tip, and $r_{Tip}$, the radius of the tip far from the contact point are much larger than $r_{Contact}$, the size of the tip-sample contact point, then

$$R_{Sample} = \frac{1}{2\pi\kappa_{Sample} r_{Contact}} \quad (B.7)$$

$$R_{Tip} = \frac{1}{\pi\kappa_{Tip} tan \, ^{\theta_{Tip}}/_{2} \, r_{Contact}} \quad (B.8)$$

Finally, f is represented in terms of the thermal conductivities and tip angle as[5,6]

$$f = \frac{1}{1 + {R_{Tip}}/{R_{Sample}}} = \frac{\kappa_{tip} tan \, ^{\theta_{Tip}}/_{2}}{\kappa_{tip} tan \, ^{\theta_{Tip}}/_{2} + 2\kappa_{sample}} \quad (B.9)$$

Figure B.2 shows f plotted as a function of θ for a tungsten tip, $\kappa_W$=173 W/mK, and samples with κ ranging from $\kappa_{GaAs}$= 55 W/mK to $\kappa_{BiTe}$=1.7 W/mK. f increases with the ratio of $\kappa_{Tip}/\kappa_{Sample}$ and with the tip angle $\theta_{Tip}$. The values of the f factor calculated using Eq. B.9 and measured for GaAs and $Sb_2Te_3$ samples of known S are marked with blue and red x's, respectively. The calculated and measured values of $f_{GaAs}$ agree well, but there is nearly a factor of 2 discrepancy between the calculated and measured values of $f_{SbTe}$. Thus, the simple model presented here is reasonably reliable for III-V semiconductors but not for V-VI layered semiconductors, such as $Bi_2Te_3$, $Sb_2Te_3$, and related compounds.

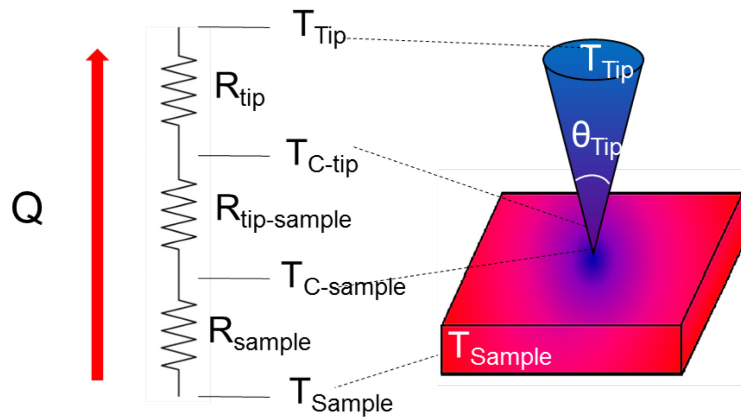


Figure B.1: Thermal model of SThEM. Assuming Q is constant, we model the sample as a series of thermal resistances and temperatures. There is a thermal resistance and temperature drop in the sample, the tip, and the tip-sample contact.

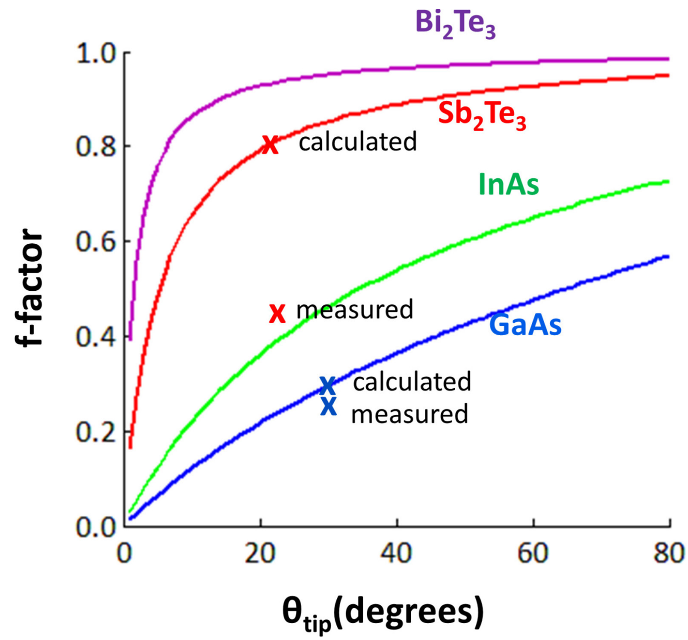


Figure B.2: f as a function of θ for a tungsten tip, $\kappa_W$=173 W/mK, and samples of thermal conductivities ranging from $\kappa_{GaAs}$= 55 W/mK to $\kappa_{BiTe}$=1.7W/mK. f increases with the ratio of $\kappa_{Tip}/\kappa_{Sample}$ and with the tip angle $\theta_{Tip}$. The values of the f factor calculated using Eq. B.9 and measured for GaAs and $Sb_2Te_3$ samples of known S are marked with blue and red x's, respectively. The calculated and measured values of $f_{GaAs}$ agree well, but there is nearly a factor of 2 discrepancy between the calculated and measured values of $f_{SbTe}$.

# Appendix C

## Materials Parameters

This appendix lists a variety of materials parameters used in this dissertation. Table C.1 contains values for the thermal conductivities (κ) of the tip and samples used to calculate the f-factor as well as the bulk band gap values at 300 K used for comparison with the effective bandgaps measured by STS.[7-11] Table C.2 and Table C.3 contain the materials parameters used for the software "1D Poisson"[12] used for the 1D Poisson-Schrodinger calculations in Sections 3.5 and 4.7 and Appendix H. The parameters for the binaries InAs and GaAs in Table C.2 are unaltered from the default materials file that comes with the software. The author constructed a section for the ternary alloy $In_xGa_{1-x}As$ using the parameters listed in the electronic archive compiled by the Ioffe Physico-Technical Institute.[13] The ternary parameters presented in Table C.3 follow the form $parameter\ value = constant + (linear)x + (quadratic)x^2$, where x is the In fraction. The documentation for the materials file structure can be found in the download package for "1D Poisson" which is available on the website of Prof. Gregory Snider.[14]

| | κ (W/mK) | Band gap (eV) |
|---|---|---|
| GaAs | 55 | 1.42 |
| InAs | 27 | 0.36 |
| $Sb_2Te_3$ | 4 | 0.22 |
| $Bi_2Te_3$ | 1.7 | 0.15 |
| W (tip) | 173 | N/A |

Table C.1: κ of the tip and samples used to calculate the f-factor and the bulk band gap values at 300 K used for comparison with the effective bandgaps measured by STS.

| | GaAs | InAs |
|---|---|---|
| Energy gap (eV) | +0.142E+01 | +3.720E-01 |
| Band offset (eV) | +0.000E+00 | -6.490E-01 |
| Rel. dielectric constant | +0.131E+02 | +1.450E+01 |
| electron effective mass ($m_e$) | +0.670E-01 | +2.300E-02 |
| conduction band valley degeneracy (eV) | +0.100E+01 | +1.000E+00 |
| heavy hole effective mass ($m_e$) | +0.480E+00 | +4.000E-01 |
| light hole effective mass ($m_e$) | +0.820E-01 | +8.000E-02 |
| donor ionization energy (eV) | +0.600E-02 | +1.500E+00 |
| acceptor ionization (eV) | +0.300E-01 | +5.000E-02 |
| deep donor ionization (eV) | +0.600E+00 | +5.000E-02 |
| deep acceptor ionization (eV) | +0.700E+00 | +1.000E-01 |
| donor concentration ($cm^{-3}$) | +0.000E+00 | +0.000E+00 |
| acceptor concentration ($cm^{-3}$) | +0.000E+00 | +0.000E+00 |
| deep donor concentration ($cm^{-3}$) | +0.000E+00 | +0.000E+00 |
| deep acceptor concentration ($cm^{-3}$) | +0.000E+00 | +0.000E+00 |
| electron mobility ($cm^2/Vs$) | +0.850E+04 | +1.000E+04 |
| hole mobility ($cm^2/Vs$) | +0.400E+03 | +5.000E+02 |

| electron lifetime (s) | +0.100E-11 | +1.000E-10 |
|---|---|---|
| hole lifetime (s) | +0.100E-11 | +1.000E-10 |
| polarization ($C/cm^2$) | +0.000E+00 | +0.000E+00 |

Table C.2: Material parameters of GaAs and used for the 1D Poisson-Schrodinger calculation.

| | constant | linear | quadratic |
|---|---|---|---|
| Energy gap (eV) | 1.42E+00 | -1.49E+00 | 4.30E-01 |
| Band offset (eV) | 0.00E+00 | -6.60E-01 | 1.76E-01 |
| Rel. dielectric constant | 1.29E+01 | 1.53E+00 | 6.70E-01 |
| donor ionization energy (eV) | 3.00E-03 | 4.30E-03 | 4.00E-03 |
| acceptor ionization (eV) | 3.00E-03 | 0.00E+00 | 0.00E+00 |
| deep donor ionization (eV) | 5.00E-01 | 0.00E+00 | 0.00E+00 |
| deep acceptor ionization (eV) | 5.00E-01 | 0.00E+00 | 0.00E+00 |
| electron effective mass ($m_e$) | 6.70E-02 | -4.40E-02 | 0.00E+00 |
| conduction band valley degeneracy (eV) | 1.00E+00 | 0.00E+00 | 0.00E+00 |
| heavy hole effective mass ($m_e$) | 7.60E-01 | -2.50E-01 | 0.00E+00 |
| light hole effective mass ($m_e$) | 1.50E-01 | -6.80E-02 | 0.00E+00 |
| electron mobility ($cm^2/Vs$) | 4.00E+03 | 0.00E+00 | 0.00E+00 |
| hole mobility ($cm^2/Vs$) | 4.00E+02 | 0.00E+00 | 0.00E+00 |
| electron lifetime (s) | 1.00E-10 | 0.00E+00 | 0.00E+00 |
| hole lifetime (s) | 1.00E-10 | 0.00E+00 | 0.00E+00 |
| absorption coefficient ($cm^{-1}$) | 0.00E+00 | 0.00E+00 | 0.00E+00 |
| polarization ($C/cm^2$) | 0.00E+00 | 0.00E+00 | 0.00E+00 |

Table C.3: Material parameters of ternary $In_xGa_{1-x}As$ and used for the 1D Poisson-Schrodinger calculation. The ternary parameters follow the form $parameter\ value = constant + (linear)x + (quadratic)x^2$.

## Appendix D

## SThEM modifications

In this appendix, we provide details of the modifications to the Park STM to enable SThEM. Figure D.1 presents a detailed overview of these modifications, both inside and outside the UHV chamber.

The modified sample plate contains a heater and Si diode to monitor the temperature. The electrical connections for these components are made to the base of the sample plate holder using pogo pins. Another Si diode can be mounted on the tip holder to monitor the temperature at the base of the tip. The heater and diodes are connected to a temperature controller and heater power supply external to the chamber through a newly installed 10 pin military connector, labeled “10 pin SThEM” in Fig. D.1.

The tunneling current and sample bias are disconnected using relays external to the chamber in a breakout box, shown in detail in Fig. D.2. Then these connections are joined together to measure the thermoelectric voltage between the tip and sample, $V_{SThEM}$, as shown in both Figs. D.1 and D.2.

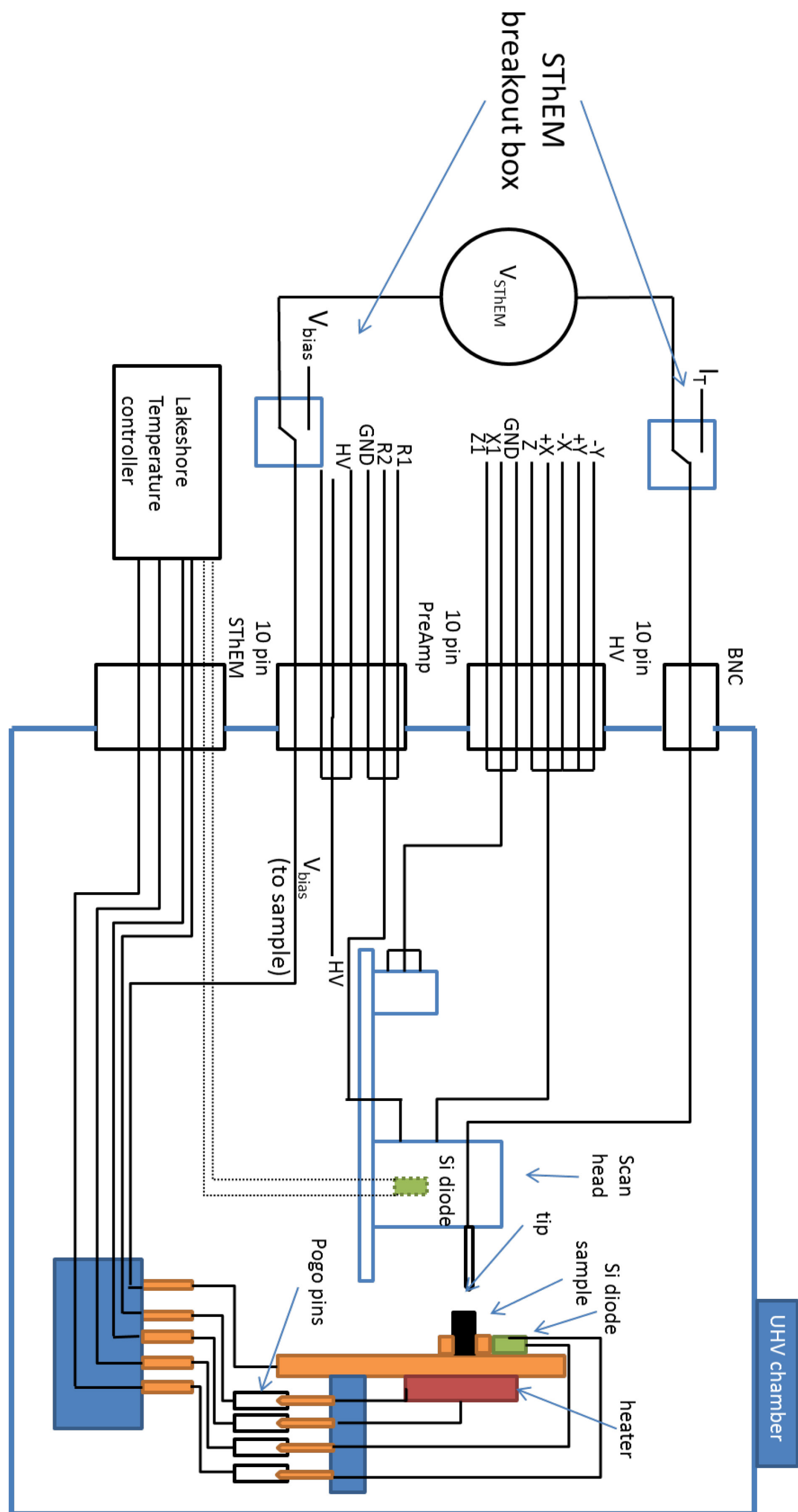


Figure D.1: Overview of STM and SThEM electronics in the modified Park Autoprobe VP2.

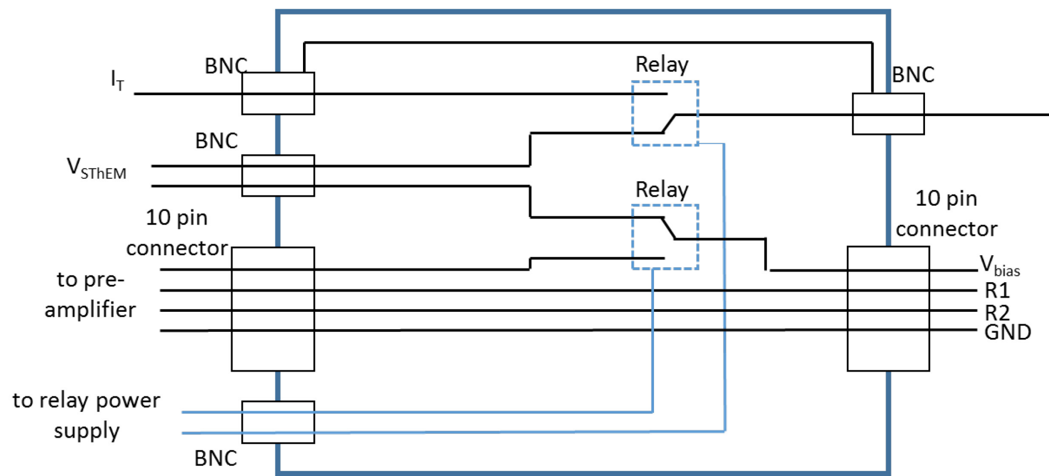


Figure D.2: SThEM breakout box schematic diagram. Two relays disconnect the sample bias and tunneling current to instead measure the thermoelectric voltage, $V_{SThEM}$. The breakout box is connected between the STM and the pre-amplifier externally to the UHV chamber by 10 pin military connectors.

# Appendix E

## Modifications to the RHK SPM controller

When the high voltage power supply in the Park Autoprobe VP2 STM controller failed, many attempts were made to repair the controller by sending it to PSI repair, which specializes in repairing old electronics, but they were unable to make the controller functional once again. The controller was replaced with an SPM100 STM controller from RHK Technology which was intended for use with an Omicron LS-STM, so several adaptations were required to enable use with the Park STM.

First, we ordered custom cables from RHK to connect the SPM 100 to the Park STM. This included a new 2 stage pre-amp, with separate boxes for the I-V converter and amplifier, both external to the UHV chamber and connected through the tunneling current BNC connector. One 10 pin military connector supplies the bias voltage and another supplies the high voltage needed for fine and coarse motion of the tip. However, the cables supplied by RHK only provided a high voltage connection to control the Z coarse motion. To enable X and Y coarse motion, the author modified the cables from RHK to attach two extra BNC connectors. Thus, to switch between X, Y, and Z motion, the coarse motion BNC must be disconnected and switched.

However, when the cables arrived from RHK, the coarse motion of the scan head did not work. After much troubleshooting to pinpoint the problem, the RHK controller was

not outputting a sufficiently high voltage. The author attempted many solutions, including cutting a filter capacitor which limited the output voltage of the coarse motion, but this was not sufficient. To achieve the voltage necessary to control the piezos, a high voltage amplifier HVA 900 was required from RHK Technology which is connected between the SPM 100 and the Park STM high voltage input. When this still did not completely solve the problem, the author took apart the scan head stage and replaced the stage tracks with a duplicate part with less friction, allowing the scan head to move freely. The combined solution of the modified coarse motion cable, HVA 900, and modified scan head allow the RHK SPM 100 to be fully compatible with the Park STM.

The SThEM electronics and breakout box did not require any modifications to work with the RHK controller. The SThEM breakout box is still inserted between the Park STM chamber and the RHK pre-amplifier.

## Appendix F

## SThEM data acquisition

In this appendix, we provide details of the data acquisition program for recording SThEM data. This LabView Virtual Instrument (VI) was developed by Dr. Y.H. Lin to be used with a Keithley 2000 multimeter. The front panel of the VI is shown in Fig. F.1. At the top of the VI, the user can define the STM image number and coordinates of the measurement in X,Y and the tip extension Z. The VI will first measure the voltage, and then switch to measure resistance. The user sets the initial delay times for both the voltage and resistance which will determine how long the program waits before beginning each measurement set. The user also sets the number of voltage and resistance measurements to take and the delay between each measurement point. The program calculates the average and standard deviation of these readings and plots them in the graph on the right of the GUI. When the measurement is completed, a dialog box allows the user to save the data with a custom filename.

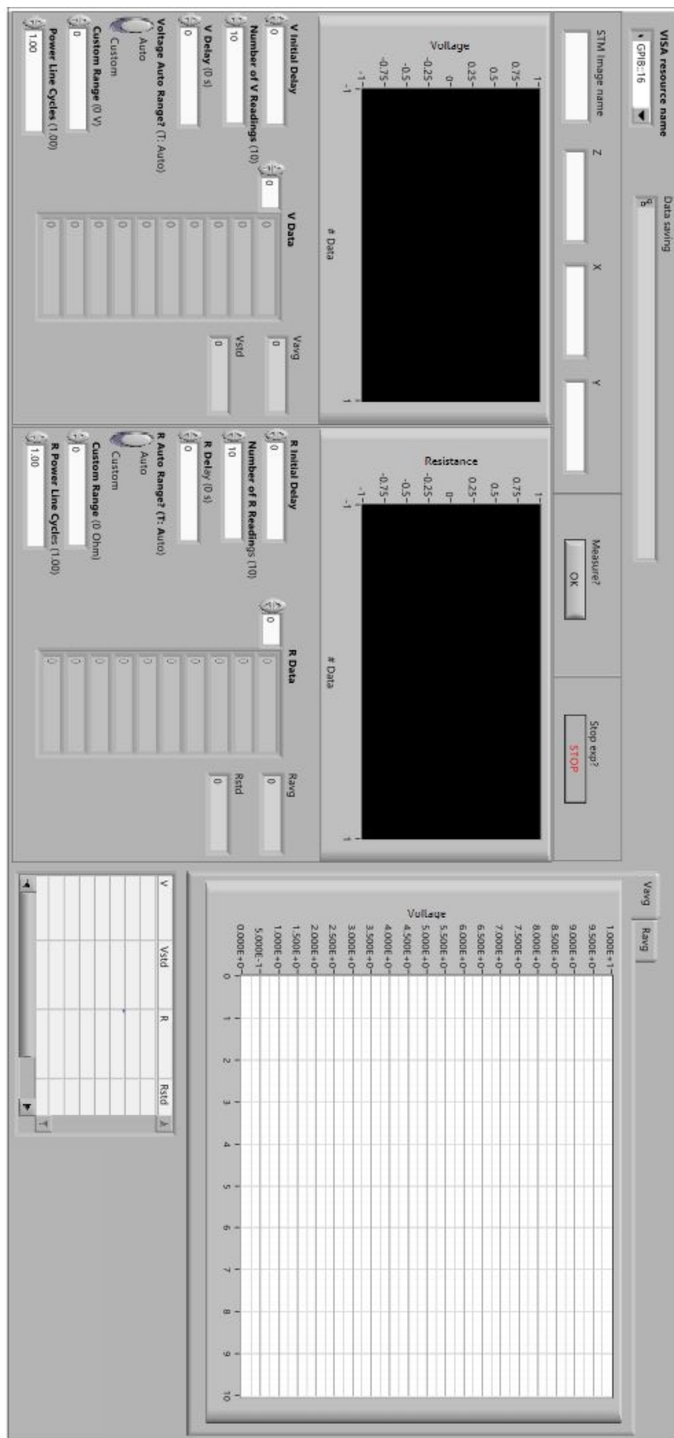


Figure F.1: VI front panel for the SThEM acquisition program. The user sets the delay times before beginning acquisition of the voltage or resistance readings and the number of readings to take. The program calculates the average and standard deviation of these readings and plots them in the graph on the right of the VI.

## Appendix G

## Influence of sample geometry on SThEM measurements

To demonstrate the independence of the thermoelectric voltage from geometry, in Figure G.1 SThEM data for several materials of varying geometry and composition are investigated, including (a) GaAs p-n junction, [15] (b) InAs/GaAs QD[16], (c) In island, and (d) $Sb_2Te_3$ nanotracks.[17,18] For each system, an STM image and line cut across the SThEM trajectory, along with a plot of the normalized $V_{SThEM}$ vs. position, are shown. The SThEM data for (a), (b), and (c) are the same as presented in Chs. 3, 4, and 5 respectively.

The nearly atomically-flat p-n junction presented in Fig. G.1(a) has the largest variation in $V_{SThEM}$. On the left side (n-type) of the p-n junction (x = 0), $V_{SThEM}$ drops to a large negative value at the edge of the depletion zone, and then rapidly rises through zero to a large positive value on the right (p-type) side. Since this measurement was conducted across an atomically-flat cleaved surface, the large variation in $V_{SThEM}$ corresponds directly to the variation in the local Seebeck coefficient and carrier concentration.

$V_{SThEM}$ across the InAs/GaAs QD is plotted in Figure G.1(b), and $V_{SThEM}$ across an In island on GaAs is plotted in Fig. G.1(c). These samples have similar geometry but significantly different composition. However, the total variation in $V_{SThEM}$ across the In island is less than 10%, compared to 30% in the InAs QD. Additionally, while $V_{SThEM}$ is

larger inside the QD than in the wetting layer, the largest $V_{SThEM}$ across the In island is measured far from the island, with the smallest value at the island center.

Finally, the material with the largest variation in surface height is the $Sb_2Te_3$ nanotracks, shown in Fig. G.1(d). $Sb_2Te_3$ nanotracks are formed by irradiating an $Sb_2Te_3$ thin film with a femtosecond laser, forming ridges of an insulating cap covering buried $Sb_2Te_3$ nanowires. VSThEM was measured at three points, two on top of the nanotracks (at x ≈ 200 and 600 nm) and one in the trench between nanotracks (x ≈ 400 nm). Despite the roughest surface ($\Delta z$ = 33 nm), the variation in $V_{SThEM}$ is smaller than all the other samples, roughly 5%. Thus, in all cases, $V_{SThEM}$ corresponds to the electronic properties of the material, rather than the geometry.

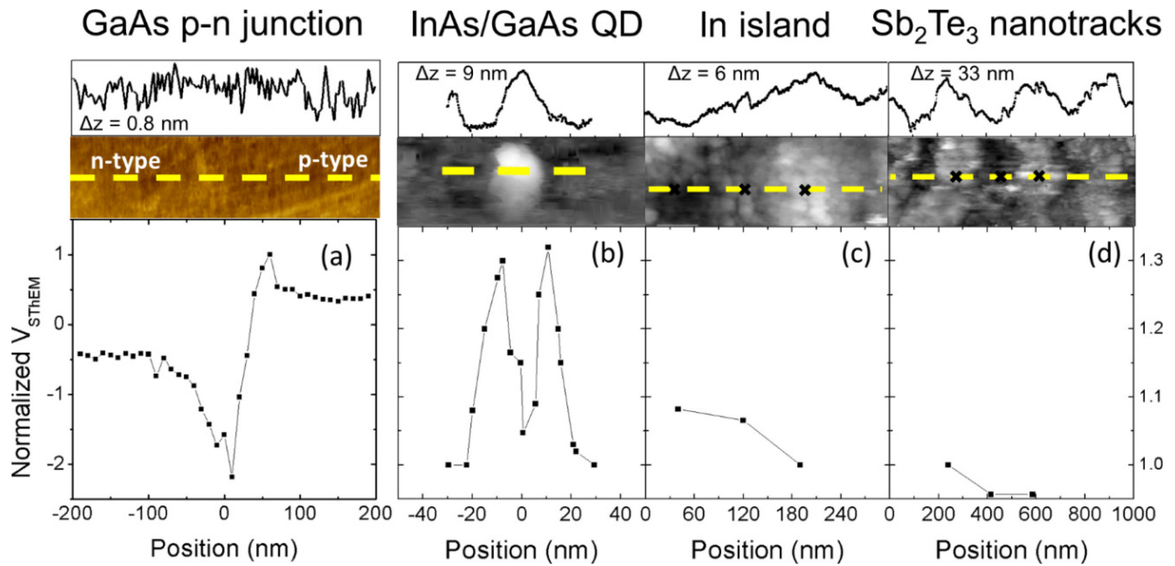


Figure G.1: Plots of normalized $V_{SThEM}$ as a function of position for (a) a GaAs p-n junction, (b) an InAs/GaAs quantum dot, (c) an In island on GaAs, and (d) $Sb_2Te_3$ nanotracks, with the height profile across the SThEM trajectory for each STM image. For all measurements, the corresponding STM image is included with the trajectory noted with a yellow dashed line.

## Appendix H

## Poisson-Schrodinger calculations

This Appendix contains the input files used for the Poisson-Schrodinger calculations used to calculate the carrier concentration profile for the GaAs p-n junction in Section 3.5 and the conduction band profile in Section 4.5. The calculations were conducted using the software "1D Poisson"[19] from Prof. Gregory Snider at the University of Notre Dame.[20]

### H.1 GaAs p-n junction

Below is the input file used to calculate the free carrier concentration profile in Section 3.5.

```
surface slope=0
GaAs t=200 Nd=7.95e16
GaAs t=200 Nd=7.92e16
GaAs t=200 Nd=7.88e16
GaAs t=200 Nd=7.83e16
GaAs t=200 Nd=7.74e16
GaAs t=200 Nd=7.62e16
GaAs t=200 Nd=7.45e16
GaAs t=200 Nd=7.21e16
GaAs t=200 Nd=6.87e16
GaAs t=200 Nd=6.41e16
GaAs t=200 Nd=5.78e16
GaAs t=200 Nd=4.93e16
```

```
GaAs t=200 Nd=3.80e16
GaAs t=200 Nd=2.31e16
GaAs t=200 Nd=3.72e15
GaAs t=200 Na=2.13e16
GaAs t=200 Na=5.33e16
GaAs t=200 Na=9.36e16
GaAs t=200 Na=1.44e17
GaAs t=200 Na=2.06e17
GaAs t=200 Na=2.83e17
GaAs t=200 Na=3.75e17
GaAs t=200 Na=4.85e17
GaAs t=200 Na=6.16e17
GaAs t=200 Na=7.69e17
GaAs t=200 Na=9.46e17
GaAs t=200 Na=1.15e18
GaAs t=200 Na=1.38e18
GaAs t=200 Na=1.64e18
GaAs t=200 Na=1.93e18
substrate

schrodingerstart=50
schrodingerstop=2000
temp=300K
dy=10
```

**H.2 InAs quantum dot**

Below is the input file used to calculate the conduction band structure in Section 4.5.

```
# Quantum well with indium concentration gradient

surface slope=0 v0
InGaAs      t=1000 Nd=6.1E18 x=0.15
InGaAs      t=35 Nd=3.5E18 x=0.2
InGaAs      t=5 Nd=3.5E18 x=0.25
InGaAs      t=7 Nd=3.5E18 x=0.3
InGaAs      t=8 Nd=3.5E18 x=0.35
InGaAs      t=10 Nd=3.5E18 x=0.4
InGaAs      t=15 Nd=3.5E18 x=0.45
InGaAs      t=25 Nd=3.5E18 x=0.5
InGaAs      t=12 Nd=3.5E18 x=0.55
```

```
InGaAs        t=7 Nd=3.5E18 x=0.6
InGaAs        t=9 Nd=3.5E18 x=0.65
InGaAs        t=7 Nd=3.5E18 x=0.6
InGaAs        t=12 Nd=3.5E18 x=0.55
InGaAs        t=25 Nd=3.5E18 x=0.5
InGaAs        t=15 Nd=3.5E18 x=0.45
InGaAs        t=10 Nd=3.5E18 x=0.4
InGaAs        t=8 Nd=3.5E18 x=0.35
InGaAs        t=7 Nd=3.5E18 x=0.3
InGaAs        t=5 Nd=3.5E18 x=0.25
InGaAs        t=35 Nd=3.5E18 x=0.2
InGaAs        t=1000 Nd=6.1E18 x=0.15
substrate

fullyionized
v1 0.0
schrodingerstart=850
schrodingerstop=1350
find quantized states
temp=300K
dy=10
```

## Appendix I

## Quasi-3D deconvolution

This Appendix presents the Matlab code used for the quasi-3D deconvolution presented in Chapter 3. The code was written by Dr. Y.H. Lin and the author, and is presented here using the publishing tool in Matlab R2015b.

### Section 1: Read the output file and fill arrays

```
%---------------------------------------------------------------
%make new text file without strings at the top
fileID=fopen('GaAs_PNjunction_Richards_revised2_Out_readable.txt');
%tell Matlab that it's full of 8 columns of doubles
C=textscan(fileID, '%f %f %f %f %f %f %f %f');
fclose(fileID);
%assign arrays for each column of values from the header of the original
%text file
%****Note: Nd and Na are in /cm^3 so I'm going to change them here to
% /m^3 so I can do SI units****

Y=C{1};
Ec_full=C{2}*1.6e-19;
Ev_full=C{3}*1.6e-19;
E=C{4};
Ef_full=C{5}*1.6e-19;
nx_full=C{6}*1e6;
px_full=C{7}*1e6;
NdNa=C{8}*1e6;

%get thickness of one division in x in the output file (in Angstroms). the
%total thicnkess will be t_out*size_nx (or px)
```

```
t_out=Y(2)-Y(1);
%get the number of entries in the columns I need
dim_nx=size(nx_full);
size_nx=dim_nx(1);

dim_px=size(px_full);
size_px=dim_px(1);

dim_Ef=size(Ef_full);
size_Ef=dim_Ef(1);

dim_Ec=size(Ec_full);
size_Ec=dim_Ec(1);

dim_Ev=size(Ev_full);
size_Ev=dim_Ev(1);
```

**Section 2: Taking full text file arrays and picking N points**

```
%-----------------------------------------------------------------------
%define the number of dimensions (N_dim) you want the 3D matrix to have, and always
make it an even number; the matrix
%will then be NxNxN. What you need to do then is pull 50 data points from
%the nx_full
%and px_full columns to be your entries
%Note: the 'x' in the variable names is there to remind me that these are
%the 1-dimensional versions of the variable

N_dim=60;

%N_divisions tells you how many points to pick, starting with the first
%entry
N_divisions_nx=round(size_nx/N_dim);

for i=0:N_dim
nx(i+1)=nx_full(1+i*N_divisions_nx);
end

N_divisions_px=round(size_px/N_dim);

for i=0:N_dim
px(i+1)=px_full(1+i*N_divisions_px);
end
N_divisions_Ec=round(size_Ec/N_dim);

for i=0:N_dim
```

```
Ec(i+1)=Ec_full(1+i*N_divisions_Ec);
%NdNax(i+1)=NdNa(1+i*N_divisions_NdNa);
end
N_divisions_Ev=round(size_Ev/N_dim);

for i=0:N_dim
Ev(i+1)=Ev_full(1+i*N_divisions_Ev);
%NdNax(i+1)=NdNa(1+i*N_divisions_NdNa);
end
N_divisions_Ef=round(size_Ef/N_dim);

for i=0:N_dim
Ef(i+1)=Ef_full(1+i*N_divisions_Ef);
%NdNax(i+1)=NdNa(1+i*N_divisions_NdNa);
end
```

**Section 3: Read data text file**

```
%----------------------------------------------------------------
%make new text file without strings at the top
fileID=fopen('RMBE1044_polish5_PN_junction_readable.txt');
%tell Matlab that it's full of 8 columns of doubles
C=textscan(fileID, '%f %f %f %f %f %f %f %f');
fclose(fileID);
%assign arrays for each column of values from the header of the original
%text file
%****Note: Nd and Na are in /cm^3 so I'm going to change them here to
% /m^3 so I can do SI units****

Y=C{1};
V_data=C{2};%mV
St_dev=C{3};%mV
X_nocor=C{4};%nm
Xcor=C{5};%nm
```

**Section 4: Define hole and electron mobilities ue and up in terms of nx and px**

```
%----------------------------------------------------------------
% This equation comes from the supporting materials of the nanoletters
% scanning AFM paper: Lee et al., Nano Lett. 12, 4472 (2012)

for i=1:N_dim
    uex(i)=65+1265/(1+(nx(i)/8.5e16)^0.72);
    upx(i)=48+447/(1+(px(i)/6.3e16)^0.76);
end
```

**Section 5: Calculate Se and Sp in 1D**

```
%--------------------------------------------------------------

e=1.60217646e-19;
%electron charge

ke=1.3806053e-23;
%Boltzmann constant
T_in=300;
for i=1:N_dim
   if nx(i)~=0
      %Sex(i)=-ke/e*(log(Ndx(i)./nx(i))+3);
      Condex(i)=nx(i)*e*uex(i);
      Sex(i)=-1/(e*T_in)*(Ec(i)-Ef(i)+3*ke*T_in);
   else
      Sex(i)=0;
      Condex(i)=0;
   end
   if px(i)~=0
      %Spx(i)=ke/e*(log(Nax(i)./px(i))+3);
      Condpx(i)=px(i)*e*upx(i);
      Spx(i)=1/(e*T_in)*(Ef(i)-Ev(i)+3*ke*T_in);
   else
      Spx(i)=0;
      Condpx(i)=0;
   end
end
```

**Section 6: Calculate the total S in 1D, and then convert it to 3D**

```
%--------------------------------------------------------------
for i=1:N_dim
   Stotx(i)=(nx(i)*uex(i)*Sex(i)+px(i)*upx(i)*Spx(i))/(nx(i)*uex(i)+px(i)*upx(i));
   Condtotx(i)= Condex(i)+ Condpx(i);
end

for k=1:N_dim
for j=1:N_dim
   for i=1:N_dim
    Stot3D(i,j,k)=Stotx(j);
    Condtot3D(i,j,k)=Condtotx(j);
    %Condtot3D(i,j,k)=1;
   end
end
end
```

**Section 7: Calculate the 1D and 2D Temperature matrix**

```
%-----------------------------------------------------------------
rc=round(t_out*size_nx/N_dim)/10;
%rc can be the grid size in nm
%rc=0.5;
%manually control rc

% rtip=1;
%size of tip contact area

%Set temperature grid. Let it be odd number. It can only be smaller than N_dim
T_dim=11;
if T_dim >= N_dim
   T_dim=N_dim;
end

 %For now, start with a given tip position (I,J)
 I=N_dim/2;
 Y0=11;
 Yf=49;
 %J=round(N_dim/2);

 for i=1:(Yf-Y0+1)
   for j=1:(Yf-Y0+1)
       DT(i,j)=0;
       Slong1D(j)= Stot3D(I,Y0+j-1,1);
   end
 end

 for i=1:(Yf-Y0+1+T_dim)
   for j=1:(Yf-Y0+1)
       DTtemp(i,j)=0;
   end
 end
 X=zeros([1,Yf-Y0]);
for J= Y0:1:Yf
   %T1 is the temperature of the sample far from the tip, Tc is the
   %temperature at the contact point, and Tth is the
   %**measured** temperature of the tip where
   %f*(T1-Tth)= T1-Tc
   Tth=302;
   T1=321;
   %Tip-sample f-factor
   f=.2;
   rctest=7;
   rtip=0;
```

```
 %Define R(i,j) which is the distance of each grid box to the tip position
 %(I,J), then calculate T(i,j) as a function of r(i,j)
       for i=1:T_dim
           for j=1:T_dim
               r(i,j)=rc*sqrt((((T_dim+1)/2)-i)^2+((((T_dim+1)/2)-j))^2);
               if r(i,j)>=(rctest+rtip)
               %T(i,j)=Tc+(T1-Tc)*(1-(rc/r(i,j));
               T(i,j)=T1-f*(T1-Tth)+f*(T1-Tth)*(1-(rctest/(r(i,j)-rtip)));
               else  T(i,j)=T1-f*(T1-Tth);
                   % else T(i,j)=Tc
               end
           end
       end
%Construct 1D temperature profile and 1D Seebeck vector
for i=1:T_dim
       T1D(i)=T((T_dim+1)/2,i);
       Stot1D(i)=Stot3D(I,J-(T_dim+1)/2+i,1);
       %for test set Stot1D(:)=0.001,if f=0.75 dT=20, V should be
       %0.015
       %Stot1D(i)=0.001;
end
```

**Section 8: Calculate 1D V**

```
%S in 1D is know:Stotx(:)
%Need to Calculate dT:
%Note: dimension of S matrix can be bigger than T matrix. V should be
%the same dimension as T
% Set boundary condition
Vcal1D(1)=0;
Vcal1D(T_dim)=0;
%Vcal1D(T_dim-1)=0;

for i=2:(T_dim-1)/2
    % Calculate potential
    Vcal1D(i)= Vcal1D(i-1)+ (-0.5)*(Stot1D(i-1)+Stot1D(i))*(T1D(i)-T1D(i-1));
    Vcal1D((T_dim+1)-i)=Vcal1D(T_dim-i+2)+ (-0.5)*(Stot1D(T_dim-
i+2)+Stot1D(T_dim-i+1))*(T1D(T_dim-i+1)-T1D(T_dim-i+2));
end

for i=1:(T_dim-1)/2
    DTtemp(i+J-Y0+1,J-Y0+1)=0.2*(T1D(i)-T1D(i+1));
    DTtemp(T_dim-i+J-Y0,J-Y0+1)=0.2*(T1D((T_dim+1)-i)-T1D((T_dim-i)));
end
```

```
  DTtemp((T_dim+1)/2+J-Y0,J-Y0+1)=0.6*f*(T1-Tth);%+0.25*(-
T1D((T_dim+1)/2)+T1D((T_dim-1)/2))+0.25*(-
T1D((T_dim+1)/2)+T1D((T_dim+3)/2));

  for i=1:(Yf-Y0+1)
    for j=1:(Yf-Y0+1)
       DT(i,j)=DTtemp(i+(T_dim-1)/2,j);
    end
  end

  %Vcal1D(T_dim/2)=0.5*(Vcal1D(T_dim/2+1)+ (-
0.5)*(Stot1D(T_dim/2)+Stot1D(T_dim/2+1))*(T1D(T_dim/2)-
T1D(T_dim/2+1))+Vcal1D(T_dim/2-1)+ (-0.5)*(Stot1D(T_dim/2-
1)+Stot1D(T_dim/2))*(T1D(T_dim/2)-T1D(T_dim/2-1)));
  Vctemp=0.5*(Vcal1D((T_dim+1)/2+1)+Vcal1D((T_dim+1)/2-1));

  if abs(Vctemp) < abs((-0.5)*(Stot1D((T_dim+1)/2))*(T1D((T_dim+1)/2-1)-
T1D((T_dim+1)/2-2)))
  Vcal1D((T_dim+1)/2)=0.25*(4*Vctemp+(-
0.5)*(Stot1D((T_dim+1)/2))*(T1D((T_dim+1)/2-1)-T1D((T_dim+1)/2-2))+(-
0.5)*(Stot1D((T_dim+1)/2))*(T1D((T_dim+1)/2+1)-T1D((T_dim+1)/2+2)));
  else
  Vcal1D((T_dim+1)/2)=Vctemp;
  end

  %Vcal1D((T_dim+1)/2)=0.5*(Vcal1D((T_dim+1)/2+1)+Vcal1D((T_dim+1)/2-1));
```

**Section 9: construct 2D conductivity matrix and 2D Seebeck matrix**

```
  %-----------------------------------------------------------------
  %for testing, we construct unity conductivity matrix
  %Take out Stot2D from Stot3D according to tip position.
  %Dimension of Stot2D should be T_dim
  for i=1:T_dim
          for j=1:T_dim
              Cond(i,j)=Condtot3D((I-(T_dim+1)/2)+i,(J-(T_dim+1)/2)+j,1);
              Stot2D(i,j)= Stot3D((I-(T_dim+1)/2)+i,(J-(T_dim+1)/2)+j,1);
              %for test Stot2D(:,:)=0.001, if f=0.3 dT=20, V should be
              %0.006
              %Stot2D(i,j)=0.001;
              %Cond(i,j)=1;
          end
  end
```

**Section 10: initialize 2D Potential matrix V**

```
  %-----------------------------------------------------------------
```

```
%Set potential at boundary grid = 0
for i=1:T_dim
        for j=1:T_dim
            if i==1 || i==T_dim
            Vini(i,j)=0;
            Vcal2D(i,j)=0;
            elseif j==1 || j==T_dim
            Vini(i,j)=0;
            Vcal2D(i,j)=0;
            else
            Vini(i,j)=1;
            end
        end
end
```

**Section 11: Calculation of 2D V**

```
%Calculate First 2D V matrix
%Use nearest known potential neighbor, temperature profile, and
%conductivity profile. V is solved by Kirchoff's law

for b=2:round(((T_dim+1)/2))
   for a=2:round(((T_dim+1)/2))
   %upper left x-direction
      Vtemp1=Vini(a-1,b)+(-0.5)*(Stot2D(a,b)+Stot2D(a-1,b))*(T(a,b)-T(a-1,b));
      Condtemp1=Cond(a,b)*Cond(a-1,b)/(Cond(a,b)+Cond(a-1,b));
      Vtemp2=Vini(a,b-1)+(-0.5)*(Stot2D(a,b)+Stot2D(a,b-1))*(T(a,b)-T(a,b-1));
      Condtemp2=Cond(a,b)*Cond(a,b-1)/(Cond(a,b)+Cond(a,b-1));
      Vini(a,b)=((Condtemp1)*(Vtemp1)+(Condtemp2)*(Vtemp2))/( Condtemp1+
Condtemp2);
   %upper left y-direction
      Vtemp1=Vini(b,a-1)+(-0.5)*(Stot2D(b,a)+Stot2D(b,a-1))*(T(b,a)-T(b,a-1));
      Condtemp1=Cond(b,a)*Cond(b,a-1)/(Cond(b,a)+Cond(b,a-1));
      Vtemp2=Vini(b-1,a)+(-0.5)*(Stot2D(b,a)+Stot2D(b-1,a))*(T(b,a)-T(b-1,a));
      Condtemp2=Cond(b,a)*Cond(b-1,a)/(Cond(b,a)+Cond(b-1,a));
      Vini(b,a)=((Condtemp1)*(Vtemp1)+(Condtemp2)*(Vtemp2))/( Condtemp1+
Condtemp2);
   %upper right  negative x-direction
      Vtemp1=Vini(T_dim+1-a+1,b)+(-0.5)*(Stot2D(T_dim+1-a,b)+Stot2D(T_dim+1-
a+1,b))*(T(T_dim+1-a,b)-T(T_dim+1-a+1,b));
      Condtemp1=Cond(T_dim+1-a,b)*Cond(T_dim+1-a+1,b)/(Cond(T_dim+1-
a,b)+Cond(T_dim+1-a+1,b));
      Vtemp2=Vini(T_dim+1-a,b-1)+(-0.5)*(Stot2D(T_dim+1-a,b)+Stot2D(T_dim+1-
a,b-1))*(T(T_dim+1-a,b)-T(T_dim+1-a,b-1));
      Condtemp2=Cond(T_dim+1-a,b)*Cond(T_dim+1-a,b-1)/(Cond(T_dim+1-
a,b)+Cond(T_dim+1-a,b-1));
```

```
        Vini(T_dim+1-a,b)=((Condtemp1)*(Vtemp1)+(Condtemp2)*(Vtemp2))/(
Condtemp1+ Condtemp2);
    %upper right  y-direction
        Vtemp1=Vini(T_dim+1-b,a-1)+(-0.5)*(Stot2D(T_dim+1-b,a)+Stot2D(T_dim+1-
b,a-1))*(T(T_dim+1-b,a)-T(T_dim+1-b,a-1));
        Condtemp1=Cond(T_dim+1-b,a)*Cond(T_dim+1-b,a-1)/(Cond(T_dim+1-
b,a)+Cond(T_dim+1-b,a-1));
        Vtemp2=Vini(T_dim+1-b+1,a)+(-0.5)*(Stot2D(T_dim+1-b,a)+Stot2D(T_dim+1-
b+1,a))*(T(T_dim+1-b,a)-T(T_dim+1-b+1,a));
        Condtemp2=Cond(T_dim+1-b+1,a)*Cond(T_dim+1-b,a)/(Cond(T_dim+1-
b+1,a)+Cond(T_dim+1-b,a));
        Vini(T_dim+1-b,a)=((Condtemp1)*(Vtemp1)+(Condtemp2)*(Vtemp2))/(
Condtemp1+ Condtemp2);
    %bottom left x-direction
        Vtemp1=Vini(a-1,T_dim+1-b)+(-0.5)*(Stot2D(a,T_dim+1-b)+Stot2D(a-
1,T_dim+1-b))*(T(a,T_dim+1-b)-T(a-1,T_dim+1-b));
        Condtemp1=Cond(a,T_dim+1-b)*Cond(a-1,T_dim+1-b)/(Cond(a,T_dim+1-
b)+Cond(a-1,T_dim+1-b));
        Vtemp2=Vini(a,T_dim+1-b+1)+(-0.5)*(Stot2D(a,T_dim+1-
b)+Stot2D(a,T_dim+1-b+1))*(T(a,T_dim+1-b)-T(a,T_dim+1-b+1));
        Condtemp2=Cond(a,T_dim+1-b)*Cond(a,T_dim+1-b+1)/(Cond(a,T_dim+1-
b)+Cond(a,T_dim+1-b+1));
        Vini(a,T_dim+1-b)=((Condtemp1)*(Vtemp1)+(Condtemp2)*(Vtemp2))/(
Condtemp1+ Condtemp2);
    %bottom left negative y-direction
        Vtemp1=Vini(b,T_dim+1-a+1)+(-0.5)*(Stot2D(b,T_dim+1-
a)+Stot2D(b,T_dim+1-a+1))*(T(b,T_dim+1-a)-T(b,T_dim+1-a+1));
        Condtemp1=Cond(b,T_dim+1-a)*Cond(b,T_dim+1-a+1)/(Cond(b,T_dim+1-
a)+Cond(b,T_dim+1-a+1));
        Vtemp2=Vini(b-1,T_dim+1-a)+(-0.5)*(Stot2D(b,T_dim+1-a)+Stot2D(b-
1,T_dim+1-a))*(T(b,T_dim+1-a)-T(b-1,T_dim+1-a));
        Condtemp2=Cond(b,T_dim+1-a)*Cond(b-1,T_dim+1-a)/(Cond(b,T_dim+1-
a)+Cond(b-1,T_dim+1-a));
        Vini(b,T_dim+1-a)=((Condtemp1)*(Vtemp1)+(Condtemp2)*(Vtemp2))/(
Condtemp1+ Condtemp2);
    %bottom right negative x-direction
        Vtemp1=Vini((T_dim+1-a)+1,T_dim+1-b)+(-0.5)*(Stot2D((T_dim+1-
a),T_dim+1-b)+Stot2D((T_dim+1-a)+1,T_dim+1-b))*(T((T_dim+1-a),T_dim+1-b)-
T((T_dim+1-a)+1,T_dim+1-b));
        Condtemp1=Cond((T_dim+1-a),T_dim+1-b)*Cond((T_dim+1-a)+1,T_dim+1-
b)/(Cond((T_dim+1-a),T_dim+1-b)+Cond((T_dim+1-a)+1,T_dim+1-b));
        Vtemp2=Vini((T_dim+1-a),T_dim+1-b+1)+(-0.5)*(Stot2D((T_dim+1-
a),T_dim+1-b)+Stot2D((T_dim+1-a),T_dim+1-b+1))*(T((T_dim+1-a),T_dim+1-b)-
T((T_dim+1-a),T_dim+1-b+1));
        Condtemp2=Cond((T_dim+1-a),T_dim+1-b)*Cond((T_dim+1-a),T_dim+1-
b+1)/(Cond((T_dim+1-a),T_dim+1-b)+Cond((T_dim+1-a),T_dim+1-b+1));
```

```
         Vini(T_dim+1-a,T_dim+1-
b)=((Condtemp1)*(Vtemp1)+(Condtemp2)*(Vtemp2))/( Condtemp1+ Condtemp2);
      %bottom right negative y-dierction
         Vtemp1=Vini(T_dim+1-b,T_dim+1-a+1)+(-0.5)*(Stot2D(T_dim+1-b,T_dim+1-
a)+Stot2D(T_dim+1-b,T_dim+1-a+1))*(T(T_dim+1-b,T_dim+1-a)-T(T_dim+1-
b,T_dim+1-a+1));
         Condtemp1=Cond(T_dim+1-b,T_dim+1-a)*Cond(T_dim+1-b,T_dim+1-
a+1)/(Cond(T_dim+1-b,T_dim+1-a)+Cond(T_dim+1-b,T_dim+1-a+1));
         Vtemp2=Vini(T_dim+1-b+1,T_dim+1-a)+(-0.5)*(Stot2D(T_dim+1-b,T_dim+1-
a)+Stot2D(T_dim+1-b+1,T_dim+1-a))*(T(T_dim+1-b,T_dim+1-a)-T(T_dim+1-
b+1,T_dim+1-a));
         Condtemp2=Cond(T_dim+1-b+1,T_dim+1-a)*Cond(T_dim+1-b,T_dim+1-
a)/(Cond(T_dim+1-b+1,T_dim+1-a)+Cond(T_dim+1-b,T_dim+1-a));
         Vini(T_dim+1-b,T_dim+1-
a)=((Condtemp1)*(Vtemp1)+(Condtemp2)*(Vtemp2))/( Condtemp1+ Condtemp2);
      end
   end

   %Iteration Calculation of 2D V
   %Use nearest neighbor potential, temperature profile, and
   %conductivity profile. V is solve by Kirchoff's law

   %initiate Vcal matrix
   for a=1:T_dim
      for b=1:T_dim
         Vcal2D(a,b)=Vini(a,b);
         Vtemp2D(a,b)=Vini(a,b);
      end
   end
   %Start to do interation
   for n=1:20
      for a=2:T_dim-1
         for b=2:T_dim-1
         Vtemp1=Vtemp2D(a-1,b)+(-0.5)*(Stot2D(a,b)+Stot2D(a-1,b))*(T(a,b)-T(a-1,b));
         Condtemp1=Cond(a,b)*Cond(a-1,b)/(Cond(a,b)+Cond(a-1,b));
         Vtemp2=Vtemp2D(a,b-1)+(-0.5)*(Stot2D(a,b)+Stot2D(a,b-1))*(T(a,b)-T(a,b-1));
         Condtemp2=Cond(a,b)*Cond(a,b-1)/(Cond(a,b)+Cond(a,b-1));
         Vtemp3=Vtemp2D(a+1,b)+(-0.5)*(Stot2D(a,b)+Stot2D(a+1,b))*(T(a,b)-
T(a+1,b));
         Condtemp3=Cond(a,b)*Cond(a+1,b)/(Cond(a,b)+Cond(a+1,b));
         Vtemp4=Vtemp2D(a,b+1)+(-0.5)*(Stot2D(a,b)+Stot2D(a,b+1))*(T(a,b)-
T(a,b+1));
         Condtemp4=Cond(a,b)*Cond(a,b+1)/(Cond(a,b)+Cond(a,b+1));

Vcal2D(a,b)=(((Condtemp1)*(Vtemp1)+(Condtemp2)*(Vtemp2)+(Condtemp3)*(Vtemp
3)+(Condtemp4)*(Vtemp4))/( Condtemp1+Condtemp2+Condtemp3+Condtemp4));
```

```
          end
        end
        for a=1:T_dim
           for b=1:T_dim
              Vtemp2D(a,b)=Vcal2D(a,b);
           end
        end
        %test for convergence
        Vtest(n+1)=Vcal2D((T_dim+1)/2,(T_dim+1)/2);
    end
      Vtest(1)=Vini((T_dim+1)/2,(T_dim+1)/2+1);
    Vnocor(J+1-Y0)=f*(T1-Tth)*Stotx(J);
    Vmea1D(J+1-Y0)=Vcal1D((T_dim+1)/2);
    Vmea2D(J+1-Y0)=Vcal2D((T_dim+1)/2,(T_dim+1)/2);
    %X(J-Y0+1)=(J-Y0)*rc;
    X(J-Y0+1)=J-Y0;
end
X=-190:10:190;
 S_theory=Slong1D*1000;
% DTtest=DT;
Vmea1D_ma=DT*transpose(S_theory);
 figure()
% %plot(X,Vmea1D)
% %hold
 plot(X,Vmea2D*1000,'r')
 hold
 %need to shift data over so it's on the same axis

 for i=1:39
   V_trunc(i)=V_data(6+i);
end
 %Scatter(X,V_trunc,'b')
 plot(X,Vnocor*1000,'k')
 plot(X,Vmea1D_ma,'g')
 figure()
 plot(X, S_theory,'k')
 hold
% %plot(X, inv(DT)*transpose(Vmea1D),'gs')
%DT is smaller than V_data so I need to truncate V_data

S_first=inv(DT)*transpose(V_trunc);
 S_zeroth=V_trunc/((T1-Tth)*f);
 plot(X, S_first,'ro')
 plot(X, S_zeroth,'b+')
%
Perc_dev_first_sum=0;
```

```
Perc_dev_zeroth_sum=0;

Perc_dev_first_sum=0;
Perc_dev_zeroth_sum=0;
dim_S=size(S_theory);
x1=1;
x2=dim_S(2);
Res_first_sum=0;
Res_zeroth_sum=0;
for i=x1:x2;
   Res_first(i)=S_first(i)-S_theory(i);
   Res_zeroth(i)=S_zeroth(i)-S_theory(i);
   Res_first_sum=Res_first_sum+abs(Res_first(i));
   Res_zeroth_sum=Res_zeroth_sum+abs(Res_zeroth(i));

   Perc_dev_first(i)=abs(Res_first(i)/S_theory(i))*100;
   Perc_dev_first_sum=Perc_dev_first_sum+Perc_dev_first(i);

   Perc_dev_zeroth(i)=abs(Res_zeroth(i)/S_theory(i))*100;
   Perc_dev_zeroth_sum=Perc_dev_zeroth_sum+Perc_dev_zeroth(i);

end
```

*Published with MATLAB® R2015b*

# Appendix J

## InAs quantum dot supplementary information

This Appendix presents further details of the InAs quantum dots discussed in Chapter 4, including the QD size distribution, STS measurements of the InAs QD surface, SThEM measurements on p-type GaAs, details about the 2D composition averaging, and a sensitivity analysis of the conversion from $V_{SThEM}$ to n.

### J.1 QD size distribution

Figure J.1(a) shows an image of the 2D local gradient of the AFM surface topography, with the distribution of QD sizes plotted in Fig. J.1(b). We use the gradient image in Fig J.1(a) to identify QDs, followed by a threshold method to determine percentage of QDs with diameters within a specified range. This frequency as a function of diameter, shown in Fig. J.1(b), is fit with a Gaussian distribution ($R^2 = 0.99$), revealing a mean diameter of 28 ± 11 nm.

## J.2 STS of uncapped InAs QDs

Figure J.2 shows the differential conductance, dI/dV, as a function of bias voltage on the oxidized surface of the InAs/GaAs QD sample. The voltages correspond to the energy relative to the Fermi level. The spectra display well-defined band edges, with effective band-gap values > 2 eV. We note the absence of electronic states in the vicinity of the Fermi level.

## J.3 $V_{SThEM}$ of p-GaAs

$V_{SThEM}$ for an air-exposed p-GaAs sample as a function of the temperature difference between the tip and sample, $\Delta T = T_{Sample}-T_{Tip}$, is presented in Fig. J.3. We use $\kappa_{GaAs}$ to calculate the f-factor for GaAs and a linear least-squares fit to $V_{SThEM}$ vs. $\Delta T$ to reveal a slope of 0.089. The resulting S-value is 270 μV/K, similar to the bulk value for p-GaAs with $p = 1 \times 10^{19}$ $cm^{-3}$.[21] The correlation coefficient value of 0.99 confirms the linear dependence of $V_{SThEM}$ on $\Delta T$ and the resulting temperature-independence of S for tip-sample temperature differences, $(T_{Sample}-T_{Tip}) < 30$ K. Therefore, a profile measured with a different $\Delta T$ is expected to rigidly shift the $V_{SThEM}$ values, leading to similar conclusions.

## J.4 2D In composition averaging

To determine the position-dependent indium composition, we use $x_{In}$ values based upon those from a similar elastically-relaxed InAs/GaAs QD.[22] We consider a 2D

composition map consisting of the in-plane, x, and out-of-plane, z, directions, where z is the growth direction, shown in Figure J.4, where $x_{In}$ ranges from 0.15 in the WL to 0.65 at the center of the QD. To account for the phonon mean free path-limited spatial resolution of SThEM, perform a 2D (x-z) moving average over 5 x 5 $nm^2$ regions, as marked by the black square, followed by extraction of a 1D $x_{In}$ profile from a line cut through the QD center, marked by the black dashed line.

### J.5 Sensitivity analysis

To examine the sensitivity of the parameters used in the conversion of $V_{SThEM}$ to n, here the analysis is conducted for a variety of composition profiles. Figure J.5(a) presents several composition profiles close to the averaged profile used in Section 4.6, which is shown in black squares. The other profiles contain values 10% higher (green triangle) or 10% lower (red circle), as well as a more gradual spatial profile (blue inverted triangle). The resulting S and n profiles are shown in Figure J.5(b) and (c), respectively. While the exact values change slightly, for all $x_{In}$ profiles in Figure J.5, the S and n profiles are roughly equal; S is less negative in the center than in the WL, and n is lower at the center than in the WL, with maxima in S at the QD edges.

In Figure J.6(a), we examine $x_{In}$ profiles which vary significantly from the averaged profile used in Section 4.6, which is again shown in black squares. We examine three constant $x_{In}$ profiles, $x_{In}$ = 0.2 (green triangle), $x_{In}$ = 0.5 (cyan diamond), and $x_{In}$ = 0.8 (blue inverted triangle), as well as a pure InAs/GaAs quantum well, shown in red circles. The resulting S and n profiles are shown in Figs. J.6(b) and (c), respectively. For the

constant profiles, n tends to decrease with increasing In fraction, but the values for n at the center of the QD are only slightly smaller than that in the WL. S and n for the pure InAs/GaAs quantum well vary most significantly from the original averaged profile, with S significantly larger (more negative), and n significantly smaller. However, the overall shape is still consistent; n is lower at the center of the QD than in the WL. This suggests that a higher In value at the center of the QD than the WL is key for the results to show a significantly reduced n at the center of the WL. However, overall the analysis is not very sensitive to small changes in the composition value, and even with a constant $x_{In}$ value, n is still slightly reduced at the center of the QD.

It is important to note that several steps in this analysis require various assumptions which should be examined in future work. In particular, bulk values are used for the thermal conductivity of InGaAs to calculate the f-factor, and the Boltzmann transport equations for S and n assume bulk semiconductors At length scales less than 10 nm, modifications to these assumptions may be needed, requiring careful analysis of the nanoscale transport.

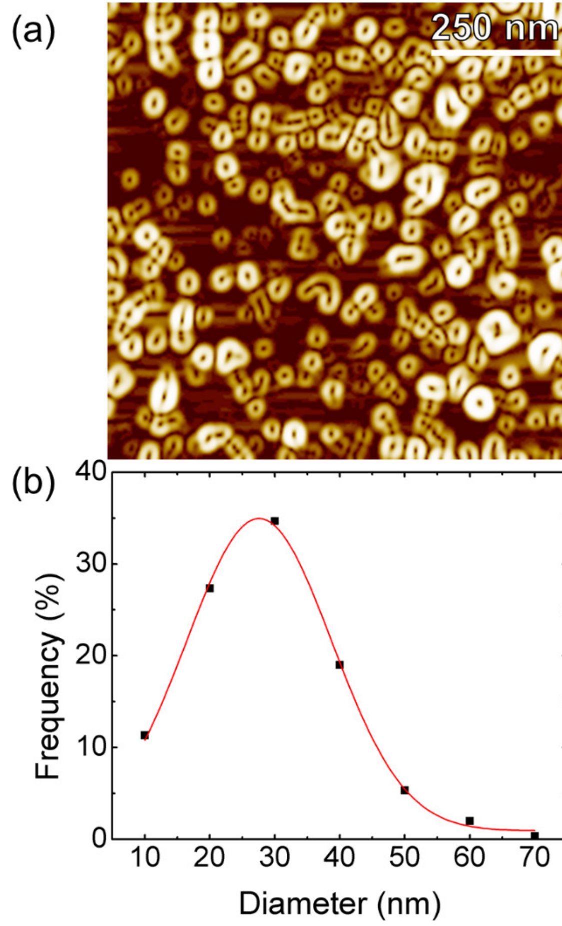


Figure J.1: (a) 2D image of the local gradient of the AFM surface topography (b) Frequency as a function of QD diameter fit with a Gaussian distribution ($R^2$=0.99), revealing a mean diameter of 28 ± 11 nm.

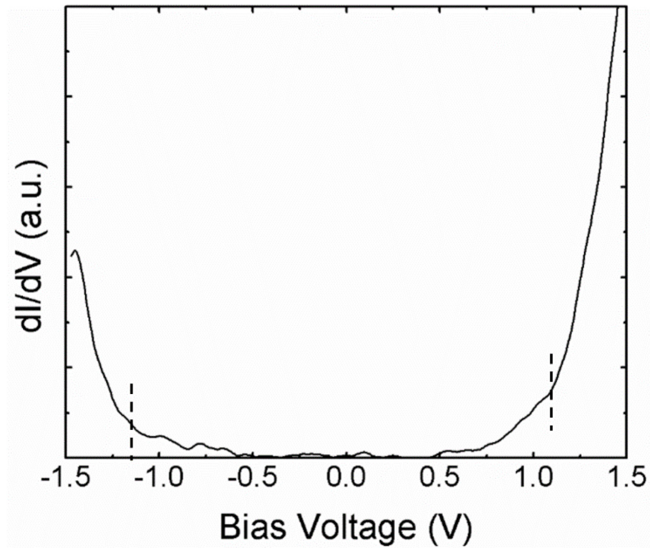


Figure J.2: STS measurement of dI/dV as a function of bias voltage on the oxidized surface of the InAs/GaAs QD sample. The voltages correspond to the energy relative to the Fermi level. The spectra display well-defined band edges, with effective band-gap values > 2 eV. We note the absence of electronic states in the vicinity of the Fermi level. The valence and conduction band edges are marked with vertical dashed lines on the left and right, respectively.

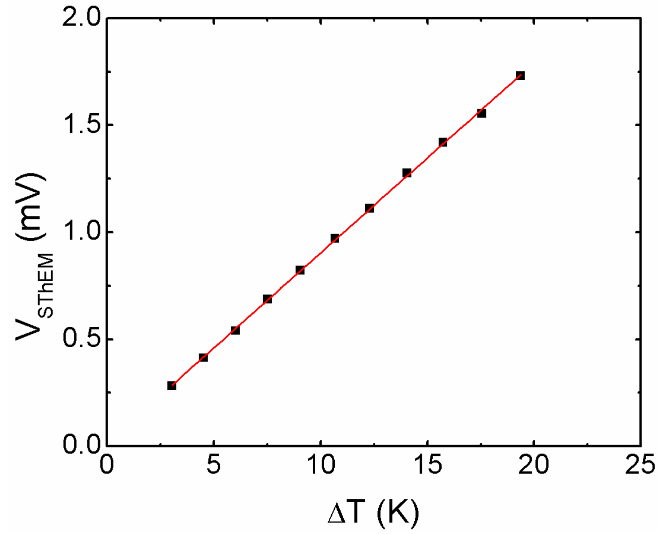


Figure J.3: SThEM data for p-type GaAs as a function of the temperature difference between the tip and sample, $\Delta T = T_{Sample} - T_{Tip}$. A linear least-squares fit to $V_{SThEM}$ vs. $\Delta T$ reveals a slope of 0.089, corresponding to an S-value of 270 μV/K. The correlation coefficient value of 0.99 confirms the linear dependence of $V_{SThEM}$ on $\Delta T$, and the resulting temperature-independence of S.

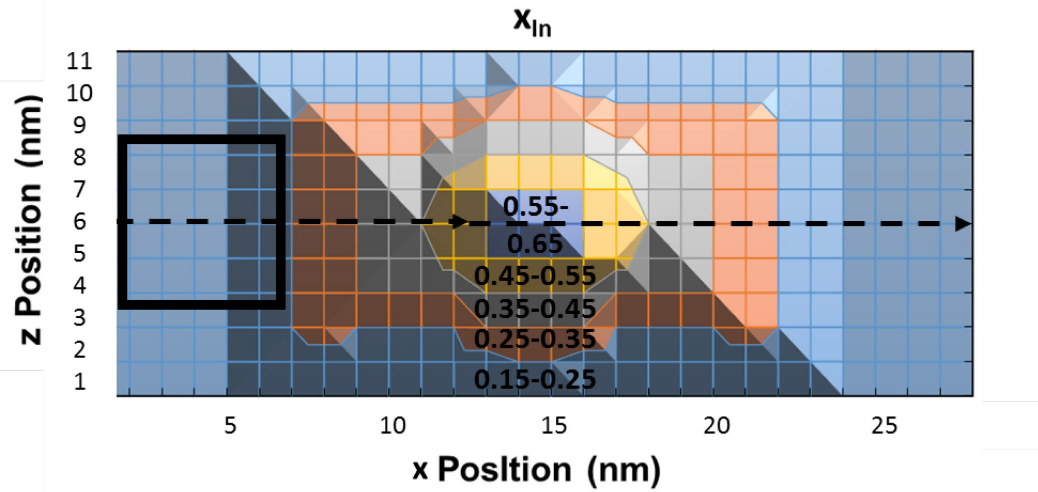


Figure J.4: To determine the position-dependent indium composition, we consider a 2D composition map consisting of the in-plane, x, and out-of-plane, z, directions, where z is the growth direction, where $x_{In}$ ranges from 0.15 in the WL to 0.65 at the center of the QD. We perform a 2D (x-z) moving average over 5 x 5 nm$^2$ regions, as marked by the black square, followed by extraction of a 1D $x_{In}$ profile from a line cut through the QD center, marked by the black dashed line.

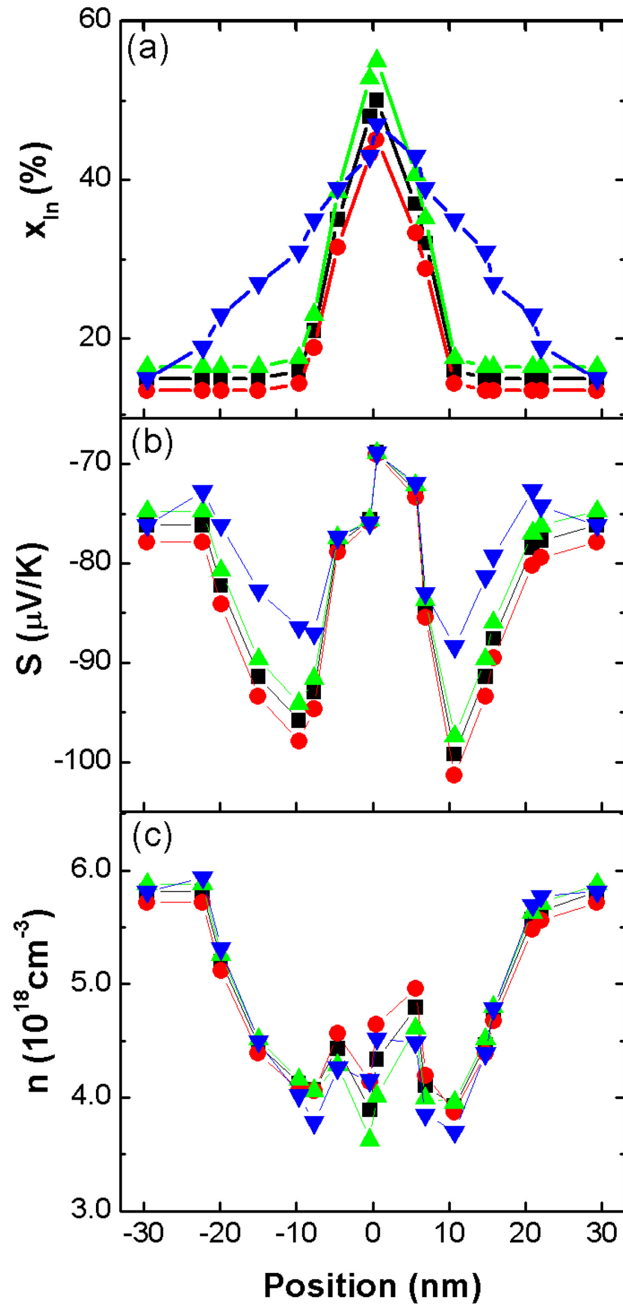


Figure J.5: (a) Varying $x_{In}$ profiles, including with values equal to those used in Section 4.5 (black squares), with values 10% higher (green triangle) or 10% lower (red circle), as well as a more gradual spatial profile (blue inverted triangle). The resulting S and n profiles are shown in (b) and (c), respectively.

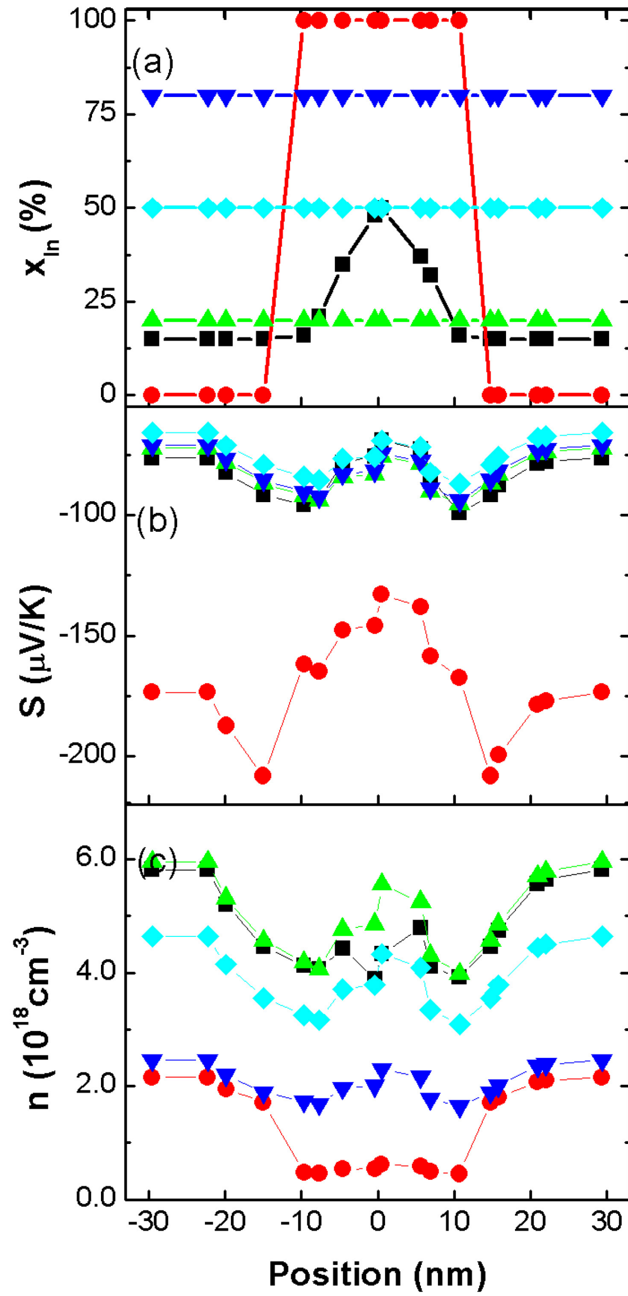


Figure J.6: (a) Varying $x_{In}$ profiles, including with values equal to those used in Section 4.5 (black squares), with constant $x_{In}$ values, $x_{In}$ = 0.2 (green triangle), $x_{In}$ = 0.5 (cyan diamond), and $x_{In}$ = 0.8 (blue inverted triangle), and with values for a pure InAs/GaAs quantum well (red circle). The resulting S and n profiles are shown in (b) and (c), respectively.

# Appendix K

## Atom probe tomography reconstruction and analysis

This appendix presents the details of the APT data reconstruction and analysis, including a comparison of data collected in voltage vs. laser mode, the parameters used for the tip reconstruction, and the details of the Si dopant concentration analysis.

### K.1 Voltage vs. laser mode

APT data was collected from prepared sample tips in both voltage and laser mode with a detection rate of 0.1% and evaporation field of 15 V/nm. For voltage mode, the pulse rate was 120 kHz, while in laser mode 200 kHz was used with a laser power 0.838 pJ at 20K. Figure K.1 shows the mass spectra collected in (a) voltage and (b) laser modes, with various peaks of Ga and As labeled in both. In the voltage mode spectra shown in (a), the peaks have large tails and are not as well defined as those in laser mode, shown in (b), which show sharper peaks. Furthermore, large mass peaks are not well detected in voltage mode, while in laser mode large mass peaks for $As_2$ and $As_3$ are clearly identified. The superiority of laser mode for the InAs/GaAs QD sample is consistent with results in the literature which show that laser-assisted APT is able to thermally enhance the evaporation

of ions from more insulating or semiconducting samples compared to voltage pulsing only.[23,24]

### K.2 Laser mode data collection

To perform APT in laser mode, the laser power is first calibrated by the CAMECA software, and the tip is aligned with the local electrode. Data collection begins with the following settings: pulse rate = 200 kHz, pulse energy = 0.828 pJ, pulse fraction = 20%, starting voltage = 500V, temperature = 20 K. As the voltage increases, detection of ions begins. The tip is raster scanned in a region of microns to coarse-align the laser to the edge of the tip, followed by a fine alignment using focus scan. Every 30 minutes to an hour, the focus scan is repeated to ensure centralization of the APT tip. The experiment continues until the tip fractures or the signatures of all quantum dot layers has been detected.

### K.3 APT tip reconstruction

To select parameters for the reconstruction, we use the radius-evolution reconstruction options in IVAS using the shank-based reconstruction, which assumes an initial tip radius and then evolves the specimen radius with a constant shank angle, measured using an SEM image of the tip. The image compression factor and detector efficiency are then varied until the QD layers have minimum curvature, and the spacing between layers matches the value expected from the MBE growth. A screenshot of the parameters used for the laser mode reconstruction is shown in Figure K.2. The parameters

on the left side are modified and the results examined in real time in the reconstruction explorer on the right.

### K.4 Si dopant analysis

To analyze the Si dopant concentration, we first ensure that the Si concentration is above the detector background. Figure K.1(c) shows a zoomed-in section of the mass spectrum at the location of the Si peak. The horizontal red line is the background noise level calculated by the IVAS software. Thus, the Si dopant peak is significantly above the background.

Then, for each layer, the Si dopant concentration is analyzed in several areas: the GaAs spacer, a section of the WL not including QDs, a section of the WL including QDs, and the QD only, defined by the x = 0.25 isosurfaces. An example of the steps required for the analysis is presented in Figure K.3. First, a cube with a volume of 1710 $nm^3$ is created in the region of interest, shown in Fig. K.3(a) surrounding a QD on the bottom layer. This volume is chosen to be able to cover even the largest of the QDs. Next, a new POS file is created from the cube and the composition is analyzed using the “background corrected” option, shown in Fig. K.3(b). For the QD only analysis, a slightly modified procedure is used. Instead of a cube, the $x_{In}$=0.25 isosurface of the QD is used to create the new POS file, analyzing only the atoms inside the QD. The resulting Si dopant concentration is determined by dividing the number of atoms detected by the volume of the cube or isosurface. These values are approximate only, since the exact number of atoms depends on the detector efficiency. However, comparisons within the same specimen can be made.

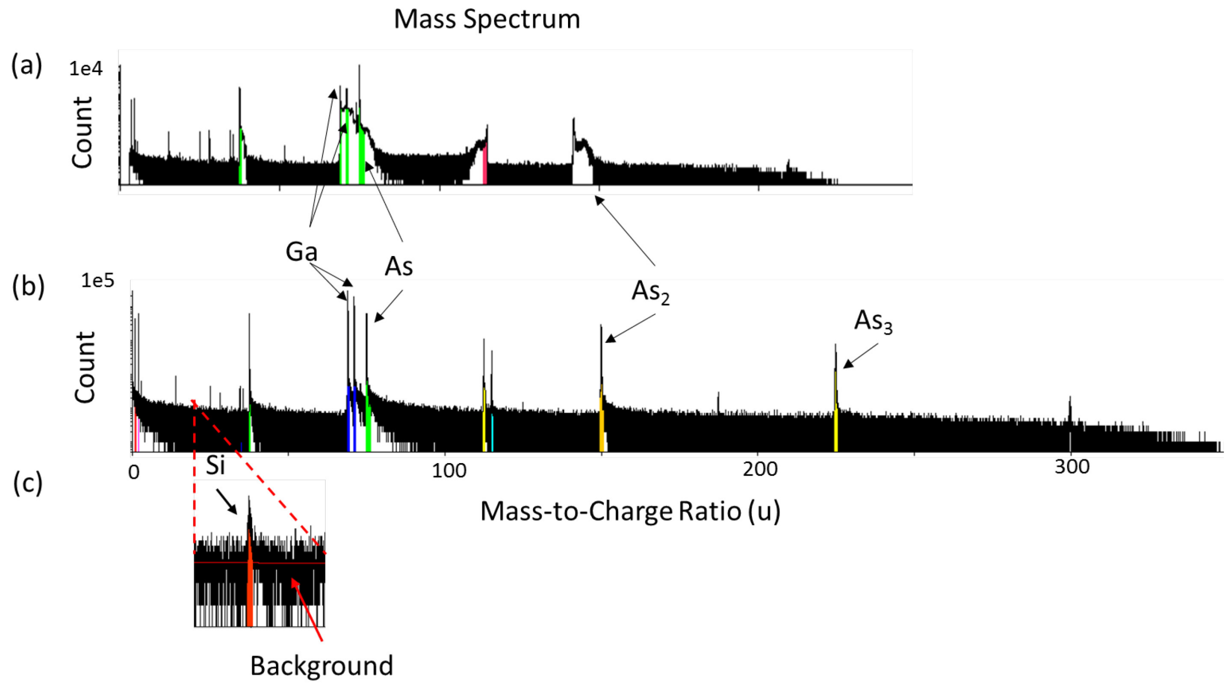


Figure K.1: Mass spectra collected in (a) voltage and (b) laser modes, with various peaks of Ga and As labeled in both. The peaks collected in laser mode are better defined, and high mass peaks are successfully detected. (c) Zoomed-in section of the mass spectrum at the location of the Si peak where horizontal red line is the background noise level calculated by the IVAS software. Thus, the Si dopant peak is significantly above the background.

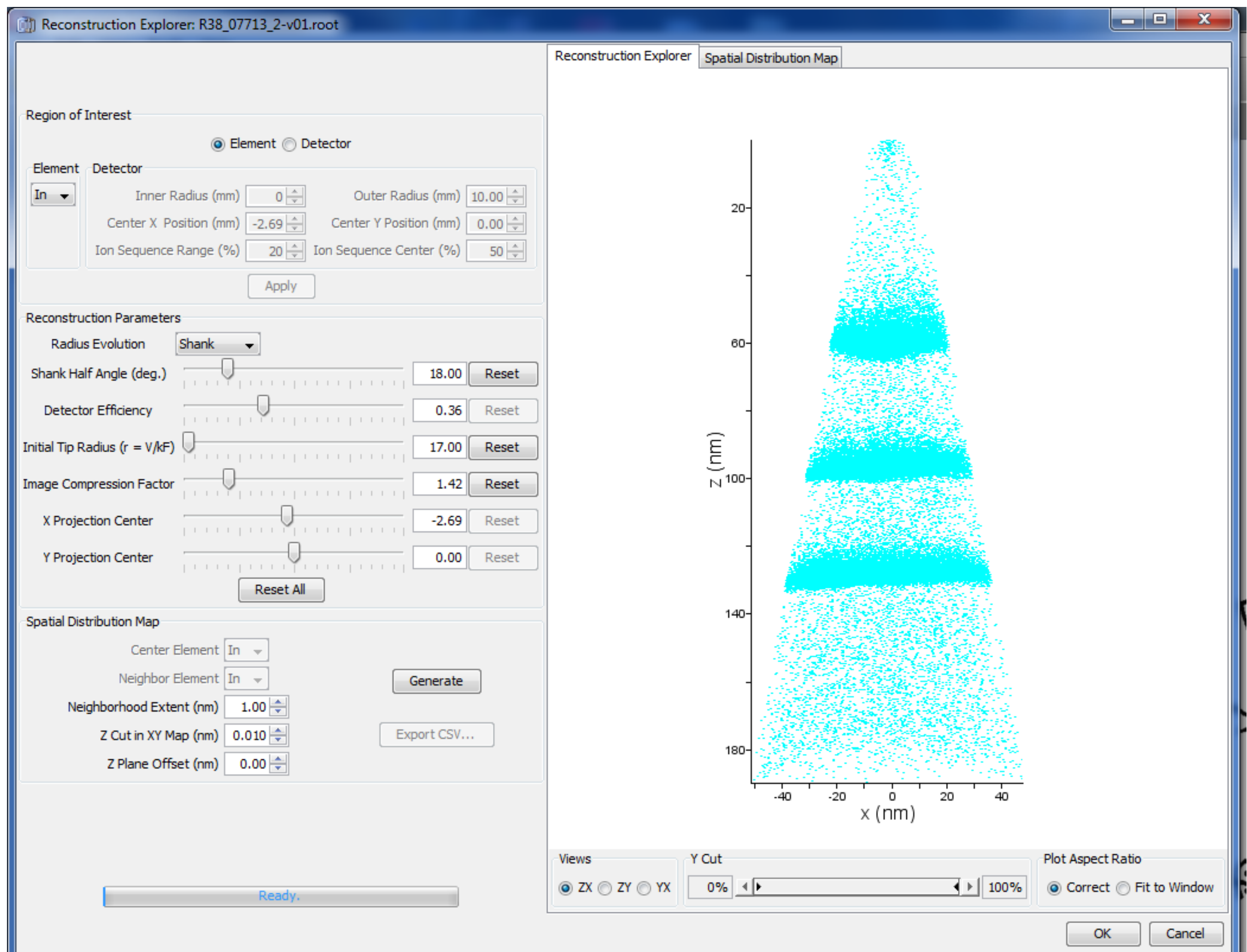


Figure K.2: Reconstruction explorer interface where the image compression factor and detector efficiency are then varied until the QD layers have minimum curvature, and the spacing between layers matches the value expected from the MBE growth. The parameters on the left side are modified and the results examined in real time in the reconstruction explorer on the right.

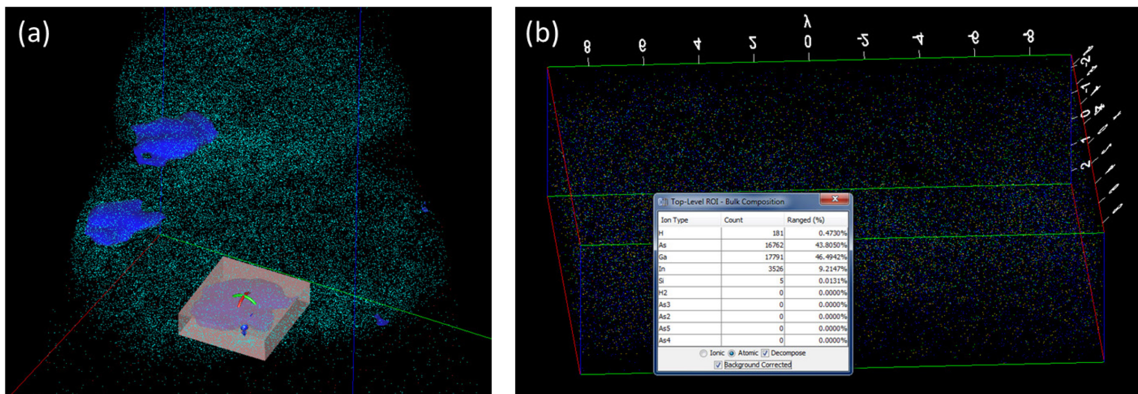


Figure K.3: Si dopant analysis procedure. (a) First, a cube with a volume of 1710 $nm^3$ is created in the region of interest. (b) Next, a new POS file is created from the cube and the composition is analyzed using the "background corrected" option. For the QD only analysis, a slightly modified procedure is used. Instead of a cube, the $x_{In}$=0.25 isosurface of the QD is used to create the new POS file, analyzing only the atoms inside the QD.

**References**

[1] R. Timm, H. Eisle, A. Lenz, L. Ivanova, V. Vosseburger, T. Warming, D. Bimberg, I. Farrer, D.A. Ritchie, and M. Dahne, *Nano Lett.* **10**, 2972 (2010).

[2] Mathworks Documentation. *smooth* (r2015b). Retrieved January 28 2016 from http://www.mathworks.com/help/curvefit/smooth.html

[3] M. Morgenstern, *Phys. Status Solidi B* **248**, 2432 (2011).

[4] H.K. Lyeo, Ph.D. Thesis, University of Texas at Austin, 2003.

[5]J. C. Walrath, Y. H. Lin, K. P. Pipe, and R. S. Goldman, *Appl. Phys. Lett.* **103**, 212101 (2013).

[6] J. C. Walrath, Y. H. Lin, S. Huang, and R. S. Goldman, *Appl. Phys. Lett.* **106**, 192101 (2015).

[7] S. Adachi, Physical Properties of III-V Semiconductor Compounds, *Wiley-VCH Verlag GmbH & Co. KGaA*, 17-47 (2005).

[8] Bismuth Telluride Band Structure, *Springer Materials* **60**, 157-176 (2010).

[9] Antimony Telluride, *Springer Materials* **60**, 157-176 (2010).

[10] David R. Lide, *CRC Handbook of Chemistry and Physics, 84th Edition*. CRC Press. Boca Raton, Florida (2003).

[11] S. Scherrer, H. Scherrer, *Handbook of Thermoelectrics*, CRC Press, Boca Raton, FL (1995), Chap. 19.

[12] I. H. Tan, G. L. Snider, L. D. Chang, and E. L. Hu, J. Appl. Phys. **68**, 4071-4076

(1990).

[13] "$Ga_xIn_{1-x}As$," *New Semiconductor Materials: Characteristics and Properties,* Ioffe

Physico-Technical Institute, © Copyright 1998-2001 by Ioffe Institute,

http://www.ioffe.ru/SVA/NSM/Semicond/GaInAs/index.html.

[14] Professor Gregory Snider, Notre Dame University http://www3.nd.edu/~gsnider/

[15] J.C. Walrath, Y.H. Lin, K.P. Pipe, R.S. Goldman, Appl. Phys. Lett. **103**, 212101 (2013).

[16] J. C. Walrath, Y. H. Lin, S. Huang, and R. S. Goldman, *Appl. Phys. Lett.* **106**, 192101

(2015).

[17] Li, Y.; Stoica, V. A.; Endicott, L.; Wang, G.; Sun, H.; Pipe, K. P.; Uher, C.; Clarke, R. Appl. Phys. Lett. **99**, 121903 (2011).

[18] Y. Li, V. A. Stoica, K. Sun, W. Liu, L. Endicott, J. C. Walrath, A. S. Chang, Y. H. Lin, K. P. Pipe, R. S. Goldman, C. Uher, and R. Clarke, under review (2014).

[19] I. H. Tan, G. L. Snider, L. D. Chang, and E. L. Hu, *J. Appl. Phys.* **68**, 4071-4076 (1990).

[20] Professor Gregory Snider, University of Notre Dame http://www3.nd.edu/~gsnider/.

[21] O. Madelung, U. Rössler, and M. Schulz, *Group IV Elements, IV-IV and III-V Compounds: Part b - Electronic, Transport, Optical and Other Properties*, Landolt-Börnstein - Group III Condensed Matter Volume 41A1b (2002).

[22] A. D. Giddings, J.G. Keizer, M. Hara, G.J. Hamhuis, H. Yuasa, H. Fukuzawa, and P. M. Koenraad, *Phys. Rev. B* **83**, 205308 (2011).

[23] A. Cereo, G. D. W. Smith, and P. H. Clifton, *Appl Phys. Lett.* **88**, 154103 (2006).

[24] N. Dawahre, G. Shen, S. M. Kim and P. Kung, *Microscopy and Microanalysis* **19**, 990 (2013).